



[Click here to view linked References](#)

1 **Review of the Accomplishments of Mid-latitude Super Dual**

2 **Auroral Radar Network (SuperDARN) HF Radars**

3
4
5
6
7
8
9
10 4 Nozomu Nishitani¹

11
12 5 Corresponding author

13 6 Email: nisitani@isee.nagoya-u.ac.jp

14
15
16
17 7
18 8 John Michael Ruohoniemi²

19
20 9 Email: mikeruo@vt.edu

21
22
23
24
25 10
26 11 Mark Lester³

27 12 Email: mle@leicester.ac.uk

28
29
30
31 13
32 14 Joseph Benjamin Harold Baker²

33
34 15 Email: bakerjb@vt.edu

35
36
37 16
38 17 Alexandre Vasilyevich Koustov⁴

39 18 Email: koustov@usask.ca

40
41
42 19
43 20 Simon G. Shepherd⁵

44 21 Email: simon.g.shepherd@dartmouth.edu

45
46
47 22
48 23 Gareth Chisham⁶

49 24 Email: gchi@bas.ac.uk

25

1
2
3
4
5
6
7
8
9
10
11
12
13
14
15
16
17
18
19
20
21
22
23
24
25
26
27
28
29
30
31
32
33
34
35
36
37
38
39
40
41
42
43
44
45
46
47
48
49
50
51
52
53
54
55
56
57
58
59
60
61
62
63
64
65

26 Tomoaki Hori¹

27 Email: tomo.hori@nagoya-u.jp

28

29 Evan G. Thomas⁵

30 Email: evan.g.thomas@dartmouth.edu

31

32 Roman A. Makarevich⁷

33 Email: rmakarevich@alaska.edu

34

35 Aurélie Marchaudon⁸

36 Email: aurelie.marchaudon@irap.omp.eu

37

38 Pavlo Ponomarenko⁴

39 Email: ponomarenko@usask.ca

40

41 James Wild⁹

42 Email: j.wild@lancaster.ac.uk

43

44 Stephen E. Milan³

45 Email: ets@leicester.ac.uk

46

47 William A. Bristow⁷

48 Email: wabristow@alaska.edu

49

1
2
3
4
5
6
7 50 John Devlin¹⁰

8
9
10 51 Email: J.Devlin@latrobe.edu.au

11
12 52

13
14 53 Ethan Miller¹¹

15
16 54 Email: ethan.miller@jhuapl.edu

17
18 55

19
20 56 Raymond A. Greenwald²

21
22 57 Email: ray.greenwald@vt.edu

23
24 58

25
26 59 Tadahiko Ogawa¹²

27
28 60 Email: taogawa@nict.go.jp

29
30 61

31
32 62 Takashi Kikuchi¹

33
34 63 Email: tkikuchi@geosci.jp

35
36 64

37
38 65 (Institutional addresses)

39 66 ¹ Institute for Space-Earth Environmental Research, Nagoya University, Nagoya 464-8601,

40
41 67 Japan

42
43 68 ² Virginia Tech Department of Electrical and Computer Engineering, VA, USA

44
45 69 ³ University of Leicester, UK

46
47 70 ⁴ University of Saskatchewan, SK, Canada

48
49 71 ⁵ Thayer School of Engineering, Dartmouth College, Hanover, NH, USA

50
51 72 ⁶ British Antarctic Survey, UK

52
53 73 ⁷ University of Alaska Fairbanks, AK, USA

54
55 74 ⁸ Institut de Recherche en Astrophysique et Planétologie, University of Toulouse, CNRS, CNES,

1	
2	
3	
4	
5	75 France
6	
7	76 ⁹ Lancaster University, UK
8	
9	
10	77 ¹⁰ La Trobe University, Australia
11	
12	78 ¹¹ Applied Physics Laboratory, Johns Hopkins University, MD, USA
13	
14	79 ¹² National Institute of Information and Communications Technology, Tokyo, Japan
15	
16	80
17	
18	81
19	
20	82
21	
22	83
23	
24	84
25	
26	85
27	
28	86
29	
30	87
31	
32	88
33	
34	89
35	
36	
37	
38	
39	
40	
41	
42	
43	
44	
45	
46	
47	
48	
49	
50	
51	
52	
53	
54	
55	
56	
57	
58	
59	
60	
61	
62	
63	
64	
65	

90 **Abstract**

91
92 The Super Dual Auroral Radar Network (SuperDARN) is a network of High Frequency (HF)
93 radars located in the high- and mid-latitude regions of both hemispheres that is operated under
94 international cooperation. The network was originally designed for monitoring the dynamics of
95 the ionosphere and upper atmosphere in the high-latitude regions. However, over the last
96 approximately 15 years SuperDARN has expanded into the mid-latitude regions. With radar
97 coverage that now extends continuously from auroral to sub-auroral and mid-latitudes a wide
98 variety of new scientific findings have been obtained. In this paper, the background of mid-
99 latitude SuperDARN is presented at first. Then the accomplishments made with mid-latitude
100 SuperDARN radars are reviewed in five specified scientific and technical areas: convection,
101 ionospheric irregularities, HF propagation analysis, ion-neutral interactions and
102 magnetohydrodynamic (MHD) waves. Finally, the present status of mid-latitude SuperDARN
103 is updated and directions for future research are discussed.

104
105 **Keywords**

106 Mid-latitude SuperDARN, ionosphere, magnetosphere, convection, ionospheric irregularities,
107 HF propagation analysis, ion-neutral interactions, MHD waves

110 Introduction

111
112 The Super Dual Auroral Radar Network (SuperDARN) is a network of High Frequency (HF)
113 radars located in the high- and mid-latitude regions of both hemispheres that is used to study
114 the dynamics of the ionosphere and upper atmosphere on global scales. As of 01 Jan 2018 there
115 were a total of 36 SuperDARN radars, 23 in the northern hemisphere and 13 in the southern
116 hemisphere as shown in Fig. 1. The fields of view (FOVs) of the mid-latitude radars are shown
117 in red. Table 1 shows a list of all the SuperDARN radars (details of geomagnetic coordinates
118 will be described in the “Meaning of Geomagnetic Coordinates” subsection). Figure 2 shows a
119 photo of the Fort Hays East (FHE) and West (FHW) antenna arrays and the shelter that houses
120 the electronic equipment for both radars. The main and interferometer antenna arrays of each
121 radar are used for measuring the elevation angle, which is estimated from the phase difference
122 between the signals received on these two arrays.

123
124 SuperDARN achieved official status in 1995 when the Principal Investigators' Agreement was
125 signed. Until about 2004, the SuperDARN radars were only able to monitor the regions of the
126 ionosphere and upper atmosphere poleward of about 60° geomagnetic latitude (MLAT).
127 Ionospheric and upper atmospheric phenomena in the sub-auroral or mid-latitude regions were
128 largely inaccessible to the radars.

129
130 The first purpose-built ‘mid-latitude’ SuperDARN radar, with a site located equatorward of
131 50° MLAT, began operating at the National Aeronautics and Space Administration (NASA)
132 Wallops Flight Facility on Wallops Island, Virginia (U.S.) (WAL) in 2005, shortly followed by
133 the second mid-latitude radar in Hokkaido (Japan), Hokkaido East radar (HOK) in 2006
134 (detailed discussion of the definition of the mid-latitude SuperDARN will be made in the

135 “Definition of a Mid-latitude Radar” subsection). The success of these radars led to the
136 construction of a second U.S. radar near Blackstone, Virginia (BKS) and finally to the
137 deployment of a chain of radars that extends across North America and the northern Pacific
138 Ocean into eastern Asia. As a result, there are now more than 10 mid-latitude SuperDARN
139 radars with additional radars under construction or planned. See the “Historical Overview of
140 Mid-latitude SuperDARN” subsection for the details of the mid-latitude SuperDARN history.

141
142 Over the past 15 years of operation of mid-latitude SuperDARN radars, a number of scientific
143 discoveries have been made that encompass processes in the magnetosphere, ionosphere,
144 thermosphere and upper mesosphere, some with wide latitudinal and longitudinal extents. It
145 seems an appropriate time to review the new scientific results and critically assess these
146 achievements.

147
148 There have been several previous papers that review the entire SuperDARN network (e.g.,
149 Greenwald et al., 1995; Chisham et al., 2007) but none have focused exclusively on mid-latitude
150 studies. The purpose of this paper is to review the accomplishments made with the mid-latitude
151 SuperDARN radars. It is hoped this will enhance coordination between the SuperDARN groups
152 in different countries and will help make their accomplishments known to scientists in other
153 research fields. In addition, by looking back on the scientific achievements, one can also look
154 forward to the future. This review concludes with a discussion of several aspects of the future
155 directions of the mid-latitude SuperDARN network.

1 **156 Basics of SuperDARN**

2
3
4 157
5
6
7 158 SuperDARN radars observe scatter from a variety of sources, including ionospheric
8
9
10 159 irregularities, the ground / sea surface, meteor ionization trails, and possibly ice crystals in the
11
12
13 160 mesosphere, sometimes referred to as Polar Mesosphere Summer Echoes (PMSE). Thus these
14
15
16 161 radars are very versatile in terms of the science which they can address. Here a very brief
17
18
19
20 162 discussion of the basics of the types of scatter, modes of HF propagation, and operating modes
21
22
23 163 is provided, recognizing that the first two of these will be covered in more detail in terms of the
24
25
26 164 mid-latitude radar observations in later sections.

27
28
29 165
30
31
32 166 SuperDARN radars are coherent scatter radars (Greenwald et al. 1995) where the signal
33
34
35 167 received from the ionosphere is similar to Bragg scatter of X-rays in crystals. Here the signal is
36
37
38
39 168 returned essentially along the same path as the transmitted signal such that the radars receive
40
41
42 169 direct backscatter, although it is possible for the transmitted signal to be scattered in other
43
44
45 170 directions. Due to the nature of Bragg scatter, the scale size of the irregularities from which the
46
47
48 171 signal is scattered is directly related to the half-wavelength of the transmitted signal. The
49
50
51 172 irregularities in the ionosphere causing the backscatter can occur at a range of different altitudes,
52
53
54 173 including the *D*, *E* and *F* regions of the ionosphere (e.g., Milan et al. 1997a; Milan and Lester
55
56
57 174 1998; Milan et al. 2001). A more detailed discussion of ionospheric irregularities is given in

1 175 “Ionospheric Irregularities” section. There are two other potential sources of returned signal
2
3
4 176 from the ionosphere / upper atmosphere. The ionization that is created in the atmosphere by
5
6
7 177 meteors can also lead to backscattered signal in SuperDARN data, but this typically occurs in
8
9
10 178 the near ranges as the meteor trail altitude range is typically between 85 and 120 km (e.g.,
11
12
13 179 Thomas et al. 1986; Hall et al. 1997; Chisham and Freeman 2013). Finally, and perhaps more
14
15
16 180 controversially, there is the possibility that SuperDARN radars receive scatter in near ranges
17
18
19 181 which is similar to PMSE (e.g., Ogawa et al. 2002a; Ogawa et al. 2003; Hosokawa et al. 2005).
20
21
22
23 182 There remains some level of controversy over the validity of this interpretation which requires
24
25
26 183 further investigation (Ponomarenko et al. 2016).
27
28
29 184
30
31
32 185 SuperDARN radars are capable of operating in the HF band of the radio spectrum between 8
33
34
35 186 and 20 MHz although most radars actually operate over a narrower range of frequencies,
36
37
38 187 typically between 10 and 14 MHz. At these frequencies radar signals can be refracted by the
39
40
41
42 188 ionosphere such that over the horizon (OTH) propagation is possible. Although a detailed
43
44
45 189 discussion of HF propagation is given in the “HF Propagation Analysis” section, a brief
46
47
48 190 overview of propagation is provided here and this is illustrated by Fig. 3 which shows an
49
50
51 191 example ray-tracing simulation for 11 MHz transmissions on beam 12 of BKS at 1400
52
53
54 192 Universal Time (UT) on 18th November 2010 (de Larquier et al. 2013). The ray paths (colored
55
56
57 193 in gray) span 5-55° in take-off elevation angle and propagate through an International Reference
58
59
60
61
62
63
64
65

1 194 Ionosphere (IRI)-2011 ionosphere color-coded by electron density according to the scale on the
2
3
4 195 right. Several important HF propagation modes can be identified:
5
6
7 196 1) The first is “penetrating rays” which have high enough elevation angles to pass through the
8
9
10 197 F2 peak density region without ionospheric refraction bringing them to horizontal propagation.
11
12
13 198 These rays exit the topside ionosphere unless they encounter ionospheric plasma irregularities
14
15
16 199 aligned with the geomagnetic field direction (pink lines) that can produce ionospheric
17
18
19 200 backscatter in a so-called “½-hop” mode. Ray segments with favorable aspect conditions for
20
21
22
23 201 experiencing this form of backscatter (i.e., $\leq 1^\circ$ from orthogonality with the geomagnetic field)
24
25
26 202 are shaded black. This ½-hop ionospheric backscatter can occur in both the *E* or *F* regions with
27
28
29 203 the *E* region ionospheric scatter dominating at nearer slant ranges.
30
31
32 204 2) Propagation of rays downward to the ground (including the sea surface) due to refraction by
33
34
35 205 the ionosphere is also illustrated here. These rays result in ‘ground scatter’ once roughness on
36
37
38
39 206 the terrestrial surface is encountered and some power is backscattered to the radar. The ground
40
41
42 207 range to the nearest edge of the ground scatter is a little over 1000 km while the outer edge
43
44
45 208 extends to over 2000 km. The ground scatter is important for a variety of studies, including
46
47
48 209 investigations of atmospheric gravity waves (see the “Ion-Neutral Interactions” section), and
49
50
51 210 Magnetohydrodynamic (MHD) waves (see the “MHD Waves” section).
52
53
54
55 211 3) The signal can take multiple hops to even farther distances, such that the radar can receive
56
57
58 212 scatter from the ionosphere not just directly but from beyond the first location of ground scatter.
59
60

1 213 Moreover, subsequent refraction to downwards propagation can generate bands of ground
2
3
4 214 scatter from more distant ranges.
5
6
7 215
8
9
10 216 The different types of ionospheric scatter are illustrated by the data plotted in Fig. 4 (Clausen
11
12
13 217 et al. 2012) where single scans from the Christmas Valley East and West radars (CVE and
14
15
16 218 CVW, respectively) are plotted. Four different types of scatter are identified in this figure.
17
18
19 219 Scatter type I is low-velocity scatter at very near ranges that has been identified as signal
20
21
22
23 220 returned from meteor ionization trails (e.g., Hall et al. 1997). Scatter type II is in the western
24
25
26 221 part of the CVW FOV and has velocities of the order of 100 m s^{-1} ; this is ionospheric scatter
27
28
29 222 from the *F* region and is typical of the low-velocity backscatter routinely obtained at mid-
30
31
32 223 latitudes on the nightside (e.g., Greenwald et al. 2006). At a somewhat higher latitude, closer
33
34
35
36 224 to 60° N MLAT , and labelled III, there is a narrow-in-latitude but extended-in-local time (LT)
37
38
39 225 region of high-velocity scatter that is typical of a sub-auroral polarization stream (SAPS) event
40
41
42 226 (see the “Convection” section for more detailed discussion of this feature). Finally, the high-
43
44
45 227 velocity scatter type IV is more typical of the type of scatter observed in the auroral zone by
46
47
48 228 the high latitude radars. Thus, Figure 4 illustrates that even mid-latitude radars can observe
49
50
51 229 auroral scatter.
52
53
54
55 230
56
57
58 231 It is important to note that the latitude of a radar does not specifically determine that it will
59
60
61
62
63
64
65

1 232 always measure scatter from a specific region for two reasons. One is simply that the
2
3
4 233 equatorward edge of the auroral oval is not located at the same latitude for all LTs, being at
5
6
7 234 higher latitudes at noon than at midnight (Fig. 5). Furthermore, the level of magnetic activity
8
9
10 235 determines the relative location of a radar with respect to auroral boundaries and hence the type
11
12
13 236 of scatter that is received. As magnetic activity increases and the polar cap area increases, the
14
15
16 237 auroral oval expands equatorward while under extremely quiet conditions the oval moves to
17
18
19
20 238 higher latitudes as the polar cap contracts (e.g., Milan et al. 2003).
21
22
23 239
24
25
26 240 SuperDARN radars have at least 16 different look directions along which they can sample over
27
28
29 241 70 or more range gates. The normal, or Common, operational mode of the radar provides a full
30
31
32 242 azimuth scan every 1 or 2 minutes with integration times that vary between 3 and 7 s per beam.
33
34
35 243 In this mode the scan is always synchronized to start on the 1-minute boundary. Special modes
36
37
38
39 244 can also be run on all the radars or a subset of radars. Here the mode of operation is the same
40
41
42 245 among the radars participating in the special mode and could involve a scanning pattern very
43
44
45 246 different from the standard Common mode. Finally, there are Discretionary modes where
46
47
48 247 individual radars run in a very specific way for specific scientific purposes. These modes are
49
50
51 248 more likely to be run on only one or two radars, often in support of regional campaigns such as
52
53
54 249 rocket launches or during heating campaigns. Special and Discretionary modes can run beam
55
56
57
58 250 scans in any sequence, with any time resolution and also with no synchronization. The
59
60

1 251 allocation of time is made by a working group of the community which allocates no less than
2
3
4 252 50% of time each month to Common modes, up to 20% of each month to Special modes and
5
6
7 253 up to 30% of time to Discretionary mode. The minimum time length of any specific run is
8
9
10 254 currently 6 hours although in the past it has been as long as one day. If there are no requests for
11
12
13 255 either Discretionary or Special time, or radars are not running in these modes, then the
14
15
16 256 operational mode defaults to Common mode.
17
18
19
20 257
21
22
23 258 The radars produce a variety of data products, the most widely used being the backscatter power
24
25
26 259 (signal-to-noise ratio), the line-of-sight (LOS) Doppler velocity, the spectral width and the
27
28
29 260 elevation angle of arrival. The radars transmit a sequence of 7 or 8 unevenly separated pulses
30
31
32 261 with an individual pulse length of 300 microseconds, which provides a range resolution of 45
33
34
35 262 km. A reduced pulse length of 100 microseconds (15 km range resolution) has also been used
36
37
38
39 263 on occasion (e.g., Lester et al. 2004); at least some of the mid-latitude radars have the capability
40
41
42 264 of operating at this higher spatial resolution. From combining pairs of different pulses in the
43
44
45 265 sequence different lags of an autocorrelation function (ACF) are generated. Typically, 25-30
46
47
48 266 multi-pulse sequences are averaged in order to obtain a statistically meaningful ACF against
49
50
51 267 noise, which corresponds to ~3-s integration time for a single beam. From the ACFs the Doppler
52
53
54 268 velocity is estimated by fitting a linear function to the measured ACF phase, while
55
56
57 269 backscattered power and spectral width are estimated from fitting a linear or a quadratic

1 270 function to the logarithm of the measured ACF power. Some radars operate in slightly different

2

3

4 271 modes from this but still create the basic data products described above.

5

6

7 272

8

9 273

10

11

12

13

14

15

16

17

18

19

20

21

22

23

24

25

26

27

28

29

30

31

32

33

34

35

36

37

38

39

40

41

42

43

44

45

46

47

1 274 **Definition of a Mid-latitude Radar**

2
3
4 275 It is not so straightforward to characterize radars as belonging to the mid-latitude region. The
5
6
7 276 auroral oval does provide a scheme for identifying three zones as shown schematically in Fig.
8
9
10 277 5. The continuous band mapped out by auroral luminosity constitutes the auroral oval while the
11
12
13 278 enclosed region is the polar cap. Extending equatorward of the auroral oval is the sub-auroral
14
15
16 279 region. This figure suggests a natural assignment of radar identity based on which region
17
18
19 280 dominates in a radar FOV. However, the positions of the oval boundaries vary with time of day
20
21
22
23 281 and also with geomagnetic activity level. The diurnal variation is fairly predictable but the
24
25
26 282 expansion and contraction with activity level is not. The oval depicted in Fig. 5 is roughly
27
28
29 283 appropriate to a K_p value of 2 which is fairly typical and corresponds to a slight geomagnetic
30
31
32 284 disturbance. The positions of the radars in the northern hemisphere are indicated with dots and
33
34
35 285 labeled with their three-letter identifiers. The FOVs of the radars in the ionosphere generally
36
37
38 286 begin several hundred kilometers to the north of the radar position. It can be seen that the
39
40
41
42 287 original high-latitude radars follow the 60° N MLAT contour; this geometry places them in
43
44
45 288 excellent position to observe across the oval on the nightside for typical conditions. The radars
46
47
48 289 at lower latitudes will then observe across a large ($\sim 10^\circ$) interval of sub-auroral latitudes, even
49
50
51 290 deep on the nightside. This is used as our discriminator: radars sited equatorward of 55° MLAT
52
53
54 291 are considered to be mid-latitude radars while appreciating that during expansion of the oval
55
56
57 292 these mid-latitude radars will make extensive auroral observations. Similarly, during periods of

1 293 contracted oval the high-latitude radars will observe across a substantial portion of the sub-
2
3
4 294 auroral region. Even during relatively quiet periods the high-latitude radars are capable of
5
6
7 295 making sub-auroral observations over their nearer range intervals and along more zonally
8
9
10 296 oriented beam directions. This review incorporates findings on sub-auroral research topics from
11
12
13 297 both the mid-latitude and high-latitude radars, and will make some distinction as to whether
14
15
16 298 radars were purpose-built to be mid-latitude radars capable of making observations of the
17
18
19
20 299 expanded auroral oval.

21
22
23 300

24 25 26 301 **Meaning of Geomagnetic Coordinates**

27
28
29 302 The Earth's magnetic field plays a dominant role in defining the geometry of the auroral oval
30
31
32 303 and it is natural to map auroral phenomena in a geomagnetic coordinate system. The Altitude
33
34
35 304 Adjusted Corrected Geomagnetic (AACGM) coordinate system was derived by Baker and
36
37
38
39 305 Wing (1989) in order to compare data from SuperDARN radars in opposite hemispheres and is
40
41
42 306 based on tracing geomagnetic field lines using the International Geomagnetic Reference Field
43
44
45 307 (IGRF) which is a mathematical description of the Earth's magnetic field updated at five-year
46
47
48 308 intervals (e.g., Barraclough 1987; Thébault et al. 2015). In AACGM coordinates, points along
49
50
51 309 a given magnetic field line are given the same coordinates and are thus a better reflection of
52
53
54
55 310 magnetic conjugacy. The concept of AACGM was re-analyzed by Shepherd (2014) which
56
57
58 311 resulted in a procedure that more accurately represents the underlying coordinate system. The
59
60

1 312 new description, known as AACGM-v2, is the accepted basis for mapping SuperDARN data.
2
3
4 313 Here one encounters an interesting complication: the magnetic field is changing surprisingly
5
6
7 314 rapidly (secular variation) with the result that the geomagnetic coordinates of the radar sites and
8
9
10 315 their FOVs are changing. For example, the MLAT of WAL has changed from 48.37° N to
11
12
13 316 46.96° N, a decrease of 1.4°, over the fifteen years since its construction in 2005. Table 1 lists
14
15
16 317 the AACGM-v2 coordinates of the radar sites to one decimal point accuracy for 1 January 2018.
17
18
19
20 318 The secular variation should be borne in mind when comparing observations from different eras.
21
22

23 319

26 320 **Brief History of Mid-latitude SuperDARN**

27
28
29 321 Figure 6 presents a timeline of radar operations with ordering by MLAT. The AACGM-v2
30
31
32 322 coordinates were used. The first purpose-built mid-latitude SuperDARN radar (WAL) began
33
34
35 323 operation at Wallops in the spring of 2005. This was followed by HOK, a radar in Hokkaido,
36
37
38
39 324 northern Japan, which started operation in 2006. Next, a radar was installed near Blackstone in
40
41
42 325 2008 (BKS). One year later, as a part of the National Science Foundation (NSF) Mid-Sized
43
44
45 326 Infrastructure (MSI) program for ‘StormDARN’, the first radar pair was built near Hays,
46
47
48 327 Kansas (‘Fort Hays’) (FHE and FHW) in 2009, the second near Christmas Valley, Oregon
49
50
51 328 (CVE and CVW) in 2011, and the third on Adak Island (ADE and ADW) in the Aleutians in
52
53
54
55 329 2012. A second SuperDARN radar in Hokkaido, the Hokkaido West radar (HKW), was
56
57
58 330 deployed in 2014. In the southern hemisphere a radar was briefly deployed on the Falkland
59
60

1 331 Islands (FIR) from 2010 to 2011. This radar resumed operations in November 2017. A new
2
3
4 332 radar was deployed at Buckland Park, Australia (BKP) in 2014. For details of the history of the
5
6
7 333 Mid-latitude SuperDARN, please refer to the additional file titled ‘Historical Overview of Mid-
8
9
10 334 latitude SuperDARN’.

11
12
13 335

14
15
16 336
17
18
19
20
21
22
23
24
25
26
27
28
29
30
31
32
33
34
35
36
37
38
39
40
41
42
43
44
45
46
47
48
49
50
51
52
53
54
55
56
57
58
59
60
61
62
63
64
65

1 **337 Structure of This Paper**

2
3
4 338 Figure 7 shows a schematic illustration of natural phenomena which can be studied by
5
6
7 339 SuperDARN radars. It can be seen that SuperDARN observes a wide variety of phenomena,
8
9
10 340 ranging from polar to mid-latitudes, and from the magnetosphere / ionosphere to the
11
12
13 341 thermosphere / upper mesosphere. Some topics have found new prominence in recent years as
14
15
16 342 a direct result of the development of the mid-latitude SuperDARN radars. Specific examples
17
18
19
20 343 include sub-auroral and mid-latitude plasma flows, solar flare effects on the ionosphere, and
21
22
23 344 earthquake-triggered ionospheric disturbances.

24
25
26 345
27
28
29 346 This paper consists of 5 sections, each of which examines a specific scientific area, followed
30
31
32 347 by a section on conclusions and future directions. A major benefit of mid-latitude SuperDARN
33
34
35
36 348 is its ability to monitor the expansion of convection to lower latitudes during geomagnetically
37
38
39 349 active periods, which was not possible with the high-latitude SuperDARN radars because of
40
41
42 350 their limited spatial coverage and radio wave absorption due to enhanced precipitation
43
44
45 351 (“Convection” section). The network is also useful for monitoring the occurrence of ionospheric
46
47
48 352 plasma irregularities across the transition from the auroral to the sub-auroral and mid-latitude
49
50
51 353 zone. (“Ionospheric Irregularities” section). An important element of SuperDARN data capture
52
53
54 354 is the role of HF propagation analysis which provides clues to the disturbance processes in the
55
56
57
58 355 ionosphere due to a variety of factors (“HF Propagation Analysis” section). In addition,

1 356 SuperDARN radars can also monitor ionospheric phenomena affected by the exchange of
2
3
4 357 energy and momentum between the charged and neutral components of the Earth's upper
5
6
7 358 atmosphere ("Ion-Neutral Interactions" section). Finally, the radars are a powerful tool for
8
9
10 359 monitoring MHD waves over a wide latitudinal range and studying their source mechanisms
11
12
13 360 ("MHD Waves" section). After reviewing these scientific topics, future directions of the
14
15
16 361 network will be discussed from several points of view ("Conclusions and Future Directions"
17
18
19 362 section).

20 363
21
22
23
24
25
26
27
28
29
30
31
32
33
34
35
36
37
38
39
40
41
42
43
44
45
46
47
48
49
50
51
52
53
54
55
56
57
58
59
60
61
62
63
64
65

Convection

Motivation for the first SuperDARN radar located equatorward of 50° MLAT, and the subsequent expansion at mid-latitudes, was largely due to the inability of the existing high-latitude network to measure the full latitudinal extent of ionospheric convection during geomagnetically active periods. During times when the auroral region expands equatorward of the lower latitude limit of the existing network (~60° MLAT) radars are no longer able to measure the complete extent of convection. In addition, absorption due to enhanced precipitation can significantly attenuate radar signals at auroral latitudes, further reducing measurements of the ionospheric convection electric field.

Evidence of the need for measurements at lower latitudes was provided by Ruohoniemi et al. (2001) who showed a prompt and widespread ionospheric response to a Coronal Mass Ejection (CME)-driven shock. The high-latitude SuperDARN radars used in this study showed a rapid increase in the convection velocity at all magnetic local times (MLTs), from dawn to dusk, an increase in the amount of backscatter observed and an equatorward expansion of the high-latitude convection region. The study focused on the now-casting capability of SuperDARN during the shock arrival, but it also acknowledged that the auroral region continues to expand equatorward of the existing SuperDARN FOVs and a reduction in the amount of backscatter occurs later in the event. Kane and Makarevich (2010) showed this behavior explicitly in

1 383 several examples of the ionospheric convection response to storm sudden commencement
2
3
4 384 (SSC) with a significant reduction in the amount of backscatter and magnitude of the velocities
5
6
7 385 observed ~30 minutes after the SSC.
8
9

10
11 386
12
13
14
15 387 The success of expanding SuperDARN to the mid-latitude region and capturing the dynamics
16
17
18 388 of storm-time convection is discussed in more detail in the “Storm-Time Convection”
19
20
21 389 subsection. Following the completion of the first mid-latitude radar (WAL), subsequent radars
22
23
24 390 were constructed in rapid succession, extending the coverage of mid-latitude phenomena by
25
26
27 391 SuperDARN both in UT, thereby increasing opportunities for observing transient features
28
29
30
31 392 (discussed in the “Transients” subsection), and MLT, allowing for the characteristics and
32
33
34 393 dynamics of longitudinally extended features, such as SAPS and sub-auroral ion drifts (SAIDs)
35
36
37 394 to be determined (discussed in 10 subsections from “SAPS: Introduction” to “Implications for
38
39
40 395 SAPS Formation Scenarios”).
41
42
43

44 396
45
46
47 397 **Storm-Time Convection**
48
49

50
51 398 During periods of enhanced geomagnetic activity triggered by a sustained southward
52
53
54 399 Interplanetary Magnetic Field (IMF), the auroral electric fields associated with magnetospheric
55
56
57 400 convection are known to expand equatorward into the mid-latitude ionosphere (MLAT < 60°)
58
59

1 401 (e.g., Carbary 2005). Baker et al. (2007) demonstrated for a moderate geomagnetic storm how
2
3
4 402 the high-latitude Goose Bay radar (GBR) can monitor the equatorward progression of the
5
6
7 403 auroral convection over a 6 hr interval from only 75-65° MLAT before observations are
8
9
10 404 disrupted by enhanced precipitation and *E* region backscatter at nearer ranges. However, for the
11
12
13 405 same period the mid-latitude radar (WAL) is able to track the convection expansion from 70-
14
15
16 406 55° MLAT, offering an additional 10° in latitudinal coverage and corresponding improvement
17
18
19 407 in mapping the instantaneous global convection pattern. Later studies of storm-time plasma
20
21
22 408 circulation by Hosokawa et al. (2010), and Thomas et al. (2013) used additional mid-latitude
23
24
25 409 radars to address the role of the convection electric field in the transport of dayside storm
26
27
28 410 enhanced density (SED) plasma through the cusp and into the polar cap to form the polar tongue
29
30
31 411 of ionization (TOI). Figure 8 shows the evolution of a TOI in global positioning system (GPS),
32
33
34 412 now a part of Global Navigation Satellite System (GNSS), total electron content (TEC) and the
35
36
37 413 LOS velocity from SuperDARN radars, including mid-latitude radars located on the dayside
38
39
40 414 measuring the convection throat (Thomas et al. 2013). Previous efforts to determine the
41
42
43 415 connection between mid-latitude SED and polar TOI were hampered by the inability of the
44
45
46 416 high-latitude SuperDARN radars to observe the lower-latitude sunward convecting regions
47
48
49 417 believed to be crucial in this global plasma circulation (Foster et al. 2005).
50
51
52
53
54
55 418
56
57
58
59 419 Baker et al. (2007) also showed the importance of mid-latitude measurements for describing
60
61
62
63
64
65

1 420 the morphology and strength of the large-scale convection electric field pattern, particularly on
2
3
4 421 the nightside during increased geomagnetic activity where convection extends to lower latitudes.
5
6
7 422 Figure 9 shows statistical convection patterns from Baker et al. (2007) both with and without
8
9
10 423 the mid-latitude WAL data during moderate to disturbed geomagnetic conditions ($Kp \geq 3$),
11
12
13 424 illustrating stronger overall convection (larger cross-polar cap potential) and more detail of the
14
15
16 425 flows on the nightside associated with the Harang discontinuity.
17
18
19
20
21 426

22
23
24 427 A more recent study by Thomas and Shepherd (2018) used data from all available SuperDARN
25
26
27 428 radars (including 10 mid-latitude radars) during the seven-year period spanning 2010-2016 to
28
29
30
31 429 produce patterns of the high-latitude convection electric field using a technique similar to that
32
33
34 430 used by Ruohoniemi and Greenwald (1996); Ruohoniemi and Greenwald (2005); and Cousins
35
36
37 431 and Shepherd (2010). The statistical patterns produced by Thomas and Shepherd (2018)
38
39
40 432 demonstrate that inclusion of mid-latitude data can increase the cross polar cap potential by as
41
42
43 433 much as 40% and provides a significantly improved specification of the plasma flows on the
44
45
46 434 nightside during a wide range of geomagnetic activity.
47
48
49

50 435
51
52
53
54 436 Fiori et al. (2010), using the Spherical Cap Harmonic Analysis (SCHA) technique, showed that
55
56
57 437 convection can be increased by moving the lower latitude limit, but caution should be taken
58
59
60
61
62
63
64
65

1 438 with the amount of data going into each pattern. Cousins and Shepherd (2010) demonstrated
2
3
4 439 that the solutions to the statistical patterns were relatively insensitive to the lower latitude
5
6
7 440 boundary.
8
9
10
11 441
12
13
14
15 442 Under steady-state conditions a shielding electric field formed at the inner edge of the plasma
16
17
18 443 sheet and associated with the region 2 field-aligned currents (FACs) counteracts the effects of
19
20
21 444 the solar wind-driven magnetospheric convection at sub-auroral latitudes (Nishida 1968). This
22
23
24 445 shielding electric field is directed in the opposite sense to the dawn-dusk convection electric
25
26
27 446 field and varies on timescales ≤ 1 hour (Kelley et al. 1979). There are two cases where
28
29
30
31 447 significant electric fields may develop in the inner magnetosphere following IMF transitions
32
33
34 448 which occur on timescales faster than the shielding layer can respond. The first is the “under-
35
36
37 449 shielding” scenario where a sudden intensification in convection causes the dawn-dusk electric
38
39
40 450 field to penetrate to the inner magnetosphere and all the way to the equatorial ionosphere. The
41
42
43 451 second case occurs when the IMF Bz component turns northward after prolonged southward
44
45
46 452 IMF conditions and the shielding electric field becomes dominant over the convection electric
47
48
49 453 field, known as “over-shielding”.
50
51
52
53 454
54
55
56
57 455 Ebihara et al. (2008) presented the first mid-latitude SuperDARN observations of the over-
58
59
60
61
62
63
64
65

1 456 shielding electric field using HOK. They examined two reverse flow periods during a moderate
2
3
4 457 geomagnetic storm, the first of which was attributed to over-shielding associated with a
5
6
7 458 northward IMF turning while the second occurred during southward IMF conditions and could
8
9
10 459 not be replicated in the ring current simulation. The second one is probably associated with a
11
12
13 460 substorm. When a substorm occurs, over-shielding is shown to appear at low- and mid-latitudes
14
15
16 461 without northward turning of IMF by global MHD simulation (Ebihara et al., 2014). A later
17
18
19
20 462 study by Kikuchi et al. (2010) also examined over-shielding signatures during the same
21
22
23 463 geomagnetic storm, although in the context of equatorial DP2 fluctuations attributed to
24
25
26 464 alternating eastward and westward electrojets in the equatorial ionosphere. Using mid-latitude
27
28
29 465 SuperDARN contributions to the instantaneous global convection patterns, they suggested the
30
31
32 466 dayside reverse flow vortices observed equatorward of the larger two-cell convection
33
34
35
36 467 correspond to the region 2 FACs responsible for over-shielding at the equator. The study of
37
38
39 468 over-/under-shielding phenomena with mid-latitude SuperDARN radars remains an
40
41
42 469 underutilized capability and an area for future studies.

43
44
45 470
46
47
48
49
50 471 To summarize, storm-time convection electric fields corresponding to a variety of geophysical
51
52
53 472 drivers are observed by the mid-latitude SuperDARN radars. Lyons et al. (2016) presented a
54
55
56 473 synthesis of ground- and space-based observations characterizing these fields during the 17
57
58
59 474 March 2013 geomagnetic storm. They identified an inter-relationship between the expansion of

1 475 the auroral oval, penetration electric fields, auroral stream activity, and SAPS, which is
2
3
4 476 discussed in the next section.
5
6
7

8 477

9
10
11 478 **SAPS: Introduction**
12
13

14 479 The sub-auroral region of geospace is where dramatic plasma convection enhancements occur
15
16
17
18 480 during geomagnetic storms and substorms. Initially identified with low-orbit satellites as
19
20
21 481 latitudinally-narrow regions of very strong westward plasma flows up to 4 km s^{-1} , they have
22
23
24 482 been termed polarization jet or PJ (Galperin et al. 1973), SAID (Spiro et al. 1979), and sub-
25
26
27 483 auroral electric field or SAEF (Karlsson et al. 1998). These narrow flow channels were
28
29
30
31 484 proposed to be driven by the poleward polarization electric field located equatorward of the
32
33
34 485 electron precipitation region due to the radial separation between the inner plasma sheet
35
36
37 486 electrons and ions (Southwood and Wolf 1978). A similar explanation has been proposed for
38
39
40 487 broader regions of enhanced plasma convection that were regularly observed during
41
42
43 488 geomagnetic storms by the Millstone Hill incoherent scatter radar (Yeh et al. 1991; Foster and
44
45
46 489 Vo 2002). As a result, an encompassing term of SAPS has been proposed to include both narrow
47
48
49
50 490 PJ/SAID forms and broader regions (Foster and Burke 2002).
51
52

53 491

54
55
56
57 492 Sub-auroral convection enhancements during substorms were also reported based on
58
59
60

1 493 observations by Very High Frequency (VHF) coherent scatter radars (Unwin and Cummack
2
3
4 494 1980; Freeman et al. 1992) and early SuperDARN observations conducted with the most
5
6
7 495 equatorward radars in the high latitude network (Parkinson et al. 2003a; Koustov et al. 2006).
8
9
10 496 These early radar studies stopped short of directly associating the observed signatures with
11
12
13 497 SAPS. To describe their radar substorm signatures, Unwin and Cummack (1980) used the term
14
15
16 498 drift spikes, while Freeman et al. (1992) called their events substorm-associated radar auroral
17
18
19
20 499 surges or SARAS. Similarly, Parkinson et al. (2003a) introduced the term Auroral Westward
21
22
23 500 Flow Channel (AWFC) to describe their Tasman International Geospace Environment Radar
24
25
26 501 (TIGER) Bruny Island (TIG) observations, while Koustov et al. (2006) used the term “SAPS-
27
28
29 502 like flows” in reference to strong convection regions seen by King Salmon radar (KSR). The
30
31
32
33 503 current definition of SAPS does not involve any particular threshold in plasma convection
34
35
36 504 velocity (although there were attempts to estimate the slowest threshold of SAPS velocity, e.g.,
37
38
39 505 Nagano et al. 2015) and it only requires that locally enhanced plasma flows should be linked to
40
41
42 506 the extended dusk convection cell that extends equatorward of the electron precipitation
43
44
45 507 boundary (Huang et al. 2006). For this reason, most of these early radar observations should
46
47
48 508 also be classified as SAPS.

49
50
51
52 509
53
54
55
56 510 The question of the nomenclature is ultimately related to the question of physical origins and
57
58
59 511 driving mechanisms. The radial charge separation and the associated polarization electric field
60

1 512 in the magnetosphere is widely accepted to be one of the two main drivers, with the other one
2
3
4 513 being positive feedback between the magnetospheric electric field and ionospheric conductance
5
6
7 514 (e.g., Wolf et al. 2007). In this feedback model, the magnetosphere-ionosphere (MI) system is
8
9
10 515 assumed to act as a current generator, with the total current being conserved. In this case, the
11
12
13 516 initial polarization electric field drives ion convection in the ionospheric F region, which
14
15
16 517 increases heating and recombination rates, depleting ionospheric densities, and further
17
18
19 518 strengthening SAPS electric fields (Anderson et al. 1993). Despite a general consensus on the
20
21
22 519 importance of these two processes for SAPS formation and evolution, there appears to be a
23
24
25 520 growing realization that these do not explain some characteristics of narrow SAID (Mishin and
26
27
28 521 Puhl-Quinn 2007; Puhl-Quinn et al. 2007). Similarly, the discovery of highly dynamic and
29
30
31 522 localized plasma flows within SAID/SAPS that are often referred to as the SAPS Wave
32
33
34 523 Structure or SAPSWS (Mishin et al. 2003; Mishin and Burke 2005) has challenged the view of
35
36
37 524 SAPS as a generally uniform flow region with possibly one or more narrow SAID-like flow
38
39
40 525 channels (Erickson et al. 2002; Mishin et al. 2003; Foster et al. 2004; Mishin and Burke 2005).
41
42
43 526
44
45
46
47
48
49 527 SuperDARN observes SAPS as a multi-scale phenomenon from large regions of sub-auroral
50
51
52 528 westward convection seen simultaneously by multiple radars to small-scale flow enhancements
53
54
55 529 within only a few range gates. Figures 4 and 10 present two examples of such observations.
56
57
58 530 Figure 4 shows a snapshot of LOS velocities observed by the CVW/CVE pair on 09 April 2011
59
60

1 531 at 0840 UT. The SAPS scatter is observed near MLAT of 60°. The SAPS region extends across
2
3
4 532 both FOVs and the flow velocities are well in excess of 500 m s⁻¹. Figure 10 from Makarevich
5
6
7 533 and Bristow (2014) presents the CVW velocity on 17 March 2013, 0930-1430 UT versus time
8
9
10 534 and MLAT. During the period marked by the two vertical white lines the westward flow is
11
12
13 535 strong and the MLAT range is narrow, which makes it consistent with SAID. Small-scale
14
15
16 536 structure is also clearly present near 1215 UT; it takes the form of small enhancements that are
17
18
19
20 537 only 1-2 range gates in extent and that propagate towards higher MLATs. Figures 4 and 10 thus
21
22
23 538 illustrate the three major advantages of SuperDARN in relation to SAPS research: (1) global-
24
25
26 539 scale spatial coverage that enables SAPS observations over an extended MLT sector, (2) nearly
27
28
29 540 continuous temporal coverage during extended periods, and (3) relatively high spatial and
30
31
32 541 temporal resolutions that enable investigations of small-scale structure of SAPS.
33
34
35

36 542
37
38
39

40 543 In the last decade, SuperDARN has provided numerous contributions to SAPS research that
41
42
43 544 can be divided into the following two groups, roughly corresponding to spatial and temporal
44
45
46 545 features of SAPS. The first exploits the advantage of global coverage of the sub-auroral and
47
48
49
50 546 auroral ionosphere allowing SuperDARN investigations to improve knowledge of global
51
52
53 547 characteristics and external control of SAPS and, through that, achieve a better understanding
54
55
56 548 of the relative importance of global/external factors versus other drivers. The second exploits
57
58
59 549 the advantage of continuous coverage allowing SuperDARN investigations to improve
60
61
62
63
64
65

1 550 knowledge of temporal dynamics of SAPS including the importance of the MI feedback
2
3
4 551 mechanism. Studies that address these two categories of issues are respectively reviewed in the
5
6
7 552 following subsections.

11 553

14 554 **Global Characteristics and Control of SAPS**

17 555 Study of the large-scale structure of SAPS has been greatly advanced by the significantly
18
19
20 556 expanded coverage of mid-latitude SuperDARN. In coordination with the original high-latitude
21
22
23 557 radars, the network of mid-latitude SuperDARN radars is unrivaled in its ability to address the
24
25
26
27 558 spatial characteristics of SAPS on global scales.

30 559

33 560 **Longitudinal Extent and Variation of SAPS**

36 561 The longitudinal structure of SAPS in the sub-auroral and mid-latitude region has been
37
38
39 562 investigated (Oksavik et al. 2006; Koustov et al. 2006; Kataoka et al. 2007; Clausen et al. 2012).
40
41
42 563 In their study, Oksavik et al. (2006) examined a SAPS flow channel equatorward of 60° MLAT
43
44
45
46 564 that was observed for several hours by WAL. It was revealed that a fast westward flow appeared
47
48
49 565 in the premidnight sector, while an eastward flow was co-located on the higher latitude side of
50
51
52 566 the fast westward flow in the post-midnight sector, forming a flow reversal as seen in Fig. 11
53
54
55 567 (Oksavik et al. 2006). Kataoka et al. (2007) examined a similar flow reversal with HOK and
56
57
58
59 568 confirmed that the flow reversal is also present in the post-midnight sector and is enhanced

1 569 during a magnetic storm.

2
3
4 570
5
6
7
8 571 In addition to these studies conducted with single radar, the unique capability of SuperDARN
9
10
11 572 for investigating SAPS – the extensive longitudinal coverage provided by combining several
12
13
14 573 neighboring radars – is evident in more recent studies. A remarkable example demonstrating
15
16
17 574 this capability is given by Clausen et al. (2012), who studied the spatio-temporal evolution of a
18
19
20 575 SAPS flow channel, seen in the bottom/left panel of Fig. 12 as a narrow (few degrees wide)
21
22
23 576 channel of westward flow extending over six hours of MLT and through the FOVs of six mid-
24
25
26
27 577 latitude SuperDARN radars. Comparison with the GPS TEC map in the top/left panel of Fig.
28
29
30 578 12, reveals that the SAPS channel is associated in latitude with the position of the ionospheric
31
32
33 579 trough over this wide range of MLT. In addition, Clausen et al. (2012) determined from the
34
35
36 580 distributed and near instantaneous measurements of the structure that the maximum flow speed
37
38
39 581 within the SAPS increases exponentially with decreasing MLT. However, a more recent
40
41
42
43 582 statistical study suggests the MLT dependence is more commonly quasi-linear (Kunduri et al.
44
45
46 583 2017).

50 584 51 52 53 585 **Dependence of SAPS on Solar Wind and Geomagnetic Drivers**

54
55
56
57 586 Since the deployment of TIG in 1999 and WAL in 2005 in the southern and northern
58
59
60 587 hemispheres, respectively, continuous observations at sub-auroral latitudes have been carried

1 588 out, enabling the correlation of SAPS characteristics with solar wind and geomagnetic
2
3
4 589 conditions to be examined. Several studies using SuperDARN data have identified SAPS
5
6
7 590 characteristics which are basically consistent with those obtained with the Millstone Hill
8
9
10 591 incoherent scatter radar (ISR) (Foster and Vo 2002; Erickson et al. 2011), namely, that SAPS
11
12
13 592 tend to form more often, with faster flow speeds, and at lower latitudes with increasing
14
15
16 593 geomagnetic activity level (Parkinson et al. 2005, 2006; Kataoka et al. 2009; Grocott et al.
17
18
19 594 2011; Kunduri et al. 2012; Nagano et al. 2015; Kunduri et al. 2017). These correlation
20
21
22 595 characteristics strongly suggest that SAPS are closely controlled by solar wind conditions as
23
24
25 596 well as by the ring current. A further examination by Grocott et al. (2011) showed that the
26
27
28 597 latitudinal location of SAID varies on similar time scales to those of the interplanetary magnetic
29
30
31 598 field and auroral activity, while variations in its flow speed are more closely related to ring
32
33
34 599 current dynamics. These results are consistent with the idea that the poleward electric field of
35
36
37 600 SAPS/SAID is caused by the shielding effect of the ring current coupled with the ionosphere
38
39
40 601 through the Region 2 FAC system (Southwood and Wolf 1978).
41
42
43
44
45

46 602

49 603 **Interhemispheric Comparisons of SAPS**

50
51
52
53 604 Several mid-latitude SuperDARN radars share conjugate FOVs between the northern and
54
55
56 605 southern hemispheres and, therefore, provide opportunities to examine interhemispheric
57
58
59 606 conjugacy of the spatial and temporal characteristics of ionospheric convection. Conjugate
60

1 607 characteristics of SAPS were studied by Parkinson et al. (2005) with KSR and TIG, whose
2
3
4 608 FOVs were roughly conjugate to each other. Besides some small asymmetry between the
5
6
7 609 hemispheres, the major variations of SAPS flow are shown to be quite similar, suggesting that
8
9
10 610 the equipotential of geomagnetic field lines holds to the zeroth order. The same conclusions
11
12
13 611 were drawn by similar studies but with a more closely conjugate set of radars (e.g., Kunduri et
14
15
16 612 al. 2012). Grocott et al. (2011) also show excellent agreement in the latitude of a narrow SAPS
17
18
19 613 channel observed by BKS and FIR, as seen in Fig. 13, however differences in the width of the
20
21
22 614 channel were also noted. Interestingly, a detailed inspection of SAPS characteristics by Kunduri
23
24
25 615 et al. (2012) indicate that there is clear asymmetry in the ionospheric Pedersen current and
26
27
28 616 electric field between the conjugate SAPS flows, while the estimated cross-SAPS electric
29
30
31 617 potential drop showed consistent variations. These results suggest that SAPS are quite dynamic
32
33
34 618 but controlled in such a way that the cross-SAPS potential difference stays constant between
35
36
37 619 the two hemispheres despite the occasional significant differences in the details of the
38
39
40 620 electrodynamics between the conjugate hemispheres.
41
42
43
44
45

46 621

49 622 **Temporal Dynamics of SAPS: Introduction**

50
51
52 623 SuperDARN observations are characterized by high temporal resolution, the continuous nature
53
54
55 624 of measurements and large spatial coverage, which make them a formidable asset to study the
56
57
58 625 longevity and the temporal evolution of SAPS-related phenomena at both large (up to 1000s of
59
60

1 626 km) and small (of the order of typical range-gate of the SuperDARN radar, i.e., 50 km). In the
2
3
4 627 beginning a recent statistical study by Kunduri et al. (2017) of the occurrence of SAPS is
5
6
7 628 introduced. Analyzing four years of data from the U.S. mid-latitude radars, they found that
8
9
10 629 SAPS are observed at all levels of geomagnetic disturbance but with a dependence on
11
12
13 630 disturbance level (characterized by *Dst*) such that quiet times have low occurrence rates (~10%)
14
15
16 631 while storm times have very high rates (approaching 100%). The SAPS feature is often clearly
17
18
19
20 632 defined against a background of lower latitude, low-velocity sub-auroral scatter.
21
22

23 633

24

25

26 634

27

28

29 **635 Lifetime/Longevity and Seasonal Dependence of SAPS**

30

31

32

33 636 From SuperDARN observations at mid- and sub-auroral latitudes, a wide range of SAPS

34

35

36 637 durations have been recorded, from a relatively short 30 min up to more than 6 hours (Parkinson

37

38

39 638 et al. 2003a, 2006; Koustov et al. 2006; Oksavik et al. 2006; Grocott et al. 2011), in agreement

40

41

42 639 with studies based on other experimental facilities (e.g., Anderson et al. 1991, 2001; Foster and

43

44

45 640 Vo, 2002). A large fraction of these studies referred to substorm-time SAPS in its narrow and

46

47

48

49 641 short form of PJ/SAID, while longer SAPS events were observed mostly by mid-latitude radars

50

51

52 642 which are better suited for storm-time observations (Oksavik et al. 2006; Grocott et al. 2011).

53

54

55

56 643

57

58

59

60 644 In order to investigate possible seasonal trends in the occurrence and properties of SAPS a

61

62

63

64

65

1 645 statistical study was performed using observations of SAPS-like flows from the KSR radar
2
3
4 646 (Koustov et al. 2006). This study shows that higher velocities occur over a larger MLT extent
5
6
7 647 during winter months. The extent and magnitude of flows decrease through equinoctial and
8
9
10 648 summer months. These results agree with the interhemispheric studies of SAPS by Kunduri et
11
12
13 649 al. (2012) who show lower velocities are observed in the summer Northern Hemisphere (BKS
14
15
16 650 and WAL observations) than in the winter Southern Hemisphere (FIR observations), but are in
17
18
19
20 651 slight disagreement with another interhemispheric study by Parkinson et al. (2005), who show
21
22
23 652 that summer Southern Hemisphere velocities (TIG) are slightly higher than in the winter
24
25
26 653 Northern Hemisphere (KSR). To resolve the issue about seasonal dependence of SAPS strength
27
28
29 654 and its controlling factors, a complementary statistical study with one or several mid-latitude
30
31
32 655 radars would clearly be useful.
33
34
35

36 656

39 657 **Evolution and Variability of SAPS**

41
42
43 658 Many SAPS events have been unambiguously related to substorm activity (e.g., Anderson et al.
44
45
46 659 1993). At large scales, a great deal of variability is observed during the course of SAPS lifetime,
47
48
49
50 660 with latitudinal position, width, and flow velocity exhibiting significant variations with time
51
52
53 661 (see Parkinson et al. 2006; Koustov et al. 2006; Oksavik et al. 2006; Makarevich and Dyson
54
55
56 662 2007; Kataoka et al. 2007; Ebihara et al. 2009; Makarevich et al. 2011; Clausen et al. 2012).
57
58
59 663 Such variations are also clearly observed in the SAID structure whether embedded in SAPS or
60

1 664 not (Oksavik et al. 2006; Grocott et al. 2011; Kunduri et al. 2012), with the observed thinning
2
3
4 665 of the SAID being possibly related to a transition between successive events (Grocott et al.
5
6
7 666 2011). Moreover, Makarevich and Dyson (2007) and Clausen et al. (2012), thanks to extensive
8
9
10 667 spatial coverage provided by several radars, also show that velocity intensifications inside
11
12
13 668 SAPS are tremendously different with respect to longitude, as illustrated in the right panel of
14
15
16 669 Fig. 12. In addition, Clausen et al. (2012) show that large-scale variations of SAPS speed are
17
18
19
20 670 not accompanied by variations of SAPS flow direction which remain extremely stable
21
22
23 671 throughout the course of the event at given longitudes.
24
25
26
27 672
28
29
30 673 SuperDARN observations of SAPS in conjunction with global auroral observations have
31
32
33
34 674 demonstrated the important role played by auroral dynamics on the spatio-temporal evolution
35
36
37 675 of SAPS. Makarevich et al. (2009) studied the temporal evolution of SAPS in the context of
38
39
40 676 simultaneous auroral dynamics provided by the International Monitor for Auroral Geomagnetic
41
42
43 677 Effects (IMAGE) spacecraft and clearly show that auroral dynamics affect the latitudinal
44
45
46 678 position of the SAPS poleward boundary as well as the SAPS intensity, but not the SAID
47
48
49
50 679 position. It is demonstrated that equatorward motion of the aurora can effectively compress the
51
52
53 680 SAPS flow channel into its narrow SAID form while simultaneously strengthening it. Another
54
55
56 681 effect of the auroral expansion and associated compression of the convection streamlines is an
57
58
59 682 eastward “mirror” flow channel on the poleward side of the SAID. Furthermore,
60
61
62
63
64
65

1 683 reconfiguration of the convection pattern during substorms results in the concurrent
2
3
4 684 development of the Harang discontinuity and an intensification of SAPS, with strong coupling
5
6
7 685 between them observed in most cases (Zou et al. 2009).
8
9
10
11 686
12
13
14
15 687 A significant fraction of SAPS events observed by SuperDARN have been associated with
16
17
18 688 geomagnetic storms. Kataoka et al. (2007) and Ebihara et al. (2009) explain the dynamical
19
20
21 689 character of the rapid westward flow observed in SAPS as a direct manifestation of spatio-
22
23
24 690 temporal variations of plasma pressure in the inner magnetosphere and ring current during
25
26
27 691 storms. Their results are based on the comparison with the numerical modeling of the inner
28
29
30
31 692 magnetosphere. Figure 14 shows a comparison between the SuperDARN HOK observations of
32
33
34 693 SAPS structure indicating temporal changes (top panel) with simulation results from the
35
36
37 694 Comprehensive Ring Current Model (CRCM) under various boundary conditions (Ebihara et
38
39
40 695 al. 2009). The middle panel shows the simulation result with the outer boundary condition
41
42
43 696 determined by the energetic particle data of the Los Alamos National Laboratory (LANL)
44
45
46 697 geosynchronous spacecraft while the bottom panel shows the simulation result with a fixed
47
48
49
50 698 boundary condition (uniform and constant plasma density). These results clearly indicate the
51
52
53 699 importance of ring current dynamics in controlling the SAPS spatial structure.
54
55
56

57 700

1 701 High temporal resolution (1-min) of SuperDARN measurements also enables observations of
2
3
4 702 small-scale variability inside SAPS. Several studies have demonstrated the existence of strong
5
6
7 703 flow pulsations during SAID periods (Parkinson et al. 2003a, 2005; Koustov et al. 2006;
8
9
10 704 Oksavik et al. 2006; Koustov et al. 2008; Makarevich and Bristow 2014). These pulsations exist
11
12
13 705 in the form of flow channels of extremely high westward velocity (between 1 and 2 km s⁻¹) that
14
15
16 706 are localized in latitude (~50-100 km) and have periods between 10 and 15 min (Parkinson et
17
18
19 707 al. 2003a, 2005; Koustov et al. 2006; Oksavik et al. 2006; Koustov et al. 2008). Lower periods,
20
21
22
23 708 down to 1-2 min, and hence higher frequencies (Makarevich and Bristow 2014) and higher
24
25
26 709 velocities up to 4 km s⁻¹ (Parkinson et al. 2003a) have also been observed. These structures
27
28
29 710 appear close to the equatorial edge of SAPS and the ionospheric trough, and generally propagate
30
31
32 711 toward higher MLAT (Koustov et al. 2006; Makarevich and Bristow 2014). The cause of these
33
34
35 712 pulsations has been attributed to Ultra-Low Frequency (ULF) wave activity, as shown by a
36
37
38 713 correlation with spectral width (Parkinson et al. 2005) or to SAPSWS activity (Mishin et al.
39
40
41
42 714 2003; Makarevich and Bristow 2014).

43
44
45
46 715

47 48 49 716 **Occurrence Frequency of SAPS and Their Dependence on Substorm Phase**

50
51
52
53 717 As previously stated, SAPS are often closely related to substorm processes. Parkinson et al.
54
55
56 718 (2006) have estimated the percentage occurrence rate of strong westward flows associated with
57
58
59 719 SAPS-like feature of AWFC over 12 months of measurements from TIG and found a rate of

1 720 about 40%. Yet with only one radar covering SAPS longitudes for only 25% of the time due to
2
3
4 721 the Earth's rotation, they argued that the occurrence rate could be up to 4 times larger. The
5
6
7 722 implication is that SAPS could be occurring almost every night, making it a recurrent sub-
8
9
10 723 auroral process persisting for several substorm cycles (Makarevich and Dyson 2007; Koustov
11
12
13 724 et al. 2008; Zou et al. 2009; Makarevich et al. 2009), but not necessarily observed due to a non-
14
15
16 725 favorable radar location or propagation conditions. A comprehensive statistical study using the
17
18
19
20 726 larger longitudinal coverage of the existing mid-latitude SuperDARN radars will reduce the
21
22
23 727 speculation in these results.

24
25
26
27 728
28
29
30
31 729 Great attention has been given to relating SAPS onset and intensification to the different phases
32
33
34 730 of the substorm process. Koustov et al. (2006) and Makarevich and Dyson (2007) have shown
35
36
37 731 that SAPS generally appear or undergo a marked increase, if already present, between -5 and +
38
39
40 732 60 min after a substorm onset, with the negative delay being due to a pre-existing
41
42
43 733 substorm/SAPS event. Makarevich and Dyson (2007) examined several SAPS events seen
44
45
46 734 simultaneously by TIG and TIGER Unwin radar (UNW) in conjunction with a substorm onset
47
48
49
50 735 as seen by IMAGE, and conclude that the time delay between substorm onset and SAPS flow
51
52
53 736 enhancement is likely due to the finite propagation time from the substorm injection location at
54
55
56 737 substorm onset to the position of the radars. SAPS generally show a two-stage evolution, with
57
58
59 738 initially relatively weak velocities followed by strong intensifications between 90 and 120 min

1 739 after onset (Makarevich and Dyson 2007). This intensification phase starts, in general, at the
2
3
4 740 end of the substorm expansion phase or during the recovery phase and ceases at the end of the
5
6
7 741 recovery phase (Parkinson et al. 2003a, 2006; Koustov et al. 2006; Makarevich et al. 2009).
8
9
10 742 The narrow SAID feature is more likely to occur during this later stage of SAPS evolution
11
12
13 743 (Oksavik et al. 2006; Parkinson et al. 2006; Makarevich and Dyson 2007). SAPS are also
14
15
16 744 observed during the main phase of storms when several successive substorms and associated
17
18
19
20 745 auroral intensifications are observed (Grocott et al. 2011; Makarevich and Bristow 2014).
21
22
23

24 746

27 747 **Implications for SAPS Formation Scenarios**

28
29
30 748 Observations from SuperDARN radars, particularly at mid-latitudes, have been extremely
31
32
33
34 749 beneficial in advancing our understanding of the underlying cause of SAPS. As explained in
35
36
37 750 the previous subsections, the MI feedback process that is believed to play an important role in
38
39
40 751 SAPS evolution implies that the sub-auroral electric field intensification should be
41
42
43 752 accompanied by a decrease in the ionospheric electron density (e.g., Wolf et al. 2007).
44
45
46 753 Makarevich et al. (2011) and Makarevich and Bristow (2014) exploited the continuous nature
47
48
49
50 754 of SuperDARN observations by also examining simultaneous and continuous measurements of
51
52
53 755 GPS TEC during a SAPS event. A general decrease of electron content inside SAPS during the
54
55
56 756 first stage of weak SAPS evolution was seen, suggesting that the long-term variation of SAPS
57
58
59 757 electron content is largely caused by a continuous depletion of ionospheric density and
60

1 758 supporting the idea of the current generator scenario at large scales. On the other hand, an
2
3
4 759 opposite trend was observed inside SAPS with an overall TEC increase during the second stage
5
6
7 760 of SAPS evolution that is associated with SAID intensification and the appearance of SAPSWS
8
9
10 761 (Fig. 15a from Makarevich and Bristow 2014). This important result was interpreted by
11
12
13 762 Makarevich and Bristow (2014) in terms of cross-scale coupling occurring within SAPS, where
14
15
16 763 net changes in ionospheric conductance and TEC are positive when SAPSWS activity exists
17
18
19 764 and negative in the contrary. Finally, Kunduri et al. (2012) also showed that variations in SAPS
20
21
22
23 765 peak velocity exhibited a moderate correlation with the *ASY-H* index indicating that local
24
25
26 766 ionospheric conditions such as the height integrated Pedersen conductivity and thus electron
27
28
29 767 density, may have an important influence on SAPS flow channel dynamics.
30

31
32
33 768
34
35
36
37 769 Figure 15 illustrates some of the important features of the plasma velocity – electron density
38
39
40 770 relationship within SAPS at short time scales (below 20 min) as presented by Makarevich and
41
42
43 771 Bristow (2014) utilizing close conjunctions between the CVW and a GPS receiver at Beaver
44
45
46 772 Cove (BCOV). Figure 15a illustrates a merging of flow channels with the SAID feature located
47
48
49
50 773 westward and poleward (Makarevich and Bristow 2014). They show that each flow channel
51
52
53 774 enhancement related to SAPSWS is associated with a simultaneous decrease in TEC, followed
54
55
56 775 by a TEC increase outside of each flow channel (see panels b and c of Fig. 15). Wavelet spectra
57
58
59 776 of CVW velocities and GPS TEC also exhibited strikingly similar variations (see panels d and
60

1 777 e of Fig. 15), providing additional evidence for the ionospheric feedback instability scenario
2
3
4 778 even at small scales.

5
6
7
8 779
9
10
11 780 In summary, continuous observations of SAPS by SuperDARN show that the evolution of
12
13
14
15 781 SAPS is strongly controlled by the substorm onset location, prior time history including
16
17
18 782 previous substorm cycles, concurrent auroral dynamics, MI and cross-scale coupling processes.
19
20
21 783 In the future, coordinated and distributed measurements will be central to further understanding
22
23
24 784 the underlying causes of SAPS and SAID. By its continued expansion, the mid-latitude
25
26
27 785 SuperDARN network will be ideally situated to contribute to this effort.

28
29
30
31 786

32 33 34 787 **Transients**

35
36
37
38 788 The distributed and continuous nature of SuperDARN observations are well-suited for studying
39
40
41 789 transient features observed in ionospheric convection. Even operating in the standard mode
42
43
44
45 790 (stepping sequentially through each beam to cover the whole FOVs in 1 min) SuperDARN
46
47
48 791 radars are able to resolve many of the spatio-temporal ambiguities that are often encountered
49
50
51 792 in observations of transient events. Special experimental modes have also been developed to
52
53
54 793 increase the temporal or spatial resolution of observations in order to study particular aspects
55
56
57 794 of transient phenomena.

1 795
2
3
4
5 796 In addition to storm-time phenomena, such as the prompt penetration electric field (PPEF)
6
7
8 797 associated with over/under-shielding, several other types of transient electric fields are
9
10
11 798 observed by SuperDARN. These observations primarily occur in the high-latitude and polar
12
13
14 799 cap regions owing to their origins in the solar wind and the favorable coupling on open magnetic
15
16
17 800 field lines at higher latitudes. Studies of these transients include the response of large- and
18
19
20 801 meso-scale convection to abrupt transitions in the IMF Bz (Ruohoniemi and Greenwald 1998;
21
22
23 802 Shepherd et al. 1999; Milan et al. 2000; Nishitani et al. 2002; Fiori et al. 2012) and IMF By
24
25
26 803 (Chisham et al. 2000; Senior et al. 2002) magnetic field components, the solar wind dynamic
27
28
29
30 804 pressure (Boudouridis et al. 2007; Coco et al. 2008; Boudouridis et al. 2011; Gillies et al. 2012)
31
32
33 805 and interplanetary shocks (e.g., Kane and Makarevich 2010). These studies show general
34
35
36 806 agreement with a two-stage response consisting of a prompt initial perturbation in the
37
38
39
40 807 convection velocity seen nearly simultaneously at all MLTs, followed by a slower
41
42
43 808 reconfiguration of the large-scale convection pattern that progresses from the dayside to the
44
45
46 809 nightside.

47
48
49
50 810
51
52
53 811 A particular transient in the solar wind dynamic pressure, known as a sudden impulse (SI),
54
55
56 812 occurs under various IMF conditions and has been studied extensively with ground-based
57
58
59
60 813 magnetometer networks. Observations show a large-scale twin-vortex and/or meso-scale pairs

1 814 of traveling convection vortices (TCVs) associated with FACs resulting from a deformation of
2
3
4 815 the magnetopause due to the abrupt change in the solar wind dynamic pressure (Araki 1977;
5
6
7 816 Friis-Christensen et al. 1988; Glassmeier et al. 1989). High-latitude SuperDARN radars have
8
9
10 817 observed TCVs (e.g., Thorolfsson et al. 2001) due to the contracted polar cap under northward
11
12
13 818 IMF. In one event, Hori et al. (2012) showed the convection electric field associated with a
14
15
16 819 TCV negative SI (and possible aftershocks) at high-latitude extending into the sub-auroral
17
18
19
20 820 region. Effects of the passage of TCVs are also seen at mid-latitudes in ground scatter returns,
21
22
23 821 as shown by Kim et al. (2012). Meanwhile, Hori et al. (2015) demonstrated using the high- and
24
25
26 822 mid-latitude SuperDARN data that there is a dawn-dusk asymmetry of flow vortices as shown
27
28
29 823 in statistical convection velocity perturbations, caused by IMF By polarity, which appears
30
31
32 824 associated with negative SI events (dynamic pressure decrease) that is not seen for positive SI
33
34
35
36 825 events. However, most of the observations were poleward of 60° MLAT and all measurements
37
38
39 826 were considered not just those associated with TCVs.

40
41
42 827
43
44
45
46 828 Other studies of transient convection phenomena include observations of bursty flows
47
48
49 829 associated with dayside reconnection, such as flux-transfer events (FTEs) (Pinnock et al. 1993;
50
51
52
53 830 Provan et al. 1998; Wild et al. 2001, 2003) - results mainly based on high-latitude SuperDARN
54
55
56 831 observations - and on the nightside associated with substorm phenomena such as auroral
57
58
59 832 beading, auroral streamers and poleward boundary intensifications (PBIs) (Lyons et al. 2011;
60

1 833 Gallardo-Lacourt et al. 2014a, 2014b; Lyons et al. 2015, 2016), with the latter studies
2
3
4 834 demonstrating a connection between enhanced nightside polar cap flows and the triggering of
5
6
7 835 PBIs, auroral streamers and substorm onset, with associated SAPS and SAID flows.
8
9

10
11 836

14 837 **Convection: Future Directions**

17 838 There are currently ten SuperDARN radars located equatorward of 50° MLAT in the northern
18
19
20 839 hemisphere. The expansion of SuperDARN to mid-latitudes has been a demonstrated success
21
22
23 840 with previously unattainable measurements of the convection electric field equatorward of ~60°
24
25
26
27 841 MLAT and associated contributions to a variety of phenomena occurring at mid-latitudes. Plans
28
29
30 842 are in place to build several more mid-latitude radars in the European and Asian sectors. These
31
32
33 843 radars will provide critical measurements in these regions, enabling near-continuous monitoring
34
35
36 844 of convection in the mid-latitude region and allowing several unanswered questions to be
37
38
39 845 addressed, such as the statistical nature of SAPS occurrence and the origins of SAPS and SAID.
40
41
42
43 846 The latter will benefit from more continuous observations at mid-latitudes but will also require
44
45
46 847 complementary measurements of the electrodynamic parameters such as the electrical current
47
48
49 848 and conductivity.

50
51
52 849

55 850 Another convection topic that mid-latitude SuperDARN will have a sizeable impact on is the
56
57
58 851 specification of statistical convection patterns or convection maps. Several studies of the
59

1 852 climatology of large-scale convection have been performed using SuperDARN observations.
2
3
4 853 These studies bin the LOS radar data according to various combinations of the IMF magnitude,
5
6
7 854 IMF clock angle, solar wind speed and dipole tilt angle in order to obtain a global solution of
8
9
10 855 the electrostatic potential that "best fits" the radar observations in each bin. As more radars
11
12
13 856 became operational the statistics for any given bin increased, thereby improving the quality of
14
15
16 857 the solutions and allowing for additional binning parameters or/and finer bin resolution.
17
18
19
20 858 Ruohoniemi and Greenwald (1996) used data from only the GBR radar to construct the first set
21
22
23 859 of statistical convection maps. Ruohoniemi and Greenwald (2005) then performed a similar
24
25
26 860 analysis using the nine high-latitude SuperDARN radars available at that time. Pettigrew et al.
27
28
29 861 (2010) reanalyzed the northern hemisphere, adding dipole tilt angle bins and separate model
30
31
32 862 patterns produced using the southern hemisphere radars, in order to study the conjugacy
33
34
35 863 between hemispheres. Finally, Cousins and Shepherd (2010) added solar wind velocity bins
36
37
38
39 864 and the ability to interpolate between discrete patterns in order to achieve a more dynamical
40
41
42 865 model of the large-scale convection in both hemispheres.
43
44
45 866
46
47
48
49 867 In all of these studies data from only the high-latitude SuperDARN radars were used, resulting
50
51
52 868 in limited data coverage in the polar cap and the mid-latitude region, particularly during
53
54
55 869 geomagnetically active periods. A new statistical model has recently been developed that uses
56
57
58 870 measurements from the polar cap and mid-latitude radars to complement the high-latitude
59
60
61
62
63
64
65

1 871 radars (Thomas and Shepherd 2018). The resulting patterns reinforce what Baker et al. (2007)
2
3
4 872 show in Fig. 9, namely that the addition of data from the mid-latitude radars has a dramatic
5
6
7 873 effect on the overall convection strength, increasing the cross-polar cap potential by as much
8
9
10 874 as 25% (40 % in Thomas and Shepherd 2018), and markedly changing the potential contours
11
12
13 875 on the nightside, where a region of westward flow extending from dusk (18 MLT) to past
14
15
16 876 midnight (24 MLT) is observed equatorward of $\sim 60^\circ$ MLAT by the mid-latitude radars.
17
18
19

20 877
21
22
23
24
25
26
27
28
29
30
31
32
33
34
35
36
37
38
39
40
41
42
43
44
45
46
47
48
49
50
51
52
53
54
55
56
57
58
59
60
61
62
63
64
65

1 878 **Ionospheric Irregularities**

2
3
4 879 The ionosphere is a weakly ionized plasma that is subject to structuring and plasma instability.

5
6
7 880 The SuperDARN HF radar technique relies on the emergence of decameter-scale irregularities

8
9
10 881 in the plasma density for generating coherent backscatter from the ionosphere. In this section

11
12
13 882 the findings to date on the occurrence, properties, and causes of the irregularities that are

14
15
16 883 commonly observed at mid-latitudes by the SuperDARN radars are reviewed. As noted

17
18
19 884 previously, the expansion of the auroral oval during disturbances can cause the mid-latitudes to

20
21
22 885 be “auroral” in nature, hence auroral-type irregularities fall within the scope of this review.

23
24
25 886 Descending in latitude, irregularities are observed to map out features near the edge of the

26
27
28 887 auroral oval, e.g., SAPS, while at lower latitudes one encounters categories of irregularities

29
30
31 888 which are distinctly sub-auroral.

32 33 34 35 36 37 889 38 39 40 41 890 **Introduction of Ionospheric Irregularities**

42
43
44 891 At auroral latitudes the ionosphere is impacted by electric fields and particle precipitation of

45
46
47 892 magnetospheric origin. The resulting perturbations from the equilibrium state of the plasma,

48
49
50 893 observable as bulk particle motions, density gradients, temperature gradients, etc., represent

51
52
53 894 sources of free energy for triggering instability in the plasma (e.g., Fejer and Kelley 1980).

54
55
56 895 Thermal fluctuations in electron density can be greatly amplified to produce the ionization

1 896 irregularities that represent viable targets for backscattering with low-power HF coherent
2
3
4 897 scatter radars. Given the nearly continuous excitation that is due to auroral processes it is no
5
6
7 898 surprise that ionization irregularities are a nearly ubiquitous feature of the auroral ionosphere.
8
9
10 899 The early SuperDARN radars were sited approximately along an arc of 60° MLAT in order to
11
12
13 900 look into the auroral region and sense these irregularities.
14
15
16
17 901
18
19
20
21
22 902 When the first radar specifically intended for making observations in the mid-latitude
23
24
25 903 ionosphere was proposed for the WAL site, the primary scientific motivation was to enable
26
27
28 904 observations of the expansion of auroral effects during geomagnetic storms, leading to the term
29
30
31 905 “StormDARN”. It was not apparent that the sub-auroral ionosphere, defined as that region lying
32
33
34 906 equatorward of the electron precipitation boundary, would provide extensive irregularity targets.
35
36
37
38 907 In fact, a category of irregularities responsible for low-velocity backscatter was found to
39
40
41 908 populate the nighttime sub-auroral ionosphere (Greenwald et al. 2006). Evidently there are
42
43
44 909 sources of plasma instability for generating irregularities with ample backscattering cross-
45
46
47 910 sections in an ionosphere that is markedly less structured and dynamic than in the auroral
48
49
50 911 regions. The term “StormDARN” has now been rendered obsolete by the attention given to the
51
52
53 912 non-storm categories of mid-latitude backscatter. Indeed, HOK, which is sited at the lowest
54
55
56 913 MLAT of any SuperDARN radar, observes irregularities that are so far removed from contact
57
58
59
60
61
62
63
64
65

1 914 with auroral processes (equatorward of the Electron Precipitation Boundary (EPB) by more
2
3
4 915 than 10°) that it seemed appropriate to categorize them separately as temperate mid-latitude
5
6
7 916 irregularities.

8
9
10
11 917

12
13
14
15 918 Table 2 summarizes the categories of mid-latitude irregularities for the purposes of this review.

16
17
18 919 It should be noted that the position of the electron precipitation boundary (i.e., the auroral

19
20
21
22 920 boundary) is key to these definitions as a fixed MLAT may at different times correspond to the

23
24
25 921 auroral zone, the equatorward boundary zone (with SAPS), or to the sub-auroral region, with

26
27
28 922 pronounced differences for the physics of the ionosphere and the occurrence of irregularities.

29
30
31
32 923

33 34 35 36 37 924 **Auroral Irregularities**

38
39
40 925 During quiet geomagnetic conditions the equatorward edge of the auroral oval reaches as low

41
42
43 926 as 60° MLAT on the nightside. The ground range to the edge of the quiet-time oval on the

44
45
46 927 nightside is around 1200 km for the U.S. mid-latitude radars and around 2500 km for the

47
48
49 928 Hokkaido Pair of Radars (HOP). It is routine for the radars to generate ionospheric scatter at

50
51
52 929 the shorter ground range and relatively frequent at the longer ground range. Consequently, the

53
54
55 930 mid-latitude SuperDARN radars do observe backscatter from auroral irregularities even under

56
57
58 931 non-storm conditions but any activity observed within the oval is then likely due to propagation

1 932 modes that are less favorable for analysis than the half-hop mode. When there is significant
2
3
4 933 geomagnetic disturbance and the oval expands equatorward the mid-latitude radars encounter
5
6
7 934 the oval at nearer ranges and, under the most disturbed conditions ($Kp > 7$ for the U.S. radars),
8
9
10 935 the equatorward edge of the oval reaches to the near-range boundary of the radar FOVs. The
11
12
13 936 radar observations are then dominated by backscatter from auroral irregularities. To date, there
14
15
16 937 has not been an expansion event so extreme that the oval boundary has reached to the near-
17
18
19
20 938 range boundary of the HOP radars, which are located at the lowest MLAT among the
21
22
23 939 SuperDARN radars. It is noteworthy that the expansion that occurred for the historically
24
25
26 940 extreme event of March 1989 would have reached well beyond the near-range boundary of the
27
28
29 941 HOP radars (Rich and Denig 1992).
30
31
32
33
34 942
35
36
37
38 943 The earliest work on the occurrence of irregularities at mid-latitudes was reported with radars
39
40
41 944 in the southern hemisphere. With MLATs near 55° S TIG and UNW reach into the auroral zone
42
43
44 945 on the nightside at moderate ground ranges (~ 600 km), consequently, their observations
45
46
47 946 routinely encompass both the sub-auroral and auroral regions. Parkinson et al. (2003b)
48
49
50 947 produced maps of the occurrence of backscatter from TIG observed over one year near solar
51
52
53 948 cycle maximum and ordered by Kp . Comparing with model auroral boundaries they determined
54
55
56 949 that the bulk of the backscatter originated from within the oval although categories of both polar
57
58
59
60
61
62
63
64
65

1 950 cap and sub-auroral backscatter were also identified, as shown in Fig. 16 (Parkinson et al.
2
3
4 951 2003b). In particular, they noticed a high-velocity feature at the equatorward edge of the oval
5
6
7 952 in pre-midnight hours that would be later attributed to backscatter from SAPS. *F* region echoes
8
9
10 953 were found to be most frequent in autumn while *E* region echo occurrence peaks in winter and
11
12
13 954 summer.
14
15
16
17 955
18
19
20
21
22 956 Subsequent work in the southern hemisphere using TIG and UNW focused on *E* region
23
24
25 957 backscatter usually defined as having been collected from ranges less than about 600 km. Using
26
27
28 958 three years of data, Carter and Makarevich (2009) found a primary occurrence peak for
29
30
31 959 backscatter in the mid-morning sector (7-8 MLT) and a secondary peak in the pre-midnight
32
33
34 960 sector (20-23 MLT) for higher *Kp* values. There was evidence that the occurrence of the evening
35
36
37 961 echoes was more conditioned by the magnetic aspect geometry owing to limited refraction due
38
39
40
41 962 to low *E* region densities during disturbances. They reported two categories of echoes, one with
42
43
44 963 low velocities and no connection between velocity magnitude and spectral width and a second,
45
46
47 964 more apparent during storms, with higher velocities and a clear dependence of spectral width
48
49
50 965 on velocity magnitude. The difference in backscatter properties is almost certainly due to the
51
52
53 966 appearance of auroral irregularities within the designated range interval as the oval expands.
54
55
56
57
58 967

1 968 Carter and Makarevich (2010) extended the study of *E* region backscatter to cover a total of 15
2
3
4 969 radars over the same three-year period. As the bulk of the radars operate at high latitudes, the
5
6
7 970 contrasts with TIG were illuminating. TIG had peak occurrence at 7-8 MLT under quiet
8
9
10 971 conditions while the high-latitude radars had a broad occurrence peak extending across the
11
12
13 972 nightside with a preference for conditions of moderate disturbance. The occurrence rate fell off
14
15
16 973 steeply for TIG for $K_p > 5$. The *E* region echoes observed by TIG at sub-auroral latitudes
17
18
19 974 showed a fundamental difference from the higher latitude radars in terms of their diurnal
20
21
22
23 975 variation and its dependence on disturbance level. The implication is that storm-time
24
25
26 976 irregularities at nominally sub-auroral latitudes differ significantly from high-latitude auroral
27
28
29 977 irregularities.
30
31
32
33 978
34
35
36
37
38 979 Ponomarenko et al. (2016) reported on very near range echoes (< 300 km) seen with mid-
39
40
41 980 latitude radars. They identified meteor scatter, which peaks in the early morning hours, and a
42
43
44 981 new category of summer daytime echoes hypothesized to be due to neutral turbulence in the
45
46
47 982 lower *E* region. In addition, they identified an evening *E* region echo associated with the auroral
48
49
50
51 983 region which they attributed to precipitating energetic particles and strong electric fields. One
52
53
54 984 notes that this activity must be associated with very high levels of disturbance in order to have
55
56
57 985 auroral effects projected to such low latitudes. It was also speculated that the high-aspect angle
58
59
60
61
62
63
64
65

1 986 region (HAIR) echoes (Milan et al. 2004), previously reported at sub-auroral latitudes (Carter
2
3
4 987 and Makarevich 2009) and polar cap latitudes, might contribute to a surprisingly wide variety
5
6
7 988 of near-range echo types.
8
9
10
11 989
12
13
14
15 990 In summary, because of the long-range nature of HF propagation, SuperDARN radars at mid-
16
17
18 991 latitudes can observe backscatter from auroral irregularities even under quiet geomagnetic
19
20
21
22 992 conditions, albeit at ranges that are less favorable for study than is the case for high-latitude
23
24
25 993 radars. The more interesting applications of the mid-latitude radars are: (i) to observe and
26
27
28 994 characterize the storm-time auroral irregularities at mid-latitudes and their impacts on regions
29
30
31 995 that are usually sub-auroral, and, (ii) to compare the infrequent mid-latitude auroral
32
33
34 996 irregularities with the commonly occurring high-latitude auroral irregularities to see if
35
36
37
38 997 differences in geomagnetic inclination, density distribution, preconditioning of the ionosphere-
39
40
41 998 thermosphere system, etc., affect the conditions for ionospheric plasma instability and
42
43
44 999 irregularity formation. The work to date has demonstrated that the nature of the backscattering
45
46
47 1000 changes when the oval expands and auroral irregularities begin to appear in the nearer ranges
48
49
50
51 1001 of the radars. Some results on *E* region auroral irregularities have been obtained from the
52
53
54 1002 observations in the southern hemisphere. There is still clearly much to do, especially for *F*
55
56
57 1003 region irregularities. An example of a promising direction is to relate the occurrence of storm-
58
59
60
61
62
63
64
65

1 1004 time irregularities to scintillations on GNSS signal. Another is to conduct joint observations
2
3
4 1005 with mid-latitude incoherent scatter radar to obtain the necessary plasma diagnostics to
5
6
7 1006 determine whether the irregularity types and instability mechanisms that have been studied at
8
9
10 1007 high latitudes can account for the mid-latitude irregularities.
11
12
13
14
15 1008

16
17
18
19 1009

SAPS Irregularities

20
21
22 1010 Descending in latitude from the auroral zone, the electron precipitation boundary is encountered
23
24
25 1011 and sets the location of the equatorward auroral boundary. Within the vicinity of this boundary
26
27
28 1012 a distinctive convection feature is often observed, the SAPS. SAPS is characterized by high
29
30
31 1013 westward velocity (hundreds to thousands of m s^{-1}), a narrow extent in latitude (a few degrees),
32
33
34 1014 and extension in the east-west direction of thousands of kilometers. It is believed to be
35
36
37 1015 associated with an equatorward displacement of the ion precipitation boundary from the
38
39
40
41 1016 electron precipitation boundary, whence it earns its designation as sub-auroral. However, it is
42
43
44 1017 quite clearly associated with the auroral boundary and its physical nature is so distinct from
45
46
47 1018 both higher auroral latitudes and lower sub-auroral latitudes as to be considered a distinct
48
49
50 1019 category for the purpose of discussing irregularities and their properties. A detailed treatment
51
52
53 1020 of SAPS as observed by the mid-latitude SuperDARN radars is given in the “Convection”
54
55
56 1021 section; here, the implications for understanding this category of mid-latitude irregularities are
57
58
59
60
61
62
63
64
65

11022 briefly reconsidered.
2
3
4
51023
6
7
8
91024 It appears that SAPS produce small-scale irregularities and that propagation conditions under
10
11
121025 normal conditions do not seriously limit their detection, at least for the U.S. mid-latitude radars.
13
14
151026 The SAPS flow channel is associated with the mid-latitude trough, as was seen clearly in the
16
17
18
191027 example presented by Clausen et al. (2012) using TEC data. Thus, both large electric fields and
20
21
221028 steep density gradients are available during SAPS events to destabilize the plasma and generate
23
24
251029 irregularities. An obvious candidate mechanism is the gradient drift instability (GDI). At F
26
27
281030 region altitudes this instability has a positive growth rate if the plasma drift has a component in
29
30
311031 the direction of the density gradient. The nominal combination of westward SAPS flow and
32
33
341032 poleward orientation of the poleward wall of the trough would not seem favorable. However, a
35
36
37
381033 careful examination of actual events might reveal a small but sufficient degree of alignment.
39
40
41
421034
43
44
45
461035 In summary, the SAPS phenomenon is critical for our understanding of magnetosphere-
47
48
491036 ionosphere-thermosphere coupling. It is a well-defined, repeatable, and somewhat predictable
50
51
52
531037 feature of the ionosphere particularly under disturbed conditions. The high visibility of SAPS
54
55
561038 to HF coherent scatter radar must be due to the self-generation of small-scale irregularities.
57
58
591039 Determining the instability mechanism responsible would represent a significant advance for
60
61
62
63
64
65

1 1040 our understanding of plasma instability and attract the attention of a wider plasma physics
2
3
4 1041 community. More joint studies with systems that can provide diagnostic measurements (Low
5
6
7 1042 Earth Orbit: LEO satellites, Incoherent Scatter Radars: ISRs) should be sought and a challenge
8
9
10 1043 could be issued to ionospheric modelers to reproduce the full spectrum of SAPS-related effects,
11
12
13 1044 including the occurrence of small-scale irregularities in the mid-latitude SuperDARN radar
14
15
16 1045 observations.
17
18
19
20
21 1046

22
23
24

25 1047 **Sub-auroral Irregularities**

26
27
28 1048 The region of the ionosphere that extends equatorward of the electron precipitation boundary
29
30
31 1049 is conjugate to the inner magnetosphere and lacks obvious strong sources of electric field.
32
33
34 1050 Studies with ISRs have revealed the existence of 1-2 mV m⁻¹ electric fields corresponding to
35
36
37
38 1051 drifts measured in tens of meters per second. No significant particle precipitation occurs at these
39
40
41 1052 latitudes and so the ionospheric density distribution is far less subject to structuring and the
42
43
44 1053 formation of density gradients. These conditions would seem unpromising for the onset of
45
46
47 1054 plasma instability leading to irregularities especially at the decameter scale lengths necessary
48
49
50 1055 for generating HF coherent backscatter. Nonetheless from the earliest observations with the
51
52
53
54 1056 first purpose-built mid-latitude radar (WAL) it was clear that the nightside sub-auroral
55
56
57 1057 ionosphere often generates backscatter (Greenwald et al. 2006). The activity persists for hours
58
59
60

11058 at a time and is associated with low Doppler velocities. The Greenwald et al. (2006) study
2
3
41059 utilized complementary observations with the Millstone Hill ISR to argue that the irregularities
5
6
71060 could be due to, or enhanced by, the Temperature Gradient Instability (TGI) which requires
8
9
101061 oppositely directed electron density and electron temperature gradients. Figure 17 (Greenwald
11
12
131062 et al. 2006) shows the intensification of backscatter on a beam of WAL that was directed
14
15
161063 towards Millstone Hill that followed a reversal in the electron temperature gradient in the F
17
18
191064 region ionosphere at the time indicated. This event was re-examined by de Larquier et al. (2014).
20
21
22
231065 By taking account of the substantial tilt of the mid-latitude geomagnetic field lines they
24
25
261066 determined that the TGI growth conditions were in fact satisfied in the F region for the duration
27
28
291067 of the experiment. They attributed the weakness of the earlier activity to the shorting effect of
30
31
321068 daytime E region conductivity. A companion paper by Eltrass et al. (2014) examined the source
33
34
35
361069 of the irregularities during this event in terms of first-principles plasma physics. They developed
37
38
391070 the kinetic dispersion relations for the TGI and the GDI in the frequency regime of the
40
41
421071 SuperDARN radars and solved for the growth rates in both the meridional and perpendicular
43
44
451072 directions. They determined that the growth rate for the TGI was much higher than that of the
46
47
481073 GDI throughout the event. It was suggested that instability in the topside F region leads to
49
50
51
521074 growth of km-scale irregularities that mapped via their electric fields to lower altitudes and
53
54
551075 populated the F region with smaller-scale irregularities through a process of cascading. This
56
57
581076 series of papers culminated in a study by Eltrass et al. (2016) that carried the earlier analysis
59
60
61
62
63
64
65

11077 into the nonlinear (saturation) regime by applying a gyrokinetic simulation model involving
2
3
41078 particle-in-cell (PIC) calculations with Monte Carlo collisions. They found that conditions were
5
6
71079 favorable for linear growth in the kilometer-scale regime and turbulent cascade to decameter–
8
9
101080 scale irregularities in the saturation stage. Analysis of GPS scintillation data revealed a spectral
11
12
131081 index n , where the density perturbations δN can be represented by a power law of
14
15
16
171082 wavenumber k^{-n} , of about 2 for the mid-latitude irregularities with scale sizes less than a few
18
19
201083 kilometers.
21
22
23
241084
25
26
27
281085 Sub-auroral ionospheric backscatter was initially confused with ground scatter because of its
29
30
311086 low velocities and narrow spectral widths. The algorithm that had been developed at high
32
33
34
351087 latitudes for distinguishing between the two types of backscatter in routine work was found to
36
37
381088 be inadequate. Ribeiro et al. (2011) developed a new technique based on a “depth first search”
39
40
411089 method of identifying discrete events and their start and stop times and the locations of their
42
43
441090 boundaries in range (see the “Propagation Analysis: Backscatter Classification and Geolocation”
45
46
471091 subsection for details). These authors also coined the expression Sub-Auroral Ionospheric
48
49
50
511092 Scatter (SAIS) to identify this type of activity. Ribeiro et al. (2012) applied the technique to
52
53
541093 several years of observations with BKS and found that SAIS is confined to local nighttime and
55
56
571094 occurs on about 70% of nights. The absence of SAIS during sunlight was attributed to the
58
59
60
61
62
63
64
65

11095 shorting effect of a conducting E layer.
2
3
4
51096
6
7
8
91097 de Larquier et al. (2013) performed a study of the altitude of the irregularities causing SAIS
10
11
121098 using well-calibrated elevation angle data from BKS. They found that the primary source region
13
14
151099 extends between 200 and 300 km in altitude, i.e., occupies the bottomside F region. Figure 18
16
17
18
191100 shows an example of the variation of the altitude of SAIS irregularities with range from a radar
20
21
221101 (de Larquier et al. 2013). It was determined that the spatial distribution of SAIS backscatter
23
24
251102 within radar scans is primarily a function of propagation conditions and magnetic aspect
26
27
281103 geometry implying that the irregularities are widely distributed in the horizontal dimension.
29
30
31
321104 In the southern hemisphere the statistical study of the occurrence of backscatter with TIG
33
34
351105 reported by Kane et al. (2012) is relevant to this discussion of sub-auroral irregularities. They
36
37
38
391106 found a decrease in quiet-time F region backscatter when the Pedersen conductance modeled
40
41
421107 on the basis of IRI is high, as shown in Fig. 19. This finding is a convincing demonstration of
43
44
451108 the shorting effect of a conducting E layer on the occurrence of small-scale mid-latitude F
46
47
481109 region irregularities.
49
50
51
521110
53
54
55
56
571111 Ruohoniemi et al. (1988) described GBR radar observations of a sub-auroral backscatter feature
58
59
60

11112 that regularly occurs near dusk. Subsequently, the topic was treated comprehensively over
2
3
41113 many radars and the backscatter named by Hosokawa et al. (2001) as Dusk Scatter Event
5
6
71114 (DUSE). Hosokawa and Nishitani (2010) applied HOK and KSR data to determine that the
8
9
101115 center of DUSE corresponds to the minimum of a modelled trough, indicating an association
11
12
131116 with the poleward wall of the trough. Once again, the strong density gradient in the poleward
14
15
161117 wall of the trough is thought to play a role in generating irregularities.
17
18
19
20
211118
22
23
24
251119 In summary, the occurrence of coherent backscatter using the mid-latitude radars from latitudes
26
27
281120 equatorward of the equatorward edge of the auroral oval is now well-established. One category,
29
30
311121 namely SAIS, is a prominent feature of the nightside observations. It is characterized by low
32
33
34
351122 Doppler velocities and small spectral widths such that care must be exercised to discriminate it
36
37
381123 from ground scatter. A number of observational results indicate that the conducting E layer
39
40
411124 during the day suppresses the occurrence of F region irregularities. Theoretical work has
42
43
441125 demonstrated that the TGI and GDI combined with turbulent cascade can account for SAIS.
45
46
471126 More varieties of sub-auroral backscatter have been reported. It is noted that the sub-auroral
48
49
50
511127 ionosphere has advantages over the high-latitude ionosphere for resolving the background
52
53
541128 plasma parameters with sufficient confidence and precision to test ideas of plasma instability.
55
56
571129 One research direction would be to model on first principles the shorting effect of E region
58
59
60

11130 conductivity. Another would be to adapt the modelling work performed on SAIS events to
2
3
41131 routinely account for the occurrence or non-occurrence of SAIS.
5
6
7

81132
9

10
11

121133 **Temperate Mid-latitude Irregularities**

13
14
15

161134 The SuperDARN radars on Hokkaido are located at $\sim 37^\circ$ N MLAT which is more than 10°

17
18

191135 lower than the latitudes of the U.S. mid-latitude radars. This difference is comparable to that

20
21

221136 between the auroral and U.S. radars. Consequently, it seems appropriate to allow for the

23
24

251137 possibility of significant variations between the ‘higher’ sub-auroral latitudes and the ‘lower’

26
27

281138 sub-auroral latitudes observed by the HOP radars. The irregularities encountered routinely in

29
30

311139 HOK/HKW observations are designated as temperate mid-latitude in type.

32
33
34
35

361140

37
38

39
401141 Ogawa et al. (2009) described backscatter from the *E* and *F* regions on the nightside that is
41
42

431142 associated with the passage of Medium-Scale Traveling Ionospheric Disturbances (MSTIDs)
44
45

461143 through the radar FOV. Figure 20 shows an example. The MSTIDs were found to be
47
48

491144 propagating in southeast / southwest directions with phase speeds of $120\text{-}170\text{ m s}^{-1}$ and
50
51

52
531145 horizontal wavelengths of $300\text{-}600\text{ km}$. Some activity showed a clear linkage between *F* region
54
55

561146 Doppler velocity variations and alternations in power visible as striations in time-range plots.
57
58

591147 The *F* region observations were interpreted in terms of $\mathbf{E} \times \mathbf{B}$ instability at the bottom of the *F*
60
61

62
63
64
65

11148 region where the background electric field is modulated by the polarization field generated
2
3
41149 through interaction of the MSTID-induced neutral wind with the ionospheric plasma as
5
6
71150 explained in detail in Suzuki et al. (2009). It was conjectured that the E region echoes could be
8
9
101151 attributed to electrical coupling of the E and F regions. Suzuki et al. (2009) examined a similar
11
12
131152 event with a southwest propagating MSTID with a phase speed of 100 m s^{-1} and a horizontal
14
15
161153 wavelength of 300 km. The alternations in Doppler velocity reached magnitudes of $50\text{-}60 \text{ m s}^{-1}$.
17
18
19
201154 Airglow data were consistent with the radar observations of striations, propagation, and speed.
21
22
231155 The observations were interpreted in terms of the GDI acting at the base of the F layer with an
24
25
261156 eastward component of the electric field. A schematic for the instability is shown in Fig. 21
27
28
291157 (Suzuki et al. 2009). The total electric field consists of the F region dynamo field, \mathbf{E}_0 , and the
30
31
321158 $\mathbf{u} \times \mathbf{B}$ component generated by the background thermospheric winds. Modulation of \mathbf{u} by the
33
34
35
361159 neutral gas motions generated by MSTIDs generates polarization electric fields parallel or
37
38
391160 antiparallel to the propagation directions. The alternating polarization fields, through $\mathbf{E} \times \mathbf{B}$ drifts,
40
41
421161 cause variations in the Doppler shifts with opposite signs for the enhanced/depleted echo power,
43
44
451162 which also vary due to modulation of the GDI.
46
47
48
491163
50
51
52
53
541164 Koustov et al. (2014) made a statistical study of the HF radar signatures of nighttime MSTIDs
55
56
571165 at near ranges corresponding to E region backscatter. They found a reversal in the sense of
58
59
60
61
62
63
64
65

11166 propagation through midnight from southward-southwestward (toward the radar) to northward-
2
3
41167 northeastward (away from the radar). The average speeds for the two categories are 85 m s^{-1}
5
6
71168 and 56 m s^{-1} , respectively. The progression in phase fronts is apparent in both the velocity and
8
9
101169 backscattered power data and amplitude and velocity are linearly related. The MSTID motion
11
12
131170 is attributed to gravity waves propagating through the radar FOV. It is speculated that neutral
14
15
161171 turbulence plays a role in generating the *E* region backscatter during the events.
17
18
19
20
211172
22
23
24
251173 Yakymenko et al. (2015) studied the statistical characteristics of short-range echoes observed
26
27
281174 by HOK generally. Echo occurrence increases at night and there is a category of backscatter
29
30
311175 that occurs in summer in the morning-prenoon sector that can be associated with sporadic *E*
32
33
341176 layers. The irregularities are attributed to the GDI. Echo occurrence does not depend on *Kp* or
35
36
37
381177 *Dst* but is anti-correlated with the *Ap* index indicating that local factors and not high-latitude
39
40
411178 drivers are responsible for the onset of irregularities. The authors suggest that a significant
42
43
441179 number of these echoes are generated at rather high magnetic aspect angles of several degrees.
45
46
471180 They argue that non-GDI mechanisms such as neutral turbulence must account for the
48
49
50
511181 appearance of irregularities that are not strongly magnetic field aligned. The passage of
52
53
541182 MSTIDs and the onset of meridional winds are also proposed as generators of ionospheric
55
56
571183 irregularities.
58
59
60
61
62
63
64
65

11184
2
3
4
51185
6
7
81186
9
10
111187
12
13
141188
15
16
171189
18
19
20
211190
22
23
241191
25
26
271192
28
29
301193
31
32
33
341194
35
36
371195
38
39
40
41
42
43
44
45
46
47
48
49
50
51
52
53
54
55
56
57
58
59
60
61
62
63
64
65

In summary, the most-studied type of temperate mid-latitude irregularity is that associated with the passage of nighttime MSTIDs. Both Doppler velocity and backscattered power are well ordered by wave characteristics. There has been some success in attributing the formation and properties of the *F* region irregularities to the GDI with modification of the ionosphere by polarization fields that are due to MSTID-induced neutral winds. A variety of echo types is seen at near ranges and neutral winds, either through turbulence or passage of MSTIDs, are thought to play a significant role in the generation of *E* region irregularities. Two directions for future research are: (i) comparison with observations of MSTIDs and their relation to irregularity formation at higher latitudes, and, (ii) modeling of the ionospheric physics to account for the generation of irregularities and the properties of the backscatter during these events.

11196 **HF Propagation Analysis**

2
3
41197 One avenue of research that has matured significantly since the advent of mid-latitude
5
6
71198 SuperDARN is the use of HF propagation analysis for value-added research. These studies have
8
9
101199 built upon previous efforts at high latitudes which used propagation analysis to investigate
11
12
131200 ionospheric irregularities (e.g., Milan and Lester, 2001), meteor echoes (e.g., Hall et al. 1997),
14
15
161201 and traveling ionospheric disturbances (TIDs) (e.g., Bristow et al. 1996). Propagation analysis
17
18
19
201202 has several distinct advantages at mid-latitudes, which are summarized in this section, along
21
22
231203 with some of the key research results.

261204 **Introduction of HF Propagation Analysis**

27
28
291205 **Introduction of HF Propagation Analysis**
30
31
32
331206 HF propagation analysis can be broadly defined as any attempt to precisely determine the
34
35
361207 refractive pathways (or “modes”) connecting an HF radar to its backscatter targets. At relatively
37
38
391208 close-ranges, the propagation path tends to be quasi-linear and thus specified completely by the
40
41
421209 slant range and angle of arrival measurements. However, as the range to the target increases,
43
44
451210 accurate specification of the propagation mode becomes increasingly more ambiguous because
46
47
48
491211 the amount of ionospheric refraction depends on the electron density which is a highly variable
50
51
521212 function of altitude, latitude, LT, and geomagnetic conditions. For this reason, propagation
53
54
551213 analysis at ranges beyond a few hundred kilometers is typically done using simulations from
56
57
581214 an HF ray-tracing code (e.g., Jones and Stephenson, 1975) coupled with an empirical

1 1215 ionosphere model such as IRI (e.g., Bilitza et al. 2014).

2
3

4 1216

5
6

7 1217 The over-arching purpose of propagation analysis tends to fall into three broad categories: (1)

8
9

10 1218 backscatter classification and geolocation, (2) ionospheric morphology and dynamics, and (3)

11
12

13 1219 radar performance assessment and calibration. The studies reviewed in this section are therefore

14
15

16 1220 categorized under these three subsection headings. To minimize overlap with other sections the

17
18

19 1221 focus of the discussion here is primarily on how propagation analysis has been used as a tool to

20
21

22 1222 improve a methodology and/or scientific interpretation of radar data.

23
24

25 1223

26
27

28 **Propagation Analysis: Backscatter Classification and Geolocation**

29
30

31 1224 A central challenge of SuperDARN data analysis has always been how best to distinguish

32
33

34 1225 ground scatter from ionospheric scatter. Traditionally, ground scatter has been identified by

35
36

37 1226 applying lower thresholds of a few tens of m s^{-1} on both the LOS velocity and spectral width

38
39

40 1227 (Blanchard et al. 2009). This simple approach has worked reasonably well at high latitudes

41
42

43 1228 because the ionospheric plasma tends to move at speeds of a few hundreds of m s^{-1} , and is thus

44
45

46 1229 more easily distinguishable from the ground, in most situations. At mid-latitudes, however,

47
48

49 1230 typical convection speeds are much lower and comparable to the magnitude of Doppler velocity

50
51

52 1231 fluctuations expected for ground scatter in the presence of dynamic ionospheric modulations,

53
54

55 1232 such as TIDs. To overcome this ambiguity, Ribeiro et al. (2011) presented a new algorithm for

56
57

58 1233

59
60

61
62

11234 distinguishing ground and ionospheric scatter by identifying closed groupings of connected
2
3
41235 scatter points and assigning the propagation mode based on characteristics of data clusters as a
5
6
71236 whole, rather than point-by-point. Figure 22 compares the results of the traditional method (top)
8
9
101237 with the new method (bottom) for 24 hours of BKS data on 15-16 January 2010 (Ribeiro et al.
11
12
131238 2011). Ionospheric scatter is colored according to the scale on the right while ground scatter is
14
15
161239 shaded gray. Local sunrise is at ~13 UT so the left and right portions correspond to night and
17
18
19
201240 day, respectively. The lower panel shows the new algorithm produces a much more sensible
21
22
231241 classification in which there is a clear separation between bands of low velocity ionospheric
24
25
261242 scatter during the night and ground scatter during the day. This slow-moving nighttime scatter
27
28
291243 is now called SAIS.
30
31
32
331244
34
35
361245 Elevation angle data are particularly important for accurate geolocation and distinguishing
37
38
391246 various sources of backscatter. Greenwald et al. (2017) found estimates of ground range and
40
41
421247 refractive index using virtual height models are rarely consistent with results from ray tracing.
43
44
451248 Ponomarenko et al. (2016) used elevation angle data to determine near-range echoes at mid-
46
47
481249 latitudes measured by CVE and TIG. In the early morning sector these near-range echoes were
49
50
51
521250 found most likely to be meteor backscatter, whereas those near local noon during midsummer
53
54
551251 were either PMSEs or produced by lower E region neutral turbulence. In some cases,
56
57
581252 particularly statistical studies, the propagation conditions can sometimes be inferred from the
59
60
61
62
63
64
65

1 1253 context of the radar measurements themselves. For example, Parkinson et al. (2003b) examined
2
3
4 1254 the occurrence of irregularities observed by TIG over a broad range of latitudes and found,
5
6
7 1255 among other things, that nightside echoes were typically observed via 1.5-hop propagation near
8
9
10 1256 dusk and then via 0.5-hop propagation from pre-midnight to dawn.
11
12
13
14 1257
15
16
17 1258 Other studies have examined the extent to which radar detection of ionospheric backscatter
18
19
20 1259 depends on the occurrence of irregularities versus HF propagation conditions. For example,
21
22
23 1260 Kumar et al. (2011) found the range-time evolution of F region ionospheric backscatter
24
25
26 1261 measured by TIG during disturbed periods was partly dependent on changes in propagation
27
28
29 1262 conditions associated with enhanced E and F region densities. Likewise, Kane et al. (2012)
30
31
32 1263 found irregularity backscatter occurrence measured by TIG during geomagnetically quiet times
33
34
35
36 1264 was most likely controlled directly by the ionospheric density during nighttime but by both
37
38
39 1265 density and propagation conditions during the day.
40
41
42 1266
43
44
45 1267 Finally, using HF propagation analysis for accurate backscatter classification and geolocation
46
47
48 1268 can be an important component of mid-latitude SuperDARN applications totally unrelated to
49
50
51
52 1269 space science. For example, Greenwood et al. (2011) used data from TIG and UNW to show
53
54
55 1270 SuperDARN radars can remotely monitor ocean wind-wave directions from Bragg peaks in one
56
57
58 1271 or two hop sea scatters. The dominant wind-wave direction is inferred by constraining a model
59
60
61
62
63
64
65

11272 of the directional sea spectrum to the ratio of the two Bragg peaks. Good agreement was found
2
3
41273 with the WAve Model (Bender and Leslie 1994), on average, but with the radar observations
5
6
71274 exhibiting far more spatial variability and structure.

101275

11

12

13

141276

Propagation Analysis: Ionospheric Morphology and Dynamics

15

16

171277

The second broad objective of HF propagation analysis is to use radar measurements to identify

18

19

201278

perturbations in the intervening ionospheric medium, such as seasonal anomalies, storm-time

21

22

231279

effects, or TIDs. For example, de Larquier et al. (2011) used ray-tracing analysis to identify an

24

25

261280

anomaly in mid-latitude evening ground scatter measurements such that ground scatter range

27

28

291281

decreased around sunset, rather than increased, as might be expected. Millstone Hill ISR data

30

31

32

331282

confirmed that the anomalous behavior measured by BKS on one particular night was

34

35

361283

associated with elevated electron densities (see Fig. 23 from de Larquier et al. 2011). Statistical

37

38

391284

analysis showed the anomaly is most pronounced from April to September (i.e., summer).

40

41

421285

Analysis with the Horizontal Wind Model (HWM07) (Drob et al. 2008) suggests it is produced

43

44

451286

by equatorward meridional winds pushing lower layers of the ionosphere up geomagnetic field

46

47

48

491287

lines to higher altitude where recombination is slower. A later study by Milan et al. (2013)

50

51

521288

found a similar effect in FIR radar ground scatter and associated it with the Weddell Sea

53

54

551289

Anomaly (WSA) (Horvath and Essex 2003).

56

57

581290

59

60

61

62

63

64

65

1 1291 SuperDARN radars can also be used to monitor ionospheric conditions in real-time, as “oblique
2
3
4 1292 ionosondes”. This capability was first demonstrated at high latitudes by Hughes et al. (2002)
5
6
7 1293 by utilizing a special “sounding-mode” of radar operation to determine the Maximum Usable
8
9
10 1294 Frequency (MUF) and F2-layer critical frequency (f_oF_2) using variations in F region ground
11
12
13 1295 scatter skip distance as a function of frequency. This result was followed by Bland et al. (2014)
14
15
16 1296 who used TIG and UNW data to show the technique is particularly well suited at mid-latitudes
17
18
19
20 1297 because the higher ionospheric densities mean that ground scatter echoes tend to dominate over
21
22
23 1298 ionospheric echoes. Figure 24 shows the technique produces good agreement with the nearby
24
25
26 1299 ionosonde at Macquarie Island (Bland et al. 2014). However, propagation conditions play an
27
28
29 1300 important role because the technique was found to be much less effective in winter months and
30
31
32 1301 away from solar maximum when the 1-hop F region ground scatter is less distinct and harder
33
34
35
36 1302 to isolate. These problems can be overcome by using elevation angle measurements to better
37
38
39 1303 discriminate E and F region ground scatter, as well as identify contamination from low velocity
40
41
42 1304 ionospheric scatter (i.e., SAIS) and ground scatter originating from the back lobe (Milan et al.
43
44
45 1305 1997b).
46
47
48 1306
49
50
51
52 1307 Other studies have used perturbations in HF propagation conditions to infer the spatiotemporal
53
54
55 1308 response of ionospheric density to intense space weather disturbances. For example, Currie et
56
57
58 1309 al. (2016) used superposed epoch analysis to examine the range dependence of backscatter
59
60
61
62
63
64
65

1 1310 observed by TIG and Kodiak radar (KOD) during 25 intense geomagnetic storms and found a
2
3
4 1311 reduction in backscatter for middle to far ranges but an increase at close ranges. Peaks in
5
6
7 1312 absorption from a nearby riometer showed no effect on the close-range backscatter suggesting
8
9
10 1313 that this result cannot be explained by D region absorption. Instead, ray tracing analysis
11
12
13 1314 suggested enhanced E region density can over-refract middle- to low-elevation rays so they do
14
15
16 1315 not reach the F region.
17
18
19
20 1316
21
22
23 1317 Watanabe and Nishitani (2013) examined how the ionosphere responds to solar flare events by
24
25
26 1318 analyzing variations in the propagation conditions inferred from HOK data. Most flares
27
28
29 1319 produced a sudden fade-out of ground scatter echoes, consistent with increased ionization, but
30
31
32 1320 they also found positive Doppler shifts in the ground scatter just before fadeout which were
33
34
35 1321 negatively correlated with elevation angle. This behavior is consistent with increased D region
36
37
38 1322 electron density being the most dominant factor during fadeout events, rather than a lowering
39
40
41
42 1323 of reflection height due to increased F region density. The space weather impacts of solar flares
43
44
45 1324 and SuperDARN were also studied using multiple radar data in the recent literature (e.g.,
46
47
48 1325 Bergardt et al. 2018; Chakraborty et al. 2018; Fiori et al. 2018).
49
50

51
52 1326

53 54 55 1327 **Propagation Analysis: Radar Performance Assessment and Calibration**

56
57
58 1328 One reason why propagation analysis has been an under-utilized tool within the SuperDARN
59

1 1329 community is the elevation angle data collected at most radars is not routinely calibrated and
2
3
4 1330 therefore tends to be unreliable. Proper calibration requires measuring the phase offset between
5
6
7 1331 signals returning to the main and secondary antenna arrays, which is not trivial, and its value
8
9
10 1332 tends to drift over time. However, Ponomarenko et al. (2015) developed an empirical method
11
12
13 1333 for calibrating angle of arrival data using the contextual information provided within the data
14
15
16 1334 itself. Specifically, the phase offset is adjusted so that the elevation angles decrease with range
17
18
19
20 1335 in continuous bands of ground scatter data, as expected (see Fig. 25 from Ponomarenko et al.
21
22
23 1336 2015). Such calibration adjustments are necessary after each radar hardware/software update
24
25
26 1337 but also desirable on a routine basis because of gradual changes in the physical properties of
27
28
29 1338 antennas, cables, and electric circuitry.
30
31
32
33 1339
34
35
36 1340 Statistical comparisons between radar data and simulations using propagation analysis can also
37
38
39 1341 be useful for identifying deficiencies in standard SuperDARN data processing. For example,
40
41
42 1342 Oinats et al. (2016b) compared 1-hop ground scatter measurements from HOK with simulated
43
44
45 1343 data to examine the accuracy of SuperDARN echo geolocation. They found that assuming a
46
47
48 1344 fixed virtual height produces a systematic error in geolocation which has a strong dependence
49
50
51
52 1345 on LT, season, and solar activity level. They also found contamination of backscatter from the
53
54
55 1346 back lobe can be as high as 35% and tends to be most problematic in winter and equinox.
56
57
58 1347

11348 Finally, ray-tracing can also be a useful tool for demonstrating proof-of-concept for proposed
2
3
41349 new radar construction. For example, Nishitani and Ogawa (2005) used the Jones-Stephenson
5
6
71350 ray-tracing code coupled with the IRI and IGRF models to identify regions where the then-
8
9
101351 proposed HOK would most likely measure backscatter from ionospheric irregularities. Figure
11
12
131352 26 from Nishitani and Ogawa (2005) shows the results for nighttime quiet geomagnetic
14
15
161353 conditions at 9, 11 and 13 MHz with X indicating potential irregularity backscatter locations
17
18
19
201354 (i.e., $\leq 1^\circ$ aspect angle). They were able to conclude that the proposed radar would collect more
21
22
231355 than enough data to be useful as a facility for analyzing mid-latitude ionospheric irregularities.
24
25

261356

27 28 291357 **Propagation Analysis: Summary and Future Directions**

30
31
32
331358 In this subsection it has been demonstrated how HF propagation analysis can be used to conduct
34
35
361359 value-added ionospheric research at mid-latitudes and assess radar performance. The mid-
37
38
391360 latitude ionosphere provides a much simpler propagation environment than at higher latitudes,
40
41
421361 so convergence between measurements and simulated data using ionospheric models is much
43
44
451362 more likely. For this reason, small model-data disagreements can often be interpreted in terms
46
47
481363 of anomalous ionospheric behavior, deficiencies in model specification, or issues of radar
49
50
51
521364 performance.

53
54
551365

56
57
581366 Looking forward, there is scope for continued use of propagation analysis to further refine our
59
60

1 1367 understanding of mid-latitude ionospheric plasma morphology and irregularities. Two specific
2
3
4 1368 topics that deserve further examination are solar cycle effects and interhemispheric influences.
5
6
7 1369 However, such efforts will require reliable elevation angle information. Shepherd (2017)
8
9
10 1370 described an algorithm for determining elevation angle data using interferometer arrays offset
11
12
13 1371 from the main array in three dimensions, rather than one or two, thus providing more flexibility
14
15
16 1372 in the positioning of interferometer arrays for future radars.
17
18
19
20 1373
21
22
23 1374
24
25
26 1375 Finally, it is worth noting that further development and refinement of propagation analysis has
27
28
29 1376 the potential to vastly expand SuperDARN's capabilities as an asset for real-time space weather
30
31
32 1377 monitoring, beyond just specification of the ionospheric convection electric field. Specifically,
33
34
35
36 1378 a comprehensive multi-radar dataset of backscattered power measurements combined with fully
37
38
39 1379 calibrated elevation angle data could conceivably be inverted to provide hemispheric maps of
40
41
42 1380 ionospheric plasma density. Such a data product would be immensely useful to the space
43
44
45 1381 physics community, as well as the society whose activity is affected by space weather
46
47
48 1382 environment changes.
49

50
51
52 1383

53
54
55
56
57
58
59
60
61
62
63
64
65

11384 **Ion-Neutral Interactions**

71386 **Introduction of Ion-Neutral Interactions**

101387 The exchange of energy and momentum between the charged and neutral components of the
11
12
131388 Earth's upper atmosphere are manifested in ionospheric phenomena observed by SuperDARN
14
15
161389 radars. Examples include generation and propagation of TIDs, sudden onset of acoustic-gravity
17
18
19
201390 waves (AGWs), mutual momentum exchange between the ion convection and neutral winds,
21
22
231391 and generation of small-scale plasma irregularities. This section reviews mid-latitude
24
25
261392 SuperDARN radar contributions in understanding these phenomena.

331394 **TIDs: Introduction**

361395 TIDs can be initiated by a number of sources, and consequently vary over a wide range of
37
38
391396 spatial scales and propagation properties. Large-scale TIDs (LSTID) are classified as
40
41
421397 perturbations with scale sizes greater than 1000 km and having periods longer than 30 min
43
44
451398 while MSTIDs are perturbations of a smaller size and a shorter period (Hunsucker 1982). TIDs
46
47
481399 have been extensively studied using various observation techniques including ionosondes
49
50
51
521400 (Hocke and Schlegel 1996 and references therein; Crowley and Rodrigues 2012), incoherent
53
54
551401 scatter radars (Hocke and Schlegel 1996 and references therein), optical imagers (e.g.,
56
57
581402 Shiokawa et al. 2002; Shiokawa et al. 2003), and GPS receivers (Ding et al. 2008, 2011; Otsuka

11403 et al. 2011; Tsugawa et al. 2003, 2004).

2
3
41404
5
6
71405 TIDs can be identified in SuperDARN radar data as quasiperiodic range progressions of echoes
8
9
101406 in either ionospheric scatter (IS) or ground scatter (GS). An example of a TID event is shown
11
12
131407 in Fig. 27 (Grocott et al. 2013). The top panel uses ray-tracing analysis to demonstrate how
14
15
161408 wave-like perturbations in ionospheric electron density can produce selective focusing of the
17
18
19
201409 HF radar waves at specific ranges (e.g., 1800 km) so that returned signals have stronger
21
22
231410 backscattered power (Samson et al. 1990). The bottom panel shows an example of how this
24
25
261411 behavior is manifested in FIR GS data as regions of enhanced power moving toward the radar
27
28
29
301412 with a periodicity of ~ 30 min. At least 10 such excursions are visible. This signature is
31
32
331413 consistent with the previous model calculation results by Stocker et al. (2000).
34
35

361414 37 38 391415 **SuperDARN Signatures of LSTIDs**

40
41
421416 The number of LSTID events studied thus far with SuperDARN has been somewhat limited.
43
44
451417 Hayashi et al. (2010) were the first authors to conclusively identify an LSTID event, during a
46
47
48
491418 geomagnetic storm, using daytime HOK GS observations and GPS Earth Observation Network
50
51
521419 System (GEONET) network GPS data of TEC. In Fig. 28 from Hayashi et al. (2010), three
53
54
551420 large-scale density perturbations are clearly seen in the TEC data (bottom panel) with
56
57
581421 enhancements propagating equatorward (events 1 and 2) and one propagating poleward (event
59
60
61
62
63
64
65

11422 3). The speeds of the equatorward perturbations were 600 and 800 m s⁻¹, respectively, with
 2
 3
 41423 corresponding periods of 45 and 30 min. These values imply horizontal scales for the
 5
 6
 71424 ionospheric structures of 1500-1700 km. By contrast, the propagation speed for the poleward
 8
 9
 101425 propagating perturbation was 600 m s⁻¹ with a period of 75 min, implying a horizontal scale of
 11
 12
 131426 ~ 2700 km. Also, the TEC enhancements for the poleward propagating perturbation were found
 14
 15
 161427 to be several times stronger (1 TECU versus 0.4 TECU, TECU=10¹⁶ electrons m⁻²).
 17
 18
 19
 201428
 21
 22
 231429 Turning now to the HOK data (top panel, Fig. 28) it can be seen that the radar detected
 24
 25
 261430 concurrent bands of enhanced GS echoes, moving toward or away from the radar, with Doppler
 27
 28
 291431 velocity enhancements up to 50 m s⁻¹, correlated with the TEC enhancements. Furthermore, the
 30
 31
 321432 main body of the high Doppler velocity echoes showed propagation speeds comparable to those
 33
 34
 351433 inferred from the GPS data. Hayashi et al. (2010) suggested the equatorward propagating
 36
 37
 38
 391434 LSTIDs (events 1 and 2) seen in both the HOK and GPS data were signatures of AGWs
 40
 41
 421435 generated at high latitudes and propagating equatorward to mid-latitudes. Indeed, estimates of
 43
 44
 451436 the expected density perturbation amplitude based on linear AGW theory showed reasonable
 46
 47
 481437 agreement with observations for events 1 and 2 but vastly underestimated the amplitude for the
 49
 50
 511438 poleward propagating signatures (event 3). It was thus suggested that event 3 was instead an
 52
 53
 54
 551439 LSTID initiated by sources in the southern hemisphere auroral zone. This interpretation is
 56
 57
 581440 somewhat anomalous because equatorward propagation is more commonly observed for
 59
 60

11441 LSTIDs (Tsugawa et al. 2004; Ding et al. 2008). A later study by Milan et al. (2013) using the
2
3
41442 FIR radar concluded that 1-2 hour perturbations in nightside GS echoes were produced by
5
6
71443 equatorward propagating LSTIDs excited by geomagnetic disturbances at auroral or sub-
8
9
101444 auroral latitudes.

141445

171446 **SuperDARN Signatures of MSTIDs: Introduction**

18
19
201447 It has long been anticipated that MSTIDs have different sources during daytime and nighttime
21
22
231448 and thus different general characteristics (Kotake et al. 2006; Ogawa et al. 2009; Kotake et al.
24
25
261449 2007; Kelley 2011). Accordingly, after general characterization of MSTIDs, daytime and
27
28
291450 nighttime observations are considered separately.

331451

361452 **MSTID Occurrence**

37
38
391453 The vast majority of SuperDARN publications on mid-latitude MSTIDs are based on the
40
41
421454 analysis of GS signals, but a few have been identified in ionospheric scatter (IS) *F* region echoes
43
44
451455 as well (e.g., Ogawa et al. 2009; Suzuki et al. 2009). Generally, the GS occurrence changes
46
47
481456 dramatically versus season and time of day because of variations in the background ionospheric
49
50
51
521457 electron density. This tendency complicates assessment of MSTID occurrence (e.g., Grocott et
53
54
551458 al. 2013; Frisell et al. 2014). At mid-latitudes, GS is typically present during daytime, centered
56
57
581459 around noon, and decreases dramatically toward winter as the electron density in the ionosphere

11460 becomes smaller (Grocott et al. 2013; Frissell et al. 2014; Oinats et al. 2015). Thus, MSTID
2
3
41461 occurrence rates should be normalized by the rate of GS occurrence, which has only been done
5
6
71462 by Grocott et al. (2013).
8
9
101463
11
12
131464 One of the first SuperDARN publications on mid-latitude MSTIDs examined TIG sea scatter
14
15
161465 measurements during the year 2000 (He et al. 2004) and found more events occur during
17
18
191466 daytime (especially during postnoon hours) and in winter, with fewer events near equinoxes
20
21
22
231467 and even fewer in summer. This tendency is consistent with Bristow et al. (1996) who also
24
25
261468 reported more frequent auroral zone MSTID event detection in winter. Frissell et al. (2014)
27
28
291469 with the BKS data and Oinats et al. (2015) with the HOK data both concluded the MSTID
30
31
321470 occurrence rate maximizes during daytime in winter. By contrast, Grocott et al. (2013)
33
34
351471 examined normalized FIR MSTID occurrence for daytime events and found the MSTID
36
37
38
391472 occurrence rate was higher during equinoctial time (although the authors could not fully
40
41
421473 conclude with respect to winter occurrence rates because of insufficient statistics). To further
43
44
451474 complicate matters, observations with other instruments are also somewhat contradictory with
46
47
481475 respect to a preferential season and time of day for MSTID occurrence (Ding et al. 2011; Kubota
49
50
51
521476 et al. 2011; Kotake et al. 2007). Clearly, more work is needed.
53
54
551477

11478 **Typical MSTID Parameters**

2
3
41479 It has been established that the typical period, wavelength and propagation speed of MSTIDs
5
6
71480 are very comparable across the MLAT of SuperDARN observations, and in both hemispheres
8
9
101481 (He et al. 2004; Ishida et al. 2008, Grocott et al. 2013; Frissell et al. 2014, 2016; Oinats et al.
11
12
131482 2015, 2016a). Frissell et al. (2014) presented histogram distributions for these parameters based
14
15
161483 on daytime BKS observations in the American sector. Typical values were found to be 30-40
17
18
191484 min periods, 200-300 km spatial scales, 100-150 m s⁻¹ phase speeds. A follow up study (Frissell
20
21
22
231485 et al. 2016) considered a more extensive data set comprising 6 North American mid-latitude
24
25
261486 radars and 4 auroral zone radars and concluded that daytime MSTID parameters at high and
27
28
291487 mid-latitudes are generally comparable. One minor difference was more frequent occurrence of
30
31
321488 shorter-wavelength and faster moving MSTIDs at high latitudes, consistent with an earlier study
33
34
35
361489 by Ishida et al. (2008) using a more limited data set. Other studies have shown that nightside
37
38
391490 MSTIDs have typical parameters comparable to those during daytime (Oinats et al. 2015,
40
41
421491 2016a; Milan et al. 2013). Minor differences noted by Oinats et al. (2016a) are 20-30% longer
43
44
451492 periods and wavelengths of nighttime MSTIDs although the differences are difficult to quantify
46
47
481493 because the data are presented as scatter plots. Data presented by Oinats et al. (2015) seem to
49
50
511494 suggest that nighttime MSTIDs during summer have larger propagation speeds, by at least 30%.

11496 **Daytime MSTIDs: Introduction**

2
3
41497 Establishing the direction of MSTID propagation is fundamentally important for locating
5
6
71498 potential sources and for understanding the mechanisms of MSTIDs generation.
8
9

101499
11
12
131500 **Daytime MSTIDs: Propagation Direction**

141500
15
161501 A number of SuperDARN studies have assessed the direction of daytime MSTID propagation
171501
18
19
201502 observed by individual radars. For example, Ishida et al. (2008) analyzed HOK and KSR data
21
22
231503 and found a great deal of similarity between the propagation directions of MSTIDs in the
24
25
261504 auroral zone and at mid-latitudes, namely toward the south-east or south-west. Frissell et al.
27
28
291505 (2014) analyzed BKS observations and identified two semi-distinct populations of daytime
30
31
321506 MSTIDs propagating over North America: a major component propagating south-east ($az=$
331506
34
35
361507 150° , where az is the angle between the propagation direction and geographic north, positive
37
38
391508 clockwise) and a minor population propagating north-west ($az=-50^\circ$). The dominant south-
40
41
421509 east propagation direction has been further confirmed by Frissell et al. (2016) using data from
43
44
451510 6 mid-latitude North American radars. Observations with FIR (Grocott et al. 2013) and TIG
46
47
481511 (He et al. 2004) are consistent with this result in the sense that the majority of MSTIDs
491511
50
51
521512 propagate toward the equator with some eastward component. However, it is important to
53
54
551513 emphasize that numerous studies have reported minor populations of MSTIDs propagating in
56
57
581514 seemingly “anomalous” directions which are likely associated with local factors. For example,
59
60
61
62
63
64
65

11515 Grocott et al. (2013) identified a persistence of MSTIDs propagating westward and related them
2
3
41516 to AGW generation by either the Andean and Antarctic Peninsula mountains or the polar vortex.
5
6
71517 Ishida et al. (2008) also detected occasional MSTIDs propagating westward and south-east
8
9
101518 which were thought to be related to meteorological phenomena above the troposphere. He et al.
11
12
131519 (2004) showed occasional occurrence of poleward-propagating MSTIDs.
14
15
16
171520
18
19
201521 Oinats et al. (2015) performed extensive analysis of MSTID propagation directions by
21
22
231522 considering skip distances of the HOK GS echoes. Four major directions were identified. Two
24
25
261523 directions were found to dominate near noon: south and south-west in winter and north-east in
27
28
291524 summer (see their Fig. 2). In a follow up study, Oinats et al. (2016a) found that the second
30
31
321525 cluster corresponds to MSTIDs at short radar ranges reflecting disturbances in the *E* region (see
33
34
35
361526 their Fig. 2).
37
38
391527
40
41
421528 One working hypothesis for the preferential direction of observed MSTID propagation is a
43
44
451529 filtering effect of neutral winds such that only those AGWs propagating opposite to the neutral
46
47
481530 wind flow will be detected by the radars (e.g., Kotake et al. 2007; Oinats et al. 2016a). General
49
50
51
521531 agreement of SuperDARN-inferred directions with this hypothesis has been invoked by Ogawa
53
54
551532 et al. (2009) and Grocott et al. (2013). Oinats et al. (2016a) went further by modeling the
56
57
581533 expected directions of MSTID propagation on the basis of the HWM07 neutral wind model
59
60
61
62
63
64
65

11534 (Drob et al. 2008). Figure 29 shows the expected (modeled) occurrence of MSTIDs on the
2
3
41535 azimuth-LT plane as grey-scale pixels and the actual MSTID occurrence by line contours with
5
6
71536 color signifying various rates. Both echo detection through the *E* and *F* regions are considered.
8
9
101537 For the dayside, one can see that the agreement is very good for the summer observations,
11
12
131538 slightly worse for the equinoctial observations, and much worse for the winter conditions where
14
15
16
171539 shift to the south-east directions is as large as $30^{\circ} - 50^{\circ}$.
18
19

201540

21

22

231541 **Daytime MSTID Generation: Geomagnetic Influences and Polar Vortex Activity**

24

25

261542 One classical scenario of MSTID onset is generation of AGWs due to geomagnetic activity in
27
28
291543 the auroral zone and subsequent propagation to mid-latitudes (Ogawa et al. 2002b; Ishida et al.
30
31
32
331544 2008). For the dayside, however, published papers have found mixed results regarding this
34
35
361545 scenario.
37
38

391546

40

41

421547 Ishida et al. (2008) specifically targeted geomagnetic influences through a statistical study of
43

44

451548 KSR, KOD and HOK GS signals in the auroral zone and at mid-low latitudes during periods
46

47

481549 with relatively low and high solar activity. For one quiet day event with nearly simultaneous
49

50

51
521550 monitoring of MSTIDs by all radars, the MSTID parameters, such as azimuth of propagation,
53

54

551551 speed and period, were very comparable. On the other hand, for disturbed conditions, the
56

57

581552 MSTID parameters at mid- and high latitudes were quite different. By considering multiple
59

60

61

62

63

64

65

1 1553 events, with statistics comprising 130 events in the auroral zone and 40 events at mid-latitudes,
2
3
4 1554 the authors found a great deal of similarity between the propagation directions of MSTIDs
5
6
7 1555 (although much more variability was seen for the high-latitude MSTIDs) which seems to favor
8
9
10 1556 a high-latitude source location.
11
12
13
14 1557
15
16
17 1558 Grocott et al. (2013) found almost no correlation of MSTID occurrence with magnetic storm
18
19
20 1559 activity (*SYM-H* index, 0.3 correlation coefficient) but a more pronounced correlation with
21
22
23 1560 auroral substorm activity (*AE* index, 0.57 correlation coefficient). Oinats et al. (2016a) reported
24
25
26 1561 a minor increase in the speed and the amplitude of MSTID-related perturbations with the *AE*
27
28
29 1562 index for HOK observations (although data in all LT sectors were included in their analysis).
30
31
32
33 1563
34
35
36 1564 Finally, an extensive analysis of daytime MSTID dependence on magnetic activity in the
37
38
39 1565 auroral zone by Frissell et al. (2016) resulted in a firm negative conclusion. These authors
40
41
42 1566 created a special index quantifying MSTID activity according to the intensity of power
43
44
45 1567 modulations of the GS echo power for each individual radar (10 radars were considered). They
46
47
48 1568 found negligible correlation of the introduced MSTID index with *SYM-H* and *AE* indices but
49
50
51
52 1569 high correlation with a newly defined Polar vortex index. Figure 30a from Frissell et al. (2016)
53
54
55 1570 shows variations of the MSTID index characterizing the level of GS signal power fluctuations
56
57
58 1571 for quiet periods (dotted line and blue color of the background) and periods with strong MSTID

1 1572 activity (solid line and pink color of the background). Figures 30b, c, d show temporal variations
2
3
4 1573 of the polar vortex index (calculated from the variabilities of the geopotential differences at the
5
6
7 1574 1 and 10 mb levels), *AE* and *SYM-H* indices, respectively. No visible correlation exists between
8
9
10 1575 enhanced MSTID activity and magnetic indices, while the polar vortex index shows generally
11
12
13 1576 the same trends as the MSTID index (e.g., pronounced decreases around 15 January and a
14
15
16 1577 monotonic decrease after March). Even some short-term excursions of the indices are consistent
17
18
19
20 1578 with each other. On the basis of these data, Frissell et al. (2016) concluded that the south-east
21
22
23 1579 direction of MSTID propagation over North America is due to AGW generation in the
24
25
26 1580 troposphere at the boundary regions of the active polar vortex area. They also demonstrated that
27
28
29 1581 the seasonal variation in MSTID activity is in accord with stratospheric warmings, pointing to
30
31
32 1582 the critical role of the lower atmosphere in generation of daytime MSTIDs. It was assumed that
33
34
35
36 1583 the neutral wind filtering effect controls the direction of the observed MSTIDs, in agreement
37
38
39 1584 with conclusions by other studies (e.g., Kotake et al. 2007; Oinats et al. 2016a).
40
41
42 1585
43
44
45 1586 Polar vortex activity is likely not the only source of daytime mid-latitude MSTIDs. Indeed, in
46
47
48 1587 an earlier paper, Frissell et al. (2014) discussed north-west propagating MSTIDs and related
49
50
51
52 1588 them to tropospheric convection processes over the Atlantic Ocean. Earlier, Grocott et al.
53
54
55 1589 (2013) identified the possibility of MSTID propagation from tropospheric processes over the
56
57
58 1590 mountains in Antarctica. Finally, Oinats et al. (2016a) reported that HOK often sees MSTIDs
59
60

1 1591 propagating north-west and attributed them to *E* region ionospheric perturbations, also
2
3
4 1592 propagating in unusual directions.
5
6

7 1593
8
9

10 1594 **Nighttime MSTIDs: Introduction**

11
12
13 1595 Optical and GPS TEC observations have shown that nighttime MSTIDs are a frequent
14
15
16 1596 phenomenon at mid-latitudes (e.g., Shiokawa et al. 2003; Otsuka et al. 2011). However,
17
18
19 1597 detection of nighttime MSTIDs using HF ground scatter signals is complicated by the fact that
20
21
22 1598 electron density decreases after sunset and the ground scatter echo occurrence rates plummet
23
24
25
26 1599 (e.g., Frissell et al. 2014). This effect is especially profound in winter. In addition, propagation
27
28
29 1600 conditions tend to be more complex during nighttime making definitive identification of quasi-
30
31
32 1601 periodic MSTID ground scatter patterns/range bands much more difficult. In such conditions,
33
34
35 1602 concurrent observations with other instruments such as optical imagers and/or GPS TEC
36
37
38 1603 receivers, are extremely useful. For example, Shiokawa et al. (2008) and Koustov et al. (2009)
39
40
41 1604 reported HOK GS echo bands moving equatorward in unison with optically identified MSTIDs.
42
43
44 1605 Finally, Oinats et al. (2015) found nighttime mid-latitude MSTIDs are less frequent in winter;
45
46
47 1606 however, this may be due to a general decrease in GS occurrence because optical observations
48
49
50
51 1607 show clear MSTID maxima at solstices (Duly et al. 2013 and references therein).
52
53
54
55 1608

56
57
58
59
60
61
62
63
64
65

Nighttime MSTIDs: Propagation Direction

Ichihara et al. (2013) reported nighttime MSTIDs observed by HOK usually propagate south-west but sometimes north to north-east. These latter MSTIDs occur more frequently after sunset, near the dusk terminator or in the midnight sector. The authors also found northward propagating MSTIDs are not always accompanied by similarly moving MSTIDs at lower latitudes (over central Japan), equatorward of the radar observational area. These statistical results substantiate a report by Shiokawa et al. (2008) who studied one event of north-east propagating MSTIDs during nighttime. MSTID motion seen in optical data during this event were related to the descent of the ionospheric F region identified by a concurrently operating ionosonde. HOK observed some irregularly-propagating GS progressions that could have been identified as MSTIDs, but details were not investigated.

Oinats et al. (2015) indicate that the majority of nighttime MSTIDs occur during late evening to pre-midnight hours (16-24 LT) and preferentially at equinox (see their Fig. 2). This finding is in disagreement with Duly et al. (2013). They found propagation to the south-west ($az=210^\circ$), similar to daytime MSTIDs over Japan, and pre-midnight MSTIDs occurrence consistent with the wind filtering effect (Fig. 29 from Oinats et al. 2016a). Another cluster of events during morning hours, between 3 and 5 LT (see their Fig. 2) propagate to the north-east ($az=30^\circ$). Surprisingly, these are not strong in winter, probably because of weakening in the neutral wind

1 1628 filtering effects, as predicted by Oinats et al. (2016a) (see Fig. 29b).

7 1630 **Nighttime MSTIDs: High-Latitude Geomagnetic Influences**

10 1631 One might generally expect better correlation between nighttime MSTID occurrence and high-
11
12
13 1632 latitude geomagnetic activity because the auroral oval is located at much lower magnetic and
14
15
16
17 1633 geographic latitudes on the nightside. So far, however, this expectation has not been fully
18
19
20 1634 articulated. Oinats et al. (2016a) found increased amplitude of MSTIDs with *AE* magnetic index
21
22
23 1635 in all LT sectors but individual events studied by Shiokawa et al. (2008) and Koustov et al.
24
25
26 1636 (2009, 2014) were during geomagnetically quiet conditions. Only one of the events considered
27
28
29 1637 by Ogawa et al. (2009) can be related to geomagnetic disturbances at high latitudes while two
30
31
32 1638 others occurred under very quiet conditions, according to the *Kp* and *AE* indices. These mixed
33
34
35
36 1639 findings question the importance of auroral zone sources for generating nighttime mid-latitude
37
38
39 1640 MSTIDs, similar to what has been found on the dayside.

42 1641
43
44
45 1642 Finally, it is noted that Ichihara et al. (2013) found preferential occurrence of north-east
46
47
48 1643 propagating MSTIDs near dusk (see their Fig. 4) suggesting the solar terminator may also play
49
50
51
52 1644 an important role (e.g., Afraimovich et al. 2009). This hypothesis, however, has not been
53
54
55 1645 investigated with SuperDARN data yet.

11647 **Nighttime MSTIDs: *E* Region Signatures and Vertical Coupling**

2
3
41648 Electron density perturbations propagating at *E* region heights can also be detected as MSTIDs
5
6
71649 in SuperDARN GS and IS signals. Ogawa et al. (2009) were the first authors to report MSTID
8
9
101650 signatures in *E* region ionospheric echoes as quasi-periodical striations in HOK ionospheric
11
12
131651 backscatter. Regions with enhanced echo power were found to be magnetically connected to *F*
14
15
161652 region plasma depletions as inferred from 630-nm airglow camera observations. Ogawa et al.
17
18
19
201653 (2009) suggested such a coincidence is indicative of electrodynamic coupling between these
21
22
231654 two regions in the form of a polarization electric field (Perkins 1973) which maps into the *E*
24
25
261655 region without attenuation, as envisioned theoretically (e.g., Yokoyama and Hysell 2010).
27
28
291656
30
31
321657 Koustov et al. (2014) performed a more comprehensive analysis of *E* region MSTID signatures
33
34
35
361658 in HOK echoes and reported preferential occurrence of such echoes in summer with a secondary
37
38
391659 maximum in winter. This tendency is despite the fact that *E* region nighttime HOK echoes are
40
41
421660 more frequent in winter (Yakymenko et al. 2015). The authors found the *E* region MSTIDs
43
44
451661 propagate toward the south-east or east during pre-midnight hours and toward the south-west
46
47
481662 or west during post-midnight hours with average speeds of 86 m s^{-1} and 56 m s^{-1} , respectively.
49
50
51
521663 Their typical spatial scale is $\sim 300 \text{ km}$. However, the Doppler velocity of the MSTID striations
53
54
551664 were smaller than the speed of the power enhancements implying HOK monitored extended
56
57
581665 plasma blobs moving across the FOV, presumably at the background wind velocity. Plasma
59
60
61
62
63
64
65

11666 motions inside the blobs are assumed to be controlled by a combined effect of the electric field
2
3
41667 and neutral wind, as later expanded by Yakymenko et al. (2015).
5
6
71668
8
9
101669 Several additional arguments supporting the notion of strong electrical coupling between the *E*
11
12
131670 and *F* regions during MSTID events have been identified. These include: 1) *F* region echo
14
15
161671 velocity is consistent with the expected electric field direction within regions of
17
18
19
201672 depleted/enhanced electron density (Suzuki et al. 2009), 2) *E* region plasma velocity is
21
22
231673 comparable to that in the *F* region (Koustov et al. 2014), 3) polarity of the *E* region velocity
24
25
261674 changes consistently in neighboring regions with enhanced/depleted plasma density (Ogawa et
27
28
291675 al. 2009) and 4) the power of *E* region echoes correlates with the measured Doppler velocity
30
31
321676 (Koustov et al. 2014). However, there are also several outstanding issues, including: 1)
33
34
35
361677 sometimes, the region of depleted plasma correlates with a sheared plasma flow of opposite
37
38
391678 polarities, instead of a single direction (Ogawa et al. 2009) and 2) polarity of the velocity is
40
41
421679 inconsistent with that usually observed for MSTIDs over Japan with the Middle and Upper
43
44
451680 atmosphere (MU) VHF radar (although at quite different MLAT).
46
47

481681
49

511682 **SuperDARN Detection of Seismically-Activated TIDs**

53
54
551683 With extensive spatial coverage and reasonably good temporal resolution, the SuperDARN
56
57
581684 radars can be a powerful tool for investigating ionospheric disturbances generated by sources
59
60

1 1685 outside the atmosphere. Only a few SuperDARN studies have been published thus far in this
2
3
4 1686 area, and the record will likely remain short in the case of meteorites (Berngardt et al. 2015).
5
6
7 1687 However, HF radars have been proven to be useful for tracking TIDs generated by intense
8
9
10 1688 earthquakes and tsunamis (Occhipinti et al. 2010) and the SuperDARN radars could become a
11
12
13 1689 powerful tool for more systematic studies of such disturbances, especially over oceans where
14
15
16 1690 other ionospheric measurements are not possible.
17
18
19
20 1691
21
22
23 1692 Nishitani et al. (2011) reported the first SuperDARN radar detection of ionospheric
24
25
26 1693 disturbances initiated by a major earthquake on 11 March 2011 off the Pacific coast of Tohoku
27
28
29 1694 (magnitude M=9.0). During this event, HOK was originally operating in a normal azimuth
30
31
32 1695 scanning mode but several minutes after the earthquake occurred it switched to a camping beam
33
34
35 1696 mode with a single high-resolution 8-s beam. Data obtained on the 8-s beam identified 5
36
37
38 1697 separate bands of ground scatter moving away from the radar with apparent speeds of 6.7, 6.2,
39
40
41
42 1698 4.5, 3.9 and 3.5 km s⁻¹ (see Fig. 31 from Ogawa et al. 2012). The speeds of the first two GS
43
44
45 1699 bands were faster than any MSTIDs observed previously, by any observational means, while
46
47
48 1700 the speed of the three next disturbances were found to be consistent with a scenario of surface
49
50
51 1701 Rayleigh waves propagating into the observational area and generating acoustic (air) waves that
52
53
54 1702 generate electron density perturbations as they expand upward to ionospheric heights (Ducic et
55
56
57 1703 al. 2003). Surprisingly, these kinds of waves with speed faster than 4 km⁻¹ were not seen in the

11704 TEC data. It was concluded that the radar observations were associated with up-and-down
2
3
41705 motions of the ionospheric layers as fast as 200 m s^{-1} (peak-to-peak values). Note that some of
5
6
71706 the disturbances, e.g., the one at 1512-1514 UT, were due to aftershocks rather than the main
8
9
101707 shocks, making it difficult to analyze the data in the later stage of the event.
11
12
13
141708
15
16
171709 A follow-up study of the 11 March 2011 earthquake event by Ogawa et al. (2012) examined a
18
19
201710 second class of poleward propagating backscatter power enhancements which arrived in the
21
22
231711 HOK observational area later than the Rayleigh wave perturbations and associated them with
24
25
261712 slower-moving AGWs generated at the epicenter. For these latter perturbations, no clear
27
28
291713 correlations between echo power and Doppler velocity were detected, contrary to what is seen
30
31
32
331714 for typical nighttime MSTIDs (Ogawa et al. 2009). Another interesting phenomenon was two
34
35
361715 bursts of quasiperiodic pulsations of echo LOS velocity (2-4 min period) which occurred ~105
37
38
391716 min and ~180 min after the earthquake and lasted for about 30 min. It was suggested that these
40
41
421717 so-called “acoustic resonance” pulsations were produced by acoustic waves trapped between
43
44
451718 the Earth’s surface and thermosphere modulating the ionospheric electric field and electron
46
47
481719 density (Shinagawa et al. 2007). Why two separate resonance intensifications were observed,
49
50
51
521720 however, requires further investigation.
53
54
551721

11722 **Ion-Neutral Coupling and Generation of Plasma Irregularities**

2
3
41723 The $\mathbf{E} \times \mathbf{B}$ drift of ionospheric plasma at F region heights may alter the directional motion of
5
6
71724 neutral particles (ion drag effect) and neutral winds can affect the velocity of charged particles.
8
9

101725 Several studies have attempted to identify the efficiency of these interactions and the time-
11
12
13
141726 scales on which they operate.
15

16
171727
18
19
201728 Joshi et al. (2015) investigated mid-latitude ion-neutral coupling during the geomagnetic storm
21
22
231729 of 2-3 October 2013 using co-located measurements of ionospheric convection from North
24
25

261730 American mid-latitude SuperDARN radars and neutral winds from Fabry-Perot Interferometers
27
28
291731 (FPIs). The timescales on which the coupling operates were analyzed using momentum
30
31
32
331732 exchange theory and time-lagged correlation analysis. During the main phase, they found the
34
35

361733 neutrals respond to the ion convection on a timescale of ~ 84 minutes. Figures 32a, b illustrate
37
38
391734 this result. Prior to storm onset (0140 UT) the two wind velocity vectors can be seen to oppose
40
41

421735 the $\mathbf{E} \times \mathbf{B}$ drift of plasma while several hours into the storm (0840 UT) the wind vectors have
43
44
451736 rotated into the direction of the plasma drift. The timescale of this rotation is comparable to
46
47

481737 what might be observed at high latitudes using satellite observations (Killeen et al. 1984) but
49
50
51
521738 significantly faster than what is expected from local ion-drag momentum forcing alone. This
53
54

551739 tendency suggests that other storm-time influences are important for driving the neutrals during
56
57
581740 the main phase, such as Joule heating. During the late recovery phase, however, the neutrals
59
60

11741 were observed to drive the ions without any significant time delay (Fig. 32c from Joshi et al.
2
3
41742 2015) consistent with the so-called “neutral fly wheel effect” or disturbance dynamo (Blanc
5
6
71743 and Richmond 1980).
8
9
101744
11
12
131745 The importance of the disturbance dynamo effect at mid-latitudes has also been confirmed
14
15
161746 earlier by Zou and Nishitani (2014) who found that midnight flows measured by HOK during
17
18
19
201747 winter are predominantly westward at latitudes $40^{\circ} - 50^{\circ}$ and their speed increases with the
21
22
231748 intensification of planetary magnetic activity characterized by the Kp magnetic index. They
24
25
261749 also found a ~12-hour delay in achieving maximum westward flow speed at mid-latitudes after
27
28
291750 a substorm onset in the auroral zone. This time delay is significantly longer than the estimates
30
31
321751 by Joshi et al. (2015) but still in qualitative agreement with the disturbance dynamo model by
33
34
351752 Blanc and Richmond (1980), provided that one considers the much lower latitudes of the HOK
36
37
38
391753 observations.
40
41
421754
43
44
451755 Neutral winds can also play an important role modulating mid-latitude F region electron density
46
47
481756 (de Larquier et al. 2011; Milan et al. 2013) and facilitating the generation of small-scale plasma
49
50
51
521757 irregularities through neutral wind turbulence (Gurevich et al. 1997). This process is
53
54
551758 particularly important at mid-latitudes where magnetospheric electric fields are weak.
56
57
581759 Yakymenko et al. (2015) found that the diurnal variation of HOK echo velocity at short ranges
59
60

11760 cannot be explained by variation in the $\mathbf{E} \times \mathbf{B}$ drift alone. However, by adding a neutral wind
2
3
41761 contribution to the irregularity velocity, and assuming that the irregularities were not strictly
5
6
71762 magnetic field-aligned, they were able to match the measurements with theoretical expectations.
8
9
101763 It was also noticed that the short range HOK echoes are not confined to locations of zero aspect
11
12
131764 angle which suggests wind-induced irregularities are not strongly field-aligned. Another study
14
15
161765 by Ponomarenko et al. (2016) concluded that a particular class of near range echoes observed
17
18
191766 in the prenoon sector during summer time are most likely from ionospheric irregularities
20
21
22
231767 produced by the neutral wind turbulence in the lower E region, rather than meteor echoes as is
24
25
261768 commonly assumed, because their velocity characteristics are similar to the winds.
27
28
291769
30
31
321770 Finally, mid-latitude SuperDARN radars can be used to monitor neutral processes in their own
33
34
35
361771 right, such as atmospheric tides and turbulization of icy particles at the summer mesopause.
37
38
391772 Hibbins et al. (2011) used FIR radar observations of meteor echoes to study atmospheric tidal
40
41
421773 motions in the mesosphere and found strong semidiurnal tides in winter were much stronger in
43
44
451774 the southern hemisphere compared to the northern hemisphere. They also noticed bursts of
46
47
481775 quasi 2-day activity in summer with amplitudes up to 60 m s^{-1} . Ogawa et al. (2013) reported 2
49
50
51
521776 cases of Mesosphere Summer Echoes (MSEs) detected at mid-latitudes by HOK with narrow
53
54
551777 spectral widths ($<10 \text{ m s}^{-1}$), high power ($>20 \text{ dB}$) and relatively fast Doppler velocities (up to
56
57
581778 50 m s^{-1}). These HF echoes were observed when Medium Frequency (MF) and VHF radars

11779 detected MSEs in a region several hundred kilometers westward of the HOK echo detection
2
3
41780 zone. An interpretation in terms of MSEs was further supported by the fact that temporal
5
6
71781 variations of the HF echo velocity correlated well with the wind velocity concurrently measured
8
9
101782 by the MF radar.

131783

15

16

171784 **Ion-Neutral Interactions: Summary and Future Directions**

18

19

201785 In this subsection, the contributions of mid-latitude SuperDARN radars to studies of
21
22
231786 phenomena associated with ion-neutral interactions, predominantly TIDs, have been

24

25

261787 summarized. Looking forward, there is additional need for coordinated studies in which radar

27

28

291788 observations are analyzed in conjunction with other instruments, such as GPS receivers,

30

31

321789 ionosondes, and airglow imagers. Such studies are most feasible in the East Asia and North

33

34

351790 American sectors where the density of suitable instruments is particularly high, allowing for

36

37

381791 the tracking of TID perturbations over extended ranges of latitude and longitude. There is also

39

40

411792 further scope for examining the interhemispheric conjugacy of TIDs using simultaneous

42

43

441793 observations from the southern and northern radar networks, perhaps, in conjunction with in

45

46

471794 situ measurements obtained from satellites orbiting in both the ionosphere (e.g., Swarm) and

48

49

501795 magnetosphere (e.g., Arase).

51

52

531796

54

55

56

57

58

59

60

61

62

63

64

65

MHD Waves

Introduction of MHD Waves

MHD waves are observed throughout the magnetosphere and therefore at a range of latitudes on the ground, from the equator to polar latitudes. These waves, often referred to as ULF (~1-1000 mHz) waves or geomagnetic pulsations, have many different source mechanisms which can be categorized as either external or internal to the magnetosphere. External sources include the Kelvin-Helmholtz Instability (KHI) on the magnetopause (e.g., Hughes 1994), solar wind dynamic pressure variations (e.g., Araki et al. 1997), and waves generated at the bow shock which directly propagate through the magnetosphere (e.g., Fairfield 1969). Internal sources include waves related to substorm onset (e.g., Lester et al. 1983), and wave-particle interactions where waves gain energy from particles in the magnetosphere (e.g., Chisham et al. 1992).

SuperDARN radars are particularly sensitive to MHD waves as the latter generate periodic variations of plasma drift observed as Doppler shift oscillations in the radar returns. Critically, such waves can be observed either in ionospheric scatter (Rae et al. 2005), in ground scatter (Ponomarenko et al. 2003), or in artificially stimulated ionospheric scatter (Yeoman et al. 1997).

The observations in ionospheric scatter provide direct measurements of the $\mathbf{E} \times \mathbf{B}$ velocity which is imposed by the electric field vector of the MHD wave. Care should be taken, however,

11816 in discussing the electric field variations of standing waves and comparing them with magnetic
2
3
41817 field changes because of the node-antinode relationship between them due to the presence of
5
6
71818 finite ionospheric conductivity, as pointed out by Sakaguchi et al. (2012). On the other hand, in
8
9
101819 ground scatter the observations can effectively be considered to be associated with the bulk
11
12
131820 motion of the ionospheric plasma in the vertical direction, although there are a number of
14
15
161821 processes involved here (e.g., Sutcliffe and Poole 1989). Furthermore, visualization of ULF
17
18
191822 waves in ground scatter can be problematic since the scatter have low velocities. Artificially
20
21
22
231823 stimulated ionospheric scatter occurs from intense field-aligned irregularities produced through
24
25
261824 the interaction of high-power HF radio waves with the ionospheric plasma below the waves'
27
28
291825 reflection point. However, this observational mechanism is not pertinent to mid-latitude
30
31
321826 SuperDARN radars as there are no high-power radio waves transmitters, or heaters, in the FOV
33
34
35
361827 of the existing mid-latitude radars. Finally, the standard 16 beam scan with 3-s integration along
37
38
391828 each beam (1-min temporal resolution) is prohibitive for registering oscillations at frequencies
40
41
421829 above 8.3 mHz, and consequently discretionary or special modes have been designed in order
43
44
451830 to expand the observed frequency spectrum of MHD waves, thereby demonstrating the
46
47
481831 flexibility of the SuperDARN radars.
49
50
51
521832
53
54
551833 The mid-latitude SuperDARN radars are well placed to observe the waves driven by these
56
57
581834 mechanisms. In particular they are conveniently located to observe waves which are driven by
59
60
61
62
63
64
65

1 1835 internal mechanisms such as substorms (Pi2) and wave-particle interactions (high-m Pc4-5).
2
3
4 1836 For substorms, the mid-latitude radars are not as badly affected by absorption or changing in
5
6
7 1837 propagation conditions of the HF signal due to particle precipitation into the D and E regions
8
9
10 1838 (e.g., Gauld et al. 2002) because the transmitted signals typically enter the ionosphere
11
12
13 1839 equatorward of the auroral regions. Furthermore, waves driven by wave-particle interactions
14
15
16 1840 tend to map more to the field lines which thread the *F* region of the mid-latitude radars. Finally,
17
18
19 1841 the presence of ground scatter tends to be more stable over a wider range of magnetic conditions
20
21
22
23 1842 for the mid-latitude radars than for the high-latitude ones making identification of ULF waves
24
25
26 1843 easier.

27
28
29 1844
30
31
32 1845 In this section, the observations of MHD waves by mid-latitude SuperDARN radars are
33
34
35 1846 reviewed. Pi2 and Pi1 pulsations are considered first, before discussing Pc3/4, and Pc5
36
37
38
39 1847 pulsations.

40 41 42 1848 43 44 45 1849 **Pi2 and Pi1 Pulsations**

46
47
48 1850 Studies of Pi2 pulsations are typically event-based and related to data from other instruments,
49
50
51
52 1851 both ground and space-born. In the first observations of sub-auroral Pi2 pulsations by a
53
54
55 1852 SuperDARN radar, at WAL, Gjerloev et al. (2007) found that the LOS velocity variations at
56
57
58 1853 ~56° N AACGM latitude were highly correlated with nearly co-located magnetometer

1 1854 observations at Ottawa. These authors used the relationship between the variations in magnetic
2
3
4 1855 field and those in the LOS velocity to demonstrate that a predominantly shear Alfvén mode
5
6
7 1856 wave can explain the amplitude and phase characteristics. This event occurred as part of a weak
8
9
10 1857 substorm, although observations at geosynchronous orbit suggest that there were time
11
12
13 1858 differences between the ground and space signatures, with the ground signatures leading those
14
15
16
17 1859 at geosynchronous orbit.
18
19
20 1860
21
22
23 1861 Frisell et al. (2011) presented observations of an individual Pi2 pulsation using data from BKS
24
25
26 1862 in a special high time resolution mode which was implemented to support the Time History of
27
28
29 1863 Events and Macroscale Interactions during Substorms (THEMIS) mission. In this mode each
30
31
32
33 1864 radar operated a scan with 3s integration times along each beam, but with a special beam, the
34
35
36 1865 camping beam, being sampled after every other beam. Thus, the full scan would take 2 minutes
37
38
39 1866 while there was a 6-s time resolution on the camping beam which in this case for BKS was
40
41
42 1867 beam 7. The BKS observations of the Pi2 wave were between 54° and 58° N MLAT, close to
43
44
45 1868 the latitude of the Remus magnetometer station which observed temporal variations similar to
46
47
48 1869 those in the Doppler velocity of the ionospheric scatter detected by the radar. A cross-phase
49
50
51
52 1870 analysis of magnetometer data over a range of latitudes indicates that these observations were
53
54
55 1871 made very close to the ionospheric projection of the plasmapause. Fine spatial and temporal
56
57
58 1872 details in the signature of the wave in the radar scatter suggest that there were periods when all

1 1873 ranges would see the onset of an enhancement in the velocity, while subsequently there would
2
3
4 1874 be evidence of a dispersion in the signature across latitudes. The authors interpreted this in
5
6
7 1875 terms of field-line compressions which occur when there is coherence in the radar scatter while
8
9
10 1876 at the time of the dispersion there is a relaxation of the field. Furthermore, THEMIS
11
12
13 1877 observations of ion velocities by electrostatic analyzers (McFadden et al. 2008) indicated two
14
15
16 1878 bursty bulk flows (BBFs) separated by 135 s which occurred about 1 minute before the Pi2
17
18
19 1879 event. Comparison of the LOS velocity at a variety of ranges along beam 7 of BKS
20
21
22
23 1880 demonstrates an interesting effect in the profile of each of the first two peaks of the Pi2 pulsation
24
25
26 1881 in the radar data (Fig. 33 from Frissell et al. 2011). In both cases the waveforms started
27
28
29 1882 coherently as they moved toward the maximum value in the case of the second pulse and the
30
31
32 1883 whole first half of the wave cycle in the case of the first pulse. On the subsequent parts of the
33
34
35 1884 wave, however, there was a more dispersed signature as the traces relaxed to the lowest velocity
36
37
38
39 1885 on different time scales, which increased with increasing range. Frissell et al. (2011) interpreted
40
41
42 1886 these observations as the initial part of the wave pulse responding to the compression created
43
44
45 1887 by the passage of the BBF, while the lack of coherence was explained by the fact that the traces
46
47
48 1888 from the longer field lines, farther ranges, took longer time due to the longer field lines. This
49
50
51 1889 interpretation is indicative of the response to the BBF compression as it passed over the field
52
53
54 1890 lines and then a relaxation after the BBF had passed.
55

58 1891

59
60
61
62
63
64
65

1 1892 By comparing the variations in the ionospheric velocity measured by TIG and UNW with the
2
3
4 1893 magnetometer observations at MacQuarie Island (albeit at 65° S), Ponomarenko and Waters
5
6
7 1894 (2013) made the first direct observations of Pi2 wave polarization transition between
8
9
10 1895 ionosphere and ground. A special three-beam mode was employed in this study and use of a
11
12
13 1896 Hilbert transform revealed dynamics of the Pi2 evolution. The authors found for this particular
14
15
16 1897 event, which has a frequency of ~7.5 mHz, an approximate linear polarization of Pi2 transferred
17
18
19 1898 from the ionosphere to the ground with a 40° rotation of the polarization ellipse, rather than the
20
21
22 1899 conventional 90° suggested in earlier works (e.g., Southwood and Hughes 1983), which
23
24
25 1900 indicates that the conductivity profile is not as simple as originally modelled.
26
27
28
29 1901
30
31
32 1902 In a pair of papers Teramoto et al. (2014, 2016) presented two further case studies of Pi2
33
34
35 1903 pulsations using data from the THEMIS mode. In the first (Teramoto et al. 2014) a Pi2 wave
36
37
38 1904 was observed by HOK in the ground / sea scatter, which was reflected via the ionospheric *F*
39
40
41 1905 region, as well as from a sporadic *E* layer. The observations in the two different data sets had
42
43
44 1906 the same period, 110 s, and there appears to be no phase lag. The authors suggested that the
45
46
47 1907 concept of a pure cavity mode is not sufficient to explain the radar and coincident magnetometer
48
49
50
51 1908 observations and that a contribution from an Alfvén mode must be considered in order to
52
53
54 1909 explain the observations.
55
56
57
58 1910

1 1911 In a second study, Teramoto et al. (2016) presented observations from 3 radars, HOK, TIG and
2
3
4 1912 UNW, together with ground magnetometer data and electric and magnetic field observations
5
6
7 1913 by the THEMIS A, D and E spacecraft. Note that, to date, this represents the only study of
8
9
10 1914 MHD waves at any latitude which use radar data from the two hemispheres. The
11
12
13 1915 interhemispheric radar observations were made near the plasmopause and are critical for the
14
15
16 1916 understanding of the event. An analysis of the THEMIS spectra indicated that two frequencies
17
18
19 1917 were present in the event under study, at 14 mHz and 28 mHz. Ground magnetometers do not
20
21
22 1918 appear to observe the higher frequency wave but spectral maxima at both frequencies are seen
23
24
25 1919 in the radar observations. TIG is key here because it made observations both inside and outside
26
27
28 1920 of the plasmopause, while UNW and HOK observed only inside the plasmopause. TIG observed
29
30
31 1921 frequencies inside the plasmopause (14 and 28 mHz) which are different from those outside of
32
33
34 1922 it (14 mHz only), while inside the plasmopause HOK only observed the lower spectral
35
36
37 1923 frequency and UNW measured the lower spectral frequency at lower latitudes and higher
38
39
40 1924 spectral frequency further poleward. The estimations of Poynting flux at THEMIS indicate that
41
42
43 1925 the waves were propagating earthward and duskward. The authors concluded that the observed
44
45
46 1926 wave was a cavity mode resonance which had been stimulated by compressional waves which
47
48
49 1927 had propagated duskward from the source region in the midnight sector.
50
51
52 1928
53
54
55 1929 Shi et al. (2017) provided a careful and thorough analysis of multiple data sets from THEMIS,
56
57
58
59
60
61
62
63
64
65

1 1930 ground magnetometer, and FHE, FHW and BKS. Shi et al. (2017) attempted here to separate a
2
3
4 1931 plasmaspheric virtual resonance (PVR) where wave energy is primarily confined to the
5
6
7 1932 plasmasphere but a small portion escapes beyond the plasmopause, from a plasmaspheric cavity
8
9
10 1933 resonance (PCR) where wave energy should be confined to the plasmasphere. The radar data
11
12
13 1934 are key as they provide high spatial resolution across the plasmopause as shown in Fig. 34 from
14
15
16 1935 Shi et al. (2017), where the wave phase and power are taken across a number of range gates of
17
18
19 1936 data from FHE. The peak in power occurs at 60.6° N which is just inside the estimated position
20
21
22
23 1937 of the plasmopause at 60.9° N, while a minimum in power occurs at 59.60° N. The main phase
24
25
26 1938 change occurs between 59.8° N and 59° N. This tendency suggests that the wave is not a field
27
28
29 1939 line resonance (FLR). The authors also concluded that the source mechanism is related to the
30
31
32 1940 downward FAC in the Substorm Current Wedge (SCW).
33
34
35
36 1941
37
38
39 1942 So far, the only observation of Pi1 pulsations by a SuperDARN radar were made at WAL while
40
41
42 1943 testing a new high-resolution multi-pulse mode (Greenwald et al. 2008) when electric field
43
44
45 1944 pulsations with periods between 13 and 20 s were observed during a substorm expansion phase.
46
47
48 1945 Magnetometer data at Ottawa revealed simultaneous magnetic pulsations with the same period
49
50
51
52 1946 (Fig. 35 from Greenwald et al. 2008). The top panel of Fig. 35 is a contour plot of the spectral
53
54
55 1947 power from a wavelet analysis of the Ottawa X (geographic north-south) component data which
56
57
58 1948 shows well defined peaks at 20 s at 0605 UT and between 25 and 30 s over 0608-0609 UT. The
59
60

1 1949 middle panel shows the high time resolution SuperDARN data which were available only for
2
3
4 1950 parts of the analyzed interval due to the operational mode. The most important segment lies
5
6
7 1951 between 0608 and 0609 UT, and it is zoomed on in the bottom panel. During this segment, two
8
9
10 1952 oscillation cycles with periods of 13-14 s were also seen by the Ottawa magnetometers,
11
12
13 1953 although in magnetic records the main spectral peak was observed at 25-30 s. There is also
14
15
16 1954 evidence for wave activity in the other high-resolution intervals from Fig. 35.
17
18
19
20 1955

23 1956 **Pc3-4 and Pc5 Pulsations**

24
25
26 1957 The first mid-latitude observations of MHD waves were reported by Ponomarenko et al. (2003)
27
28
29 1958 using TIG. This work is generally a technical paper in which the authors describe and illustrate
30
31
32 1959 a way to visualize ULF wave signatures in the range-time maps of the Doppler velocity
33
34
35 1960 observed by SuperDARN radars. This visualization is achieved by applying median high-pass
36
37
38 1961 filtering and compressed dynamic range of the gray-scale color map (Fig. 36 from
39
40
41
42 1962 Ponomarenko et al. 2005). This analysis revealed the presence of the ULF signatures for 4-5
43
44
45 1963 hours per day. A very important finding was that 60% of the MHD waves were observed in the
46
47
48 1964 previously underused ground scatter component. Four different types of MHD waves were
49
50
51 1965 observed: (1) Low wavenumber Pc5 waves; (2) High wavenumber Pc5 waves; (3) Band-limited
52
53
54 1966 dayside Pc3-4 waves (thought to be generated via upstream waves); (4) Narrowband nighttime
55
56
57 1967 Pc4 waves (thought to be local FLRs). Importantly, the authors reported that 46% of the
58
59
60
61
62
63
64
65

1 1968 observed waves had no ground magnetic signature. The methodology presented in this paper
2
3
4 1969 was then used as the primary analysis method in 3 subsequent papers using mid-latitude
5
6
7 1970 SuperDARN radars, two of which look at Pc3-4 waves and one of which looks at Pc5 waves,
8
9
10 1971 which are discussed below.
11
12
13 1972
14
15
16 1973 Ponomarenko et al. (2005) investigated Pc3-4 waves in sea scatter from TIG. These data were
17
18
19
20 1974 complemented by ground magnetometer data from Macquarie Island. The waves were observed
21
22
23 1975 between 8 and 12 MLT and the authors concluded that the observed waves were driven by the
24
25
26 1976 interaction of upstream waves with the magnetosphere. Such waves are believed to be generated
27
28
29 1977 at the Earth's foreshock by the ion-cyclotron instability in reflected proton beams. These
30
31
32 1978 observations suggest that the Pc3/4 energy propagates into and through the magnetosphere in
33
34
35
36 1979 the isotropic fast mode and couples to field-line guided mode Alfvén waves at harmonics of the
37
38
39 1980 local resonant frequency. Furthermore, Ponomarenko et al. (2005) concluded that these waves
40
41
42 1981 were 3rd harmonic poloidal mode FLRs.
43
44
45 1982
46
47
48 1983 In a follow-on study, Ponomarenko et al. (2010) report a subsequent investigation of Pc3-4
49
50
51
52 1984 waves in ionospheric scatter from TIG together with ground magnetometer data, but here the
53
54
55 1985 emphasis of the paper is on waves observed on the nightside. The authors present synchronous
56
57
58 1986 variations of Pc3-4 spectra near the post-dawn cusp and the nightside plasmopause and
59
60
61
62
63
64
65

1 1987 plasmatrough with frequencies that closely match those of upstream waves. They present direct
 2
 3
 4 1988 evidence of a common source for the day and nightside Pc3-4 waves measured on the ground
 5
 6
 7 1989 and in the ionosphere. The observed nightside Pc3-4 oscillations show a pronounced
 8
 9
 10 1990 dependence on IMF parameters that replicates the behavior of simultaneous, dayside data. They
 11
 12
 13 1991 discuss a possible propagation scenario: (1) Upstream waves are generated at the Earth's
 14
 15
 16 1992 foreshock; (2) These interact with the magnetosphere to drive compressional waves that travel
 17
 18
 19 1993 throughout the magnetosphere; (3) These couple to field-aligned Alfvén waves that result in the
 20
 21
 22 1994 ionospheric and ground Pc3-4 signatures.
 23
 24
 25
 26 1995
 27
 28
 29 1996 In a statistical analysis, Norouzi-Sedeh et al. (2015) applied a manual event selection to over
 30
 31
 32 1997 300 days of high-resolution data obtained in 2007-2009 by TIG and UNW. The ULF wave
 33
 34
 35 1998 signatures in Doppler velocity oscillations over a relatively wide frequency range of ~0.5-50
 36
 37
 38 1999 mHz were identified by comparing the event time series and Fourier spectra with those obtained
 39
 40
 41 2000 from the underlying ground magnetometer data at Macquarie Island. This procedure identified
 42
 43
 44 2001 194 events, most of which were detected between 15-21 LT, which is consistent with the radar
 45
 46
 47 2002 echo occurrence (GS or IS) with a typical duration of ~1-1.5 hr. This peak in LT occurrence
 48
 49
 50 2003 matches a survey of radially polarized waves observed by the Active Magnetospheric Particle
 51
 52
 53 2004 Tracer Explorers Charge Composition Explorer (AMPTE CCE) spacecraft (Anderson et al.
 54
 55
 56 2005 1990). A maximum entropy analysis was then applied to estimate the spectral peak locations
 57
 58
 59
 60
 61
 62
 63
 64
 65

12006 with higher precision than can be provided by the Fast Fourier Transform (FFT) analysis. The
2
3
42007 maximum occurrence in frequency was observed at ~ 2 mHz with a secondary maximum located
5
6
72008 near 4-6 mHz, which matches the expected local FLR periods. Furthermore, Norouzi-Sedeh et
8
9
102009 al. (2015) suggested the presence of discrete spectral peaks at 1.3, 1.6, 2.1 and 2.8 mHz (Fig.
11
12
132010 37), although these values vary somewhat throughout the paper and, more importantly, the
14
15
162011 peaks' magnitudes seem to be close to the statistical variance level of the analysis. Similar
17
18
192012 discrete frequencies were also identified over 1830-2130 LT based exclusively on the ground
20
21
22
232013 magnetometer data, i.e. without pre-selection of the coincident radar-magnetometer events.
24
25
262014 While the majority of the oscillations (80%) showed little phase change with range, the rest
27
28
292015 showed zig-zag patterns which they identified as the ionospheric signatures of FLRs, and
30
31
322016 postulated that they may be associated with the predicted location of the plasmopause or
33
34
35
362017 ionospheric trough region. The observed L-values, however, are much higher than those
37
38
392018 predicted by models which leaves an open question on the nature of these waves.
40
41
422019
43
44
452020 In an event study of a large-scale global mode oscillation at ~ 1.6 mHz which was triggered by
46
47
482021 a Sudden Commencement (SC) and observed across a wide range of latitudes by ground
49
50
51
522022 magnetometers, Kawano et al. (2016) interpreted the initial oscillation as a global
53
54
552023 magnetospheric cavity mode through comparison with magnetometer data. The authors argued
56
57
582024 that only a global cavity mode can have a frequency of ~ 1 mHz in the plasmasphere, as the

12025 entire magnetospheric cavity radially oscillates at the same frequency. An interesting feature
2
3
42026 embedded within this interval is a wave which displays the amplitude and phase pattern
5
6
72027 characteristic of a FLR i.e., a single peak in amplitude at the resonant latitude accompanied by
8
9
102028 a monotonic change in phase across the latitudinal peak. This amplitude and phase pattern is
11
12
132029 revealed by a detailed spectral analysis of the high resolution (15 km in group range) ground /
14
15
162030 sea scatter signatures observed by HOK near $L = 2$ which demonstrate that, for a 15-min part
17
18
19
202031 of the one-hour wave event, a maximum in spectral power and steady increase of the phase with
21
22
232032 latitude have been observed. If these features are interpreted in terms of a poloidal FLR, as done
24
25
262033 by the authors, then the values of the plasma density at the equatorial plane required to produce
27
28
292034 the 1.6 mHz eigen oscillation would be an order of magnitude larger than those normally
30
31
322035 observed at these MLAT. Furthermore, the characteristic “kink” in the latitudinal phase
33
34
35
362036 progression is effectively absent from the data. In order to explain these discrepancies, the
37
38
392037 authors invoked (1) a quarter-wave type of FLR, (2) compression of the plasmasphere, (3)
40
41
422038 compression of the ionosphere and (4) enhanced ion outflow caused by the main phase of the
43
44
452039 magnetic storm, whose combined effect might have produced the observed oscillations.
46
47

482040
49

51 522041 **MHD Waves: Future Work**

53
54
552042 It is clear from the work that has been done on MHD waves with the mid-latitude SuperDARN
56
57
582043 radars that there is significant potential for further study. There are several future directions,
59
60

12044 both with existing data sets and radars, as well as potential new developments of radar
2
3
42045 technology, as well as links to current and future space missions. Two areas where the current
5
6
72046 data sets and radars could be used are identified before moving to new developments.
8
9
102047
11
12
132048 The work that has been currently done on Pi2 pulsations has yet to result in any firm consensus
14
15
162049 regarding the modes that are present at mid-latitudes. This situation perhaps is due to both the
17
18
19
202050 nature of the waves which are relatively short lived and occur during the nighttime when the
21
22
232051 presence of ground scatter is perhaps limited. Nevertheless, there are several directions which
24
25
262052 could be followed here, notably in developing statistical analyses which may enable us to
27
28
292053 separate out which modes are most often present. Further studies which relate ground and space
30
31
322054 observations, notably with space missions such as THEMIS, would also be helpful, in particular
33
34
35
362055 to determine the exact relationship between the wave signatures and tail dynamics as
37
38
392056 exemplified by BBFs. Finally, the use of interhemispheric studies may help in determining the
40
41
422057 wave modes present as this would place additional constraints on the models.
43
44
452058
46
47
482059 Moving to Pc3-4, these tend to be smaller scale waves and so are more localized. Consequently,
49
50
51
522060 it is to be expected that future studies would focus on small sub-sets of radars, making use of
53
54
552061 the interhemispheric capability that exists in the Japanese/Australian and the US/South
56
57
582062 American sectors. Furthermore, future work is required to determine the percentage of such
59
60
61
62
63
64
65

12063 waves which are related to wave energy directly penetrating from the solar wind compared with
2
3
42064 internal sources of them such as wave-particle interactions. Pc5 waves on the other hand are
5
6
72065 more likely to be larger scale oscillations such that more studies involving multiple radars,
8
9
102066 where possible, would be sensible, especially as the network at mid-latitudes continues to
11
12
132067 expand.
14
15
16
172068
18
19
202069 Finally, the development of new radar and analysis techniques is considered. It is clear from
21
22
232070 the paper by Greenwald et al. (2008) that higher time resolution observations will enable studies
24
25
262071 of higher frequency waves. Currently the SuperDARN technique is limited in two ways in this
27
28
292072 respect. One is the integration time along the beam and the other is the scanning from one beam
30
31
322073 to the next. Greenwald et al. (2008) demonstrated the potential of new ways of using the
33
34
35
362074 multipulse data to improve the time resolution along a beam and this potential has already been
37
38
392075 recognized within the community. Further, the potential afforded by imaging radars (for more
40
41
422076 detail see the “Technical Developments” subsection) for ULF wave studies cannot be
43
44
452077 underestimated. Finally, the development of analysis techniques which do not require a
46
47
482078 continuous data set, such as Lomb-Scargle spectral analysis (Lomb 1976; Scargle 1982), would
49
50
512079 benefit the analysis of SuperDARN, where often there are data gaps.
52
53
54
552080
56
57
58
59
60
61
62
63
64
65

12081 **Conclusions and Future Directions**

72083 **Conclusions and Science Directions**

102084 In this paper the scientific accomplishments of the mid-latitude component of SuperDARN
11
12
132085 have been reviewed in five specified areas, with some discussion of future science directions.
14

16
172086 Here is the brief summary:

18
19
202087 1) *Convection*. The expansion of SuperDARN to mid-latitudes has been a demonstrated success
21
22
232088 with previously unattainable measurements of the convection electric field equatorward of $\sim 60^\circ$
24
25
262089 MLAT now possible, and the ability to study a variety of phenomena occurring at mid-latitudes.
27
28
29
302090 In addition to the expected enhancement in the capability to monitor plasma circulation during
31
32
332091 geomagnetically active periods, the mid-latitude radars have significantly improved our
34
35
362092 understanding of SAPS by providing near-continuous measurements of their temporal and
37
38
392093 spatial variations, and their relationships with other measurements such as GPS TEC and both
40
41
422094 ground and space-based imagers. Future studies will undoubtedly reveal the statistical nature
43
44
452095 of SAPS occurrence and the origins of SAPS and SAID.

46
47
48
492096 2) *Ionospheric irregularities*. With the construction of the first purpose-built mid-latitude
50
51
522097 SuperDARN radars at WAL and HOK it is evident that additional types of irregularities exist
53
54
552098 at mid-latitudes. These include low-velocity irregularities in the sub-auroral region, high-
56
57
582099 velocity irregularities at the edge of the auroral oval associated with SAPS, and irregularities

12100 occurring during the passage of MSTIDs at temperate (lower) mid-latitudes. The relative
 2
 3
 42101 simplicity of the ionosphere at sub-auroral latitudes is a distinct advantage for relating the
 5
 6
 72102 irregularities to processes of plasma instability, and there has been impressive progress in the
 8
 9
 102103 modeling of irregularities in terms of the GDI, TGI, and coupling between the *E* and *F* regions.
 11
 12
 132104 There is a good reason to think that the mid-latitude radar observations are providing a critical
 14
 15
 162105 testbed of measurements for developing comprehensive first-principle models and that this
 17
 18
 192106 work will lead to fresh insights into ionospheric plasma physics of interest to a wide range of
 20
 21
 222107 researchers and operators by encompassing the generation and growth mechanisms of several
 23
 24
 252108 kinds of ionospheric irregularities and their relation to other phenomena (e.g., SAID / SAPS,
 26
 27
 282109 MSTIDs and *E* region shortenings due to enhanced conductivity) and to geophysical parameters
 29
 30
 312110 (e.g., latitude and geomagnetic activity).
 32
 33
 34
 352111 3) HF *propagation analysis*. HF propagation analysis can be utilized to conduct value-added
 36
 37
 382112 ionospheric research at mid-latitudes and as a tool for assessing radar performance. Looking
 39
 40
 412113 forward, two scientific topics that deserve further examination with propagation analysis are
 42
 43
 442114 solar cycle dependencies and interhemispheric differences. Also, it is feasible that calibrated
 45
 46
 472115 elevation angle data could be inverted to provide ionospheric plasma density suitable for
 48
 49
 502116 interhemispheric comparison.
 51
 52
 532117 4) *Ionosphere-neutral interactions*. The contributions of mid-latitude SuperDARN to the study
 54
 55
 562118 of phenomena associated with ion-neutral interactions have been predominantly through
 57
 58
 59
 60
 61
 62
 63
 64
 65

12119 observations of TIDs (large-scale and medium-scale). With mid-latitude SuperDARN it is
2
3
42120 possible to study the characteristics of TIDs in the sub-auroral and mid-latitude regions as a
5
6
72121 function of latitude, LT and geomagnetic activity; and several important characteristics have
8
9
102122 been clarified (e.g., the relationship to the intensity of the polar vortex). It has been
11
12
132123 demonstrated that the potential scope for study of ion-neutral coupling extends to the
14
15
162124 ionospheric disturbances that are due to big earthquakes, tsunamis, volcanic eruptions and
17
18
19
202125 tornadoes, and to the time scales of flywheel effects and disturbance dynamo effects.
21
22
232126 5) *MHD waves*. There has been a number of discoveries made using the mid-latitude
24
25
262127 SuperDARN radars to study MHD waves. Statistical studies have been limited to Pc3-5 waves
27
28
292128 and an important early finding was that 60% of MHD waves occurred in the ground scatter
30
31
322129 received by the radars (Ponomarenko et al. 2003), thus opening a new technique for analysis.
33
34
352130 Studies of nightside Pi2 pulsations have been mostly limited to case studies involving multiple
36
37
38
392131 data sets collected from the ground and from space. The first estimate of the rotation of the Pi2
40
41
422132 polarization ellipse was made with the results indicating that the conductivity profile is not as
43
44
452133 simple as originally modelled. In a serendipitous observation when testing a new coding scheme,
46
47
482134 Greenwald et al. (2008) made the first observations of Pi1 pulsations by a SuperDARN radar.
49
50
512135 Further studies of MHD waves using extended radar FOVs and new techniques are thus very
52
53
54
552136 promising.

582137

59
60
61
62
63
64
65

12138 **Satellite Conjunction**

2
3
42139 Mid-latitude SuperDARN radars have FOVs which cover sub-auroral and auroral latitudes and
5
6
72140 are connected by magnetic field lines to the inner magnetosphere and near-earth plasma sheet.
8
9
102141 Comparison between SuperDARN and satellite observations is crucial for understanding the
11
12
132142 dynamics of the coupled (inner) magnetosphere and ionosphere. Collaborative studies with, for
14
15
162143 example, the THEMIS (Angelopoulos 2008) and the Van Allen Probes satellites (Mauk et al.
17
18
192144 2013) have already proven to be capable of addressing important science themes such as linkage
20
21
22
232145 of dynamical aurora in the ionosphere and plasma evolution in the magnetosphere (e.g.,
24
25
262146 Nishimura et al. 2010) and ULF waves (e.g., Teramoto et al. 2016; Kim et al. 2017), and so
27
28
292147 forth. Recently the Exploration of energization and Radiation in Geospace (ERG) satellite (also
30
31
322148 known as “Arase” satellite) (Miyoshi et al. 2012) has joined such a collaboration framework
33
34
352149 particularly for studies of the inner magnetosphere, after its successful launch at the end of 2016.
36
37
38
392150 The addition of ERG to the inner magnetospheric satellite fleet enables the global view of
40
41
422151 ionospheric convection obtained instantaneously by SuperDARN to be compared with
43
44
452152 simultaneous observations at multiple points in the magnetosphere. Multi-spacecraft
46
47
482153 conjunction studies with SuperDARN could be used to monitor the longitude/MLT evolution
49
50
512154 of magnetosphere-ionosphere coupled processes in an instantaneous manner. Several such
52
53
54
552155 studies are expected in the near future. Finally, there are several forthcoming spacecraft
56
57
582156 missions related to mid-latitude SuperDARN, such as Solar-wind Magnetosphere Ionosphere
59
60
61
62
63
64
65

12157 Link Explorer (SMILE), Ionospheric Connection Explorer (ICON), Global-scale Observations
2
3
42158 of the Limb and Disk (GOLD), Demonstration and Science Experiments (DSX) and Tool for
5
6
72159 the Analysis of RAdiations from lightNings and Sprites (TARANIS), as well as ongoing
8
9
102160 missions such as Magnetospheric Multiscale Mission (MMS).

132161

16 172162 **Expansion of SuperDARN Coverage**

18
19
202163 There are several plans to expand the reach of mid-latitude SuperDARN in both longitude and
21
22
232164 latitude. Some examples are the radars planned for several places in Europe. Construction of an
24
25
262165 HF radar at Jiamusi, China has recently been completed while construction of an additional
27
28
292166 radar at Kunming in southern China is proceeding. There are also possibilities for the Russian
30
31
322167 SuperDARN-type radars to join the SuperDARN network in the future. Finally, there are plans
33
34
35
362168 to build a SuperDARN radar in the low-latitude and equatorial regions (possible candidates are
37
38
392169 southern Japan, South-East Asia, Pacific Ocean etc.) to study the horizontal structure of the
40
41
422170 ionospheric convection and irregularities associated with equatorial plasma bubbles over
43
44
452171 distances of several thousand kilometers.

482172

51 522173 **Interhemispheric Conjugacy**

53
54
552174 Interhemispheric study of a variety of ionospheric phenomena such as SAPS is important for
56
57
582175 developing improved understanding of processes in the magnetosphere, and the connection

12176 between the magnetosphere and ionosphere. Conjugacy studies are also important for the study
2
3
42177 of ion-neutral coupling processes, e.g., to identify the dependence of TIDs on local time,
5
6
72178 geomagnetic / geographic latitude and season. The present sets of radars which could be used
8
9
102179 for such studies are (i) BKS (North America) and FIR (South America). (ii) HOK and HKW
11
12
132180 (Asia) and TIG, UNW and BKP (Oceania).
14
15

16
172181

18 19 202182 **Technical Developments**

21
22
232183 There are several prospects for further technical development in terms of 1) hardware, 2)
24
25
262184 software and 3) algorithms.

27
28
292185 1) *Hardware*. The BKP, which started operation in 2014, is the first fully digital SuperDARN
30
31
322186 radar and is much more sensitive than the pre-existing radars and much less susceptible to
33
34
35
362187 instrumental noise. The same digital radar system developed for BKP is now also running at
37
38
392188 the FIR site. Similarly, the University of Alaska, Fairbanks group has developed an ‘imaging’
40
41
422189 capability for the SuperDARN radar at KOD (Parris and Bristow 2009). Likewise, University
43
44
452190 of Saskatchewan engineers are currently working on designing a digital ‘imaging’ radar which
46
47
482191 would replace consecutive sampling of the radar beams by simultaneous multi-directional
49
50
51
522192 measurements. This ‘imaging’ will be achieved through illuminating the whole radar’s FOV by
53
54
552193 widening the main antenna lobe during transmission and recording raw data at each antenna so
56
57
582194 that the beam forming and data analysis are performed afterwards in software. This approach

12195 would decrease the sampling rate for the circulation maps from 1-2 min to several seconds
2
3
42196 and/or significantly improve the accuracy in estimating the echo parameters by increasing the
5
6
72197 ACF integration time. The “imaging” radar would also provide a continuous azimuthal
8
9
102198 coverage for studying ULF waves with periods smaller than 2 min (Pc4 and higher frequencies),
11
12
132199 which currently can only be studied using 2-3 beams in order to achieve a required sampling
14
15
162200 rate. Yet another advantage will be the ability to simultaneously sound at multiple frequencies
17
18
19
202201 (real “stereo” mode).
21
22
232202
24
25
262203 2) *Software*. The SuperDARN Data Analysis working group periodically releases updated
27
28
292204 versions of the Radar Software Toolkit (RST). The most recent version is RST 4.2
30
31
322205 (SuperDARN Data Analysis Working Group 2018). The major recent improvements are: a)
33
34
352206 Full revision of the ACF fitting package. b) Utilization of the latest statistical models (Cousins
36
37
38
392207 and Shepherd 2010; Thomas and Shepherd 2018) using multiple radar data in both hemispheres
40
41
422208 and the inclusion of data from polar and mid-latitudes versus the previous model (Ruohoniemi
43
44
452209 and Greenwald 1996) based on only one radar (GBR). c) The Chisham virtual height model
46
47
482210 (Chisham et al. 2008) was added as option in addition to the original standard SuperDARN
49
50
51
522211 virtual height model, traditionally used to map radar data.
53
54
552212
56
57
582213 3) *Algorithm*. A task force, led by Aurélie Marchaudon, has been formed to determine a reliable
59
60
61
62
63
64
65

12214 way of calibrating interferometry (elevation angle) data, including techniques utilizing low-
2
3
42215 elevation ground scatter (Ponomarenko et al. 2015), near-range (“meteor”) echoes (Chisham
5
6
72216 and Freeman 2013) and artificial irregularities generated by powerful radio waves (ionospheric
8
9
102217 “heating”) (Burrell et al. 2016).

132218

172219 **Cooperation with Modeling Activities**

19
202220 Cooperation with theoretical modeling and numerical simulation activities is important for
21
22
232221 understanding the magnetosphere-ionosphere-thermosphere coupled system. This is especially
24
25
262222 true for the mid-latitude SuperDARN observations because during magnetic storms the
27
28
292223 contribution from the ring current becomes dominant (internal forcing), and the convection
30
31
322224 dynamics cannot be interpreted only in terms of the expansion of the high-latitude convection.
33
34
35
362225 As already discussed in the “Convection” Section, Fig. 14 shows one example of the
37
38
392226 coordinated study, a comparison between the SuperDARN HOK observations of SAPS
40
41
422227 structure indicating temporal changes (top panel) with simulation results from the CRCM under
43
44
452228 various boundary conditions (Ebihara et al. 2009). These results clearly indicate the importance
46
47
482229 of ring current dynamics in controlling the SAPS spatial structure. Additional model-data
49
50
51
522230 comparisons of this sort are needed to make further progress understanding the coupled
53
54
552231 dynamics of the inner magnetosphere and sub-auroral ionosphere. Finally, efforts to use
56
57
582232 SuperDARN data to constrain first-principle models of ionosphere, such as the Research

12233 Institute in Astrophysics and Planetology (IRAP) Plasmasphere-Ionosphere model (IPIM)
2
3
42234 (Marchaudon and Blelly 2015), are currently in progress and will lead to consistent retrieval of
5
6
72235 ionospheric parameters over large 3D coverage regions.
8
9

102236

11

12

13

142237

National Strategy

172238 Funding of each mid-latitude SuperDARN radar is closely related to the national strategy of the
18
19
202239 participant country.
21

22

232240

24

25

262241 In the United States, the most recent “Decadal Survey” report commissioned by the National
27

28

292242 Research Council identified four scientific goals for the space physics research community over
30

31

322243 the next ten years. SuperDARN radars at mid-latitudes are particularly relevant to the second
33

34

352244 goal: to determine the dynamics and coupling of Earth's magnetosphere, ionosphere, and
36

37

382245 atmosphere and their response to solar and terrestrial inputs. To meet these goals, the report
39

40

412246 recommends the creation of a new, integrated multiagency initiative – DRIVE – that will more
42

43

442247 effectively exploit NASA and NSF scientific assets to address the pressing needs for improved
45

46

472248 space weather specification and forecasts. The five directives comprising the DRIVE initiative
48

49

502249 are: (1) Diversify observing platforms with microsatellites and mid-scale ground-based assets;
51

52

532250 (2) Realize scientific potential by sufficiently funding operations and data analysis; (3) Integrate
54

55

562251 observing platforms and strengthen ties between agency disciplines; (4) Venture forward with
57

58

59

60

61

62

63

64

12252 science centers and instrument and technology development; and (5) Educate, empower, and
2
3
42253 inspire the next generation of space researchers. Much of the success of SuperDARN, to date,
5
6
72254 can be attributed to the fact that it was founded on the very same collaborative principles that
8
9
102255 underpin these five directives and, as such, it is uniquely positioned to play a key role in the
11
12
132256 development of the DRIVE initiative as it moves forward.
14

15
16
172257
18
19
202258 In Japan, the government has selected master plan projects and drawn up a roadmap of scientific
21
22
232259 research every few years, in order to identify future science directions. The project “Study of
24
25
262260 Coupling Processes in the Solar-Terrestrial System” was approved as a project of “Masterplan
27
28
292261 2014” and “Masterplan 2017” by the Science Council of Japan, and of “Roadmap 2014” (one
30
31
322262 of 11 new approved projects) by the Ministry of Education, Culture, Sports, Science and
33
34
352263 Technology (MEXT). SuperDARN is related to this project in that it studies the coupling
36
37
38
392264 processes in the solar-terrestrial environment using several kinds of observation techniques,
40
41
422265 including HF radar network (Tsuda et al. 2016).
43
44

452266
46
47
482267 The UK government has identified severe space weather as a potential risk and has included
49
50
51
522268 this topic in its National Risk Register of Civil Emergencies (see
53
54
552269 <https://www.gov.uk/government/publications/national-risk-register-of-civil-emergencies-2017-edition>).
56

57
582270 SuperDARN is contributing to both the science and understanding of space weather and could
59
60

12271 in the future potentially contribute to operational systems. SuperDARN is also seen as a major
2
3
42272 contribution to national capability providing long-term and large-scale monitoring of the
5
6
72273 atmosphere through its Antarctic SuperDARN program. Finally, the UK is a major contributor
8
9
102274 to the joint European Space Agency (ESA) and Chinese National Space Science Centre (NSSC)
11
12
132275 space mission SMILE which is scheduled for launch in 2021 and SuperDARN is seen as a
14
15
162276 major ground-based contributor to that program. Other participating countries also have their
17
18
192277 national strategy for the future of space science, and some of them are related to the mid-latitude
20
21
22
232278 SuperDARN.

262279

292280 **Training and Public Outreach**

322281 Construction and operation of mid-latitude SuperDARN radars is important not only for
33
34
352282 obtaining new scientific results, but also for attracting young students and training technical
36
37
38
392283 staff. Through the training activity, they can learn the engineering details of the radar system,
40
41
422284 characteristics of irregularities and HF wave propagation, and also the science of
43
44
452285 magnetosphere / ionosphere / upper atmosphere dynamics. Radars located where access is
46
47
482286 relatively easy provide ideal opportunities for hands-on engineering engagement. One example
49
50
51
522287 is that HOK and HKW in Japan has been used for training members of Japanese Antarctic
53
54
552288 Research Expedition (JARE) every year. Through the training activity, they can learn the
56
57
582289 engineering details of the radar system in advance. However, even for those radars located in

12290 remote locations, the routine data analysis / processing and software development activities
2
3
42291 provide excellent opportunities for education and training.
5
6
72292
8
9
102293 For the continued operation and maintenance of the mid-latitude SuperDARN radars, it is
11
12
132294 crucial that relevant government agencies and the general public understand the value they
14
15
162295 provide for basic research and space weather applications (e.g., Jansen and Pirjola 2004). It is
17
18
192296 also important that researchers in other fields outside space science understand SuperDARN.
20
21
222297 For this purpose, public releases of radar operations and new scientific findings in the most
23
24
25
262298 effective ways are necessary (Wild 2012).
27
28
292299
30
31
32
33
34
35
36
37
38
39
40
41
42
43
44
45
46
47
48
49
50
51
52
53
54
55
56
57
58
59
60
61
62
63
64
65

12300 **Declarations**

2
32301
4
5
62302 **Availability of data and materials**

7
8
92303 The SuperDARN datasets shown in this paper are available in the Virginia Tech website at:

10
11
122304 <http://vt.superdarn.org> .

13
14
152305 The AACGM-v2 software for calculating geomagnetic coordinates of the SuperDARN radars is

16
17
182306 available in the Dartmouth College web server at:

19
20
212307 <http://superdarn.thayer.dartmouth.edu/aacgm.html> .

22
23
242308
25
262309 **Competing interests**

27
28
292310 The authors declare that they have no competing interest.

30
31
322311
33
34
35
362312 **Funding**

37
38
392313 SuperDARN is a collection of radars funded by national scientific funding agencies of Australia,

40
41
422314 Canada, China, France, Italy, Japan, Norway, South Africa, United Kingdom and the United

43
44
452315 States of America. Organization of the workshops for writing up the present review paper was

46
47
482316 supported by Japan Society for the Promotion of Science (JSPS) (Grant-in-Aid for Specially

49
50
51
522317 Promoted Research): Study of dynamical variation of particles and waves in the inner

53
54
552318 magnetosphere using ground-based network observations (PWING), Project Number:

56
57
582319 16H06286. Completion of the present review paper was partly supported by JSPS (Grand-in-

12320 Aid for Scientific Research), Project Number: 18KK0099. Part of the work of TH was done at
2
3
42321 the ERG-Science Center operated by ISAS/JAXA and Institute for Space-Earth Environmental
5
6
72322 Research (ISEE) /Nagoya University.
8
9

102323

11

12

13

142324

Authors' contributions

15

16

172325

NN, JMR and ML originally proposed the present review paper, attended the workshops in

18

19

202326

Nagoya, Japan and contributed to the writing of the paper. JBHB, AVK, SGS and GC attended

21

22

232327

the workshop(s) and contributed to the writing of the paper as section heads. TH, EGT, RAM,

24

25

262328

AM, PP, and JW attended the workshop(s) and contributed to the writing of the paper. SEM,

27

28

292329

WAB, JD and EM contributed to the content of the paper as mid-latitude SuperDARN Principal

30

31

32

332330

Investigators and Co-Investigators. RAG, TA and TK contributed to the content of the paper as

34

35

362331

the authors of the references cited in the present paper and by commenting on the manuscript.

37

38

392332

All authors read and approved the final manuscript.

40

41

422333

43

44

452334

Acknowledgements

46

47

482335

This review paper originated from approximately one-week long workshops in January 2017

49

50

51

522336

and January 2018, during which we discussed the content of the paper, its structure and future

53

54

552337

directions of the mid-latitude SuperDARN network. These workshops were carried out by the

56

57

582338

joint research program of the Institute for Space-Earth Environmental Research, Nagoya

59

60

61

62

63

64

65

12339 University, and supported by funding agencies described in the ‘funding’ section. Finally, we

2

3

42340 would like to thank everyone who contributed to the completion of the review paper.

5

6

72341

8

9

102342

11

12

13

14

15

16

17

18

19

20

21

22

23

24

25

26

27

28

29

30

31

32

33

34

35

36

37

38

39

40

41

42

43

44

45

46

47

48

49

50

51

52

53

54

55

56

57

58

59

60

61

62

63

64

65

Abbreviations

AACGM: Altitude Adjusted Corrected Geomagnetic; ACF: Autocorrelation Function; AGW: Acoustic-Gravity Wave; AMPTE CCE: Active Magnetospheric Particle Tracer Explorers Charge Composition Explorer; AWFC: Auroral Westward Flow Channel; BBFs: Bursty Bulk Flows; BCOV: Beaver Cove; CME: Coronal Mass Ejection; CRCM: Comprehensive Ring Current Model; DSX: Demonstration and Science Experiments; DUSE: Dusk Scatter Event; EKB: Ekaterinburg; EPB: Electron Precipitation Boundary; ERG: Exploration of energization and Radiation in Geospace; ESA: European Space Agency; FAC: Field-Aligned Current; FFT: Fast Fourier Transform; FLR: Field Line Resonance; FOV: Field Of View; FPI: Fabry-Perot Interferometer; FTEs: Flux-Transfer Events; GDI: Gradient Drift Instability; GEONET: GPS Earth Observation Network System; GNSS: Global Navigation Satellite System; GOLD: Global-scale Observations of the Limb and Disk; GPS: Global positioning system; GS: Ground Scatter; HAIR: High-Aspect Angle irregularity Region; HF: High Frequency; HOP: Hokkaido Pair of; HWM: Horizontal Wind Model; ICON: Ionospheric Connection Explorer; IGRF: International Geomagnetic Reference Field; IMAGE: International Monitor for Auroral Geomagnetic Effects; IMF: Interplanetary Magnetic Field; IRAP: Research Institute in Astrophysics and Planetology; IRI: International Reference Ionosphere; IS: Ionospheric Scatter; ISEE: Institute for Space-Earth Environmental Research; ISR: Incoherent Scatter Radar; JARE: Japanese Antarctic Research Expedition; JSPS: Japan Society for the Promotion

12362 of Science; KHI: Kelvin-Helmholtz Instability; LANL: Los Alamos National Laboratory; LEO:
2
3
42363 Low Earth Orbit; LOS: Line-Of-Sight; LSTID: Large-Scale Traveling Ionospheric
5
6
72364 Disturbance; LT: Local Time; MEXT: Ministry of Education, Culture, Sports, Science and
8
9
102365 Technology; MHD: Magnetohydrodynamic; MF: Medium Frequency; MI: Magnetosphere-
11
12
132366 Ionosphere; MLAT: Geomagnetic Latitude; MLT: Magnetic Local Time; MMS:
14
15
162367 Magnetospheric Multiscale Mission; MSEs: Mesosphere Summer Echoes; MSI: Mid-Sized
17
18
192368 Infra-structure; MSTID: Medium-Scale Traveling Ionospheric Disturbance; MU: Middle and
20
21
222369 Upper atmosphere; MUF: Maximum Usable Frequency; NASA: National Aeronautics and
23
24
25
262370 Space Administration; NSF: National Science Foundation; NSSC: National Space Science
27
28
292371 Centre; OTH: Over The Horizon; PBIs: Poleward Boundary Intensifications; PCR:
30
31
322372 Plasmaspheric Cavity Resonance; PI: Principal Investigator; PIC: Particle-In-Cell; PJ:
33
34
35
362373 Polarization Jet; PMSE: Polar Mesosphere Summer Echoes; PPEF: Prompt Penetration Electric
37
38
392374 Field; PVR: Plasmaspheric Virtual Resonance; PWING: Study of dynamical variation of
40
41
422375 Particles and Waves in the INner magnetosphere using Ground-based network observations
43
44
452376 RST: Radar Software Toolkit; SAEF: Sub-Auroral Electric Field; SAIDs: Sub-Auroral Ion
46
47
482377 Drifts; SAIS: Sub-Auroral Ionospheric Scatter; SAPS: Sub-Auroral Polarization Streams;
49
50
51
522378 SAPSWS: SAPS Wave Structure; SARAS: Substorm-Associated Radar Auroral Surges; SC:
53
54
552379 Sudden Commencement; SCW: Substorm Current Wedge; SED: Storm Enhanced Density; SI:
56
57
582380 Sudden Impulse; SMILE: Solar-wind Magnetosphere Ionosphere Link Explorer; SSC: Storm
59
60
61
62
63
64
65

12381 Sudden Commencement; SuperDARN: Super Dual Auroral Radar Network; TARANIS: Tool
2
3
42382 for the Analysis of RADIations from lightNIngs and Sprites; TCVs: Traveling Convection
5
6
72383 Vortices; TEC: Total Electron Content; TECU: TEC Unit; TGI: Temperature Gradient
8
9
102384 Instability; THEMIS: Time History of Events and Macroscale Interactions during Substorms;
11
12
132385 TIDs: Traveling Ionospheric Disturbances; TIGER: Tasman International Geospace
14
15
162386 Environment Radar; TOI: Tongue Of Ionization; TTFD: Twin Terminated folded Dipole; ULF:
17
18
192387 Ultra-Low Frequency; UT: Universal Time; VHF: Very High Frequency; WSA: Weddell Sea
20
21
22
232388 Anomaly;
24
25
262389
27
28
292390
30
31
32
33
34
35
36
37
38
39
40
41
42
43
44
45
46
47
48
49
50
51
52
53
54
55
56
57
58
59
60
61
62
63
64
65

[Click here to view linked References](#)

1
2
3
4
5
6
7
8
9
10
11
12
13
14
15
16
17
18
19
20
21
22
23
24
25
26
27
28
29
30
31
32
33
34
35
36
37
38
39
40
41
42
43
44
45
46
47
48
49
50
51
52
53
54
55
56
57
58
59
60
61
62
63
64
65

References

- 2391
- 2392
- 2393 Afraimovich EL, Edemskiy IK, Leonovich AS, Leonovich LA, Voeykov SV, Yasyukevich YV
(2009) MHD nature of night-time MSTIDs excited by the solar terminator. *Geophys Res Lett*
36:L15106. doi:10.1029/2009GL039803
- 2396
- 2397 Anderson BJ, Engebretson MJ, Rounds SP, Zanetti LJ, Potemra TA (1990) A statistical study of
Pc 3–5 pulsations observed by the AMPTE/CCE Magnetic Fields Experiment, 1. Occurrence
distributions. *J Geophys Res* 95:10495. doi:10.1029/JA095iA07p10495
- 2400
- 2401 Anderson PC, Heelis RA, Hanson WB (1991) The ionospheric signatures of rapid subauroral ion
drifts. *J Geophys Res* 96(A4):5785–5792. doi:10.1029/90JA02651
- 2403
- 2404 Anderson PC, Hanson WB, Heelis RA, Craven JD, Baker DN, Frank LA (1993) A proposed
production model of rapid subauroral ion drifts and their relationship to substorm evolution. *J*
Geophys Res 98(A4):6069–6078. doi:10.1029/92JA01975
- 2407
- 2408 Anderson PC, Carpenter DL, Tsuruda K, Mukai T, Rich FJ (2001) Multisatellite observations of
rapid subauroral ion drifts (SAID). *J Geophys Res* 106(A12):29585–29599.
doi:10.1029/2001JA000128
- 2411
- 2412 Angelopoulos V (2008) The THEMIS Mission. *Space Sci Rev* 141:5–34. doi:10.1007/s11214-
008-9336-1

1
2
3
4 2414
5
6
7 2415 Araki T (1977) Global structure of geomagnetic sudden commencements. Planet Space Sci 25:
8
9 2416 373–384. doi:10.1016/0032-0633(77)90053-8
10
11
12 2417
13
14 2418 Araki T, Fujitani S, Emoto M, Yumoto K, Shiokawa K, Ichinose T, Luehr H, Orr D, Milling DK,
15
16 2419 Singer H, Rostoker G, Tsunomura S, Yamada Y, Liu CF (1997) Anomalous sudden
17
18 commencement on March 24, 1991. J Geophys Res 102:14075-14086. doi:10.1029/96JA03637
19 2420
20
21 2421
22
23
24 2422 Baker KB, Wing S (1989) A new magnetic coordinate system for conjugate studies at high
25
26 2423 latitudes. J Geophys Res 94(A7):9139–9143. doi:10.1029/JA094iA07p09139
27
28
29 2424
30
31 2425 Baker JBH, Greenwald RA, Ruohoniemi JM, Oksavik K, Gjerloev JW, Paxton LJ, Hairston MR
32
33 2426 (2007) Observations of ionospheric convection from the Wallops SuperDARN radar at middle
34
35 latitudes. J Geophys Res 112:A01303. doi:10.1029/2006JA011982
36 2427
37
38 2428
39
40
41 2429 Barraclough DR (1987) International geomagnetic reference field: the fourth generation. Phys.
42
43 2430 Earth Planet. Interiors 48:279-292
44
45
46 2431
47
48 2432 Bender LC, Leslie LM (1994) Evaluation of a Third Generation Ocean Wave Model for the
49
50 Australian Region. BMRC Research Report No 43 Australian Bureau of Meteorology
51 2433
52
53 2434
54
55 2435 Bergardt OI, Perevalova NP, Dobrynina AA, Kutelev KA, Shestakov NV, Bakhtiarov VF,
56
57 Kusonsky OA, Zagretdinov RV, Zherebtsov GA (2015) Toward the azimuthal characteristics of
58 2436
59
60
61
62
63
64
65

1
2
3
4 2437 ionospheric and seismic effects of “Chelyabinsk” meteorite fall according to the data from
5
6
7 2438 coherent radar, GPS, and seismic networks. *J Geophys Res Space Physics* 120:10754–10771.
8
9 2439 doi:10.1002/2015JA021549
10
11 2440
12
13
14 2441 Berngardt OI, Ruohoniemi JM, Nishitani N, Shepherd SG, Bristow WA, Miller ES (2018)
15
16 2442 Attenuation of decameter wavelength sky noise during x-ray solar flares in 2013-2017 based on
17
18
19 2443 the observations of midlatitude radars. *J Atmos Sol Terr Phys* 173:1-13.
20
21 2444 <https://doi.org/10.1016/j.jastp.2018.03.022>
22
23
24 2445
25
26
27 2446 Bilitza D, Altadill D, Zhang Y, Mertens C, Truhlik V, Richards P, McKinnell LA, Reinisch B
28
29 2447 (2014) The International Reference Ionosphere 2012 – a model of international collaboration. *J*
30
31
32 2448 *Space Weather Space Clim* 4 A07. doi:10.1051/swsc/2014004
33
34
35 2449
36
37 2450 Blanc M, Richmond A (1980) The ionospheric disturbance dynamo. *J Geophys Res* 85(A4): 1669–
38
39
40 2451 1686. doi:10.1029/JA085iA04p01669
41
42 2452
43
44
45 2453 Blanchard GT, Sundeen S, Baker KB (2009) Probabilistic identification of high - frequency radar
46
47 2454 backscatter from the ground and ionosphere based on spectral characteristics. *Radio Sci* 44
48
49
50 2455 RS5012. doi:10.1029/2009RS004141
51
52 2456
53
54
55 2457 Bland EC, McDonald AJ, de Larquier S, Devlin JC (2014) Determination of ionospheric
56
57 2458 parameters in real time using SuperDARN HF radars. *J Geophys Res Space Physics* 119:5830–
58
59 2459 5846. doi:10.1002/2014JA020076
60
61
62
63
64
65

1
2
3
4 2460
5
6
7 2461 Boudouridis A, Lyons LR, Zesta E, Ruohoniemi JM (2007) Dayside reconnection enhancement
8
9 2462 resulting from a solar wind dynamic pressure increase. J Geophys Res 112:A06201.
10
11
12 2463 doi:10.1029/2006JA012141
13
14 2464
15
16 2465 Boudouridis A Lyons LR, Zesta E, Weygand JM, Ribeiro AJ, Ruohoniemi JM (2011) Statistical
17
18
19 2466 study of the effect of solar wind dynamic pressure fronts on the dayside and nightside ionospheric
20
21 2467 convection. J Geophys Res 116:A10233. doi:10.1029/2011JA016582
22
23
24 2468
25
26 2469 Bristow WA, Greenwald RA, Villain JP (1996) On the seasonal dependence of medium-scale
27
28
29 2470 atmospheric gravity waves in the upper atmosphere at high latitudes. J Geophys Res 101(A7):
30
31 2471 15685–15699. doi:10.1029/96JA01010
32
33
34 2472
35
36 2473 Burrell, AG, Yeoman TK, Milan SE, and Lester M (2016) Phase calibration of interferometer
37
38 2474 arrays at high-frequency radars. Radio Sci 51: 1445–1456. doi:10.1002/2016RS006089
39
40
41 2475
42
43 2476 Carbary JF (2005) A Kp-based model of auroral boundaries. Space Weather 3(10):20001.
44
45 2477 <http://doi.org/10.1029/2005SW000162>
46
47
48 2478
49
50 2479 Carter BA, Makarevich RA (2009) E region decameter-scale plasma waves observed by the dual
51
52
53 2480 TIGER HF radars. Ann Geophys 27:261-278
54
55 2481
56
57 2482 Carter BA, Makarevich RA (2010) On the diurnal variation of the E-region coherent HF echo
58
59
60 2483 occurrence. J Atmos Solar Terr Phys 72:570-582
61
62
63
64
65

1
2
3
4 2484
5
6
7 2485 Chakraborty S, Ruohoniemi JM, Baker JBH, Nishitani, N (2018) Characterization of short-wave
8
9 2486 fadeout seen in daytime SuperDARN ground scatter observations. Radio Sci 53(4):472-484.
10
11
12 2487 <https://doi.org/10.1002/2017RS006488>
13
14 2488
15
16 2489 Chisham G, Orr D, Yeoman TK (1992) Observations of a giant pulsation across an extended array
17
18
19 2490 of ground magnetometers and on auroral radar. Planet Space Sci 40:953-964. doi:10.1016/0032-
20
21 2491 0633(92)90135-B
22
23
24 2492
25
26 2493 Chisham G, Pinnock M, Rodger AS, Villain J-P (2000) High-time resolution conjugate
27
28
29 2494 SuperDARN radar observations of the dayside convection response to changes in IMF By. Ann
30
31 2495 Geophys 18:191-201
32
33
34 2496
35
36 2497 Chisham G, Lester M, Milan SE, Freeman MP, Bristow WA, Grocott A, McWilliams KA,
37
38 2498 Ruohoniemi JM, Yeoman TK, Dyson PL, Greenwald RA, Kikuchi T, Pinnock M, Rash JPS, Sato
39
40
41 2499 N, Sofko GJ, Villain J-P, and Walker ADM (2007) A decade of the Super Dual Auroral Radar
42
43 2500 Network (SuperDARN): scientific achievements, new techniques and future directions. Surv.
44
45
46 2501 Geophys. 28: 33 <https://doi.org/10.1007/s10712-007-9017-8>
47
48 2502
49
50
51 2503 Chisham G, Yeoman TK, and Sofko GJ (2008) Mapping ionospheric backscatter measured by the
52
53 2504 SuperDARN HF radars – Part 1: A new empirical virtual height model. Ann. Geophys. 26:823-
54
55
56 2505 841
57
58 2506
59
60
61
62
63
64
65

1
2
3
4 2507 Chisham G, Freeman MP (2013) A reassessment of SuperDARN meteor echoes from the upper
5
6
7 2508 mesosphere and lower thermosphere. *J Atmos Sol Terr Phys* 102: 207-221.
8
9 2509 <https://doi.org/10.1016/j.jastp.2013.05.018>
10
11 2510
12
13
14 2511 Clausen LBN, Ruohoniemi JM, Greenwald RA, Thomas EG, Shepherd SG, Talaat ER, Bristow
15
16 2512 WA, Zheng Y, Coster AJ, Sazykin S (2012) Large-scale observations of a subauroral polarization
17
18
19 2513 stream by midlatitude SuperDARN radars: Instantaneous longitudinal velocity variations. *J*
20
21 2514 *Geophys Res* 117: A05306. doi:10.1029/2011JA017232
22
23
24 2515
25
26 2516 Coco I, Amata E, Marcucci MF, Ambrosino D, Villain J-P, Haniuise C (2008) The effects of an
27
28
29 2517 interplanetary shock on the high - latitude ionospheric convection during an IMF By - dominated
30
31
32 2518 period. *Ann Geophys* 26:2937–2951
33
34
35 2519
36
37 2520 Cousins EDP, Shepherd SG (2010) A dynamical model of high-latitude convection derived from
38
39 2521 SuperDARN plasma drift measurements. *J Geophys Res* 115:A12329.
40
41
42 2522 doi:10.1029/2010JA016017
43
44 2523
45
46
47 2524 Crowley G, Rodrigues FS (2012) Characteristics of traveling ionospheric disturbances observed
48
49 2525 by the TIDDBIT sounder. *Radio Sci* 47:RS0L22. doi:10.1029/2011RS004959
50
51
52 2526
53
54 2527 Currie JL, Waters CL, Menk FW, Sciffer MD, Bristow WA (2016) SuperDARN backscatter
55
56 2528 during intense geomagnetic storms. *Radio Sci* 51:814–825. doi:10.1002/2016RS005960
57
58
59 2529
60
61
62
63
64
65

1
2
3
4 2530 de Larquier S, Ruohoniemi JM, Baker JBH, Ravindran-Varrier N, Lester M (2011) First
5
6 2531 observations of the midlatitude evening anomaly using Super Dual Auroral Radar Network
7
8
9 2532 (SuperDARN) radars. *J Geophys Res* 116:A10321. doi:10.1029/2011JA016787
10
11 2533
12
13
14 2534 de Larquier S, Ponomarenko P, Ribeiro AJ, Ruohoniemi JM, Baker JBH, Sterne KT, Lester M
15
16 2535 (2013) On the spatial distribution of decameter-scale subauroral ionospheric irregularities
17
18 2536 observed by SuperDARN radars. *J Geophys Res Space Physics* 118:5244–5254.
19
20
21 2537 doi:10.1002/jgra.50475
22
23
24 2538
25
26 2539 de Larquier S, Eltrass A, Mahmoudian A, Ruohoniemi JM, Baker JBH, Scales WA, Erickson PJ,
27
28
29 2540 Greenwald RA (2014). Investigation of the temperature gradient instability as the source of
30
31 2541 midlatitude quiet time decameter-scale ionospheric irregularities:1.Observations. *J Geophys Res*
32
33 2542 *Space Physics* 119:4872–4881. doi:10.1002/2013JA019644
34
35
36 2543
37
38 2544 Ding F, Wan W, Liu L, Afraimovich EL, Voeykov SV, Perevalova NP (2008) A statistical study
39
40
41 2545 of large-scale traveling ionospheric disturbances observed by GPS TEC during major magnetic
42
43 2546 storms over the years 2003–2005. *J Geophys Res* 113:A00A01. doi:10.1029/2008JA013037
44
45
46 2547
47
48 2548 Ding F, Wan W, Xu G, Yu T, Yang G, Wang J (2011) Climatology of medium - scale traveling
49
50
51 2549 ionospheric disturbances observed by a GPS network in central China. *J Geophys Res*
52
53 2550 116:A09327. doi:10.1029/2011JA016545
54
55
56 2551

1
2
3
4 2552 Drob DP, Emmert JT, Crowley G, Picone JM, Shepherd GG, Skinner W, Hays P, Niecejewski RJ,
5
6
7 2553 Larsen M, She CY, Meriwether JW, Hernandez G, Jarvis MJ, Sipler DP, Tepley CA, O'Brien MS
8
9 2554 (2008) An empirical model of the Earth's horizontal wind fields: HWM07. *J. Geophys. Res.*
10
11 2555 113:A12304. doi:10.1029/2008JA013668
12
13
14 2556
15
16 2557 Ducic V, Artru J, Lognonn'e P (2003) Ionospheric remote sensing of the Denali Earthquake
17
18
19 2558 Rayleigh surface waves. *Geophys Res Lett* 30:1951. doi:10.1029/2003GL017812
20
21 2559
22
23
24 2560 Duly TM, Chapagain NP, Makela JJ (2013) Climatology of nighttime medium-scale traveling
25
26 2561 ionospheric disturbances (MSTIDs) in the Central Pacific and South American sectors. *Ann*
27
28
29 2562 *Geophys* 31:2229–2237 2013 www.ann-geophys.net/31/2229/2013/doi:10.5194/angeo-31-2229-
30
31 2563 2013
32
33
34 2564
35
36 2565 Ebihara Y, Nishitani N, Kikuchi T, Ogawa T, Hosokawa K, Fok M (2008) Two-dimensional
37
38 2566 observations of overshielding during a magnetic storm by the Super Dual Auroral Radar Network
39
40
41 2567 (SuperDARN) Hokkaido radar. *J Geophys Res* 113:A01213. doi:10.1029/2007JA012641
42
43 2568
44
45
46 2569 Ebihara, Y, Nishitani N, Kikuchi T, Ogawa T, Hosokawa K, Fok M-C, Thomsen MF
47
48 2570 (2009) Dynamical property of storm time subauroral rapid flows as a manifestation of complex
49
50
51 2571 structures of the plasma pressure in the inner magnetosphere. *J Geophys Res* 114:A01306.
52
53 2572 doi:10.1029/2008JA013614
54
55
56 2573
57
58
59
60
61
62
63
64
65

1
2
3
4 2574 Ebihara Y, Tanaka T, and Kikuchi T (2014) Counter equatorial electrojet and overshielding after
5
6 2575 substorm onset: Global MHD simulation study. J Geophys Res 119:7281-7296.
7
8
9 2576 doi:10.1002/2014JA020065
10
11
12 2577
13
14 2578 Eltrass A, Mahmoudian A, Scales WA, de Larquier S, Ruohoniemi JM, Baker JBH, Greenwald
15
16 2579 RA, Erickson PJ(2014) Investigation of the temperature gradient instability as the source of
17
18 2580 midlatitude quiet time decameter-scale ionospheric irregularities: 2. Linear analysis. J Geophys
19
20 Res Space Physics 119:4882–4893. doi:10.1002/2013JA019644
21
22 2581
23
24 2582
25
26 2583 Eltrass A, Scales WA, Erickson PJ, Ruohoniemi JM, Baker JBH (2016) Investigation of the role
27
28 2584 of plasma wave cascading processes in the formation of midlatitude irregularities utilizing GPS
29
30 and radar observations. Radio Sci 51. doi:10.1002/2015RS005790
31
32 2585
33
34 2586
35
36 2587 Erickson PJ, Foster JC, Holt JM (2002) Inferred electric field variability in the polarization jet
37
38 2588 from Millstone Hill *E* region coherent scatter observations. Radio Sci 37(2):1027.
39
40 doi:10.1029/2000RS002531
41
42 2589
43
44 2590
45
46 2591 Erickson PJ, Beroz F, Miskin MZ (2011) Statistical characterization of the American sector
47
48 2592 subauroral polarization stream using incoherent scatter radar. J Geophys Res 116:A00J21.
49
50 doi:10.1029/2010JA015738
51
52 2593
53
54 2594
55
56 2595 Fairfield DH (1969) Bow shock associated waves observed in the far upstream interplanetary
57
58 2596 medium. J Geophys Res 74:3541-3553
59
60
61
62
63
64
65

1
2
3
4 2597
5
6
7 2598 Fejer BG, Kelley MC (1980) Ionospheric irregularities. Rev Geophys, 18(2):401–454.
8
9 2599 doi:10.1029/RG018i002p00401
10
11
12 2600
13
14 2601 Feldstein YI, Starkov GV (1967) Dynamics of auroral belt and polar geomagnetic disturbances.
15
16 2602 Planet Space Sci 15(2):209–229. [https://doi.org/10.1016/0032-0633\(67\)90190-0](https://doi.org/10.1016/0032-0633(67)90190-0)
17
18
19 2603
20
21 2604 Fiori RAD, Boteler DH, Koustov AV, Haines GV, Ruohoniemi JM (2010) Spherical cap harmonic
22
23 2605 analysis of Super Dual Auroral Radar Network (SuperDARN) observations for generating maps of
24
25 2606 ionospheric convection. J Geophys Res 115:A07307. doi:10.1029/2009JA015055
26
27
28
29 2607
30
31 2608 Fiori RAD, Boteler DH, Koustov AV (2012) Response of ionospheric convection to sharp
32
33 2609 southward IMF turnings inferred from magnetometer and radar data. J Geophys Res 117:A09302.
34
35 2610 doi:10.1029/2012JA017755
36
37
38 2611
39
40
41 2612 Fiori RAD, Koustov AV, Chakraborty S, Ruohoniemi JM, Danskin DW, Boteler DH, Shepherd
42
43 2613 SG (2018) Examining the potential of the Super Dual Auroral Radar Network for monitoring the
44
45 2614 space weather impact of solar X-ray flares. Space Weather 16(9):1348-1362.
46
47 2615 <https://doi.org/10.1029/2018SW001905>
48
49
50 2616
51
52
53 2617 Foster JC, Burke WJ (2002) SAPS: A new categorization for sub-auroral electric fields. Eos, Trans
54
55 2618 Am Geophys Union 83:393. doi:10.1029/2002EO000289
56
57
58 2619
59
60
61
62
63
64
65

1
2
3
4
5
6
7
8
9
10
11
12
13
14
15
16
17
18
19
20
21
22
23
24
25
26
27
28
29
30
31
32
33
34
35
36
37
38
39
40
41
42
43
44
45
46
47
48
49
50
51
52
53
54
55
56
57
58
59
60
61
62
63
64
65

2620 Foster JC, Vo HB (2002) Average characteristics and activity dependence of the subauroral
2621 polarization stream. J Geophys Res 107(A12):1475. doi:10.1029/2002JA009409

2622
2623 Foster, JC, Erickson PJ, Lind FD, Rideout W (2004) Millstone Hill coherent-scatter radar
2624 observations of electric field variability in the sub-auroral polarization stream. Geophys Res
2625 Lett 31:L21803. doi:10.1029/2004GL021271

2626
2627 Foster JC, Coster AJ, Erickson PJ, Holt JM, Lind FD, Rideout W, McCready M, van Eyken A,
2628 Barnes RJ, Greenwald RA, Rich FJ (2005) Multiradar observations of the polar tongue of
2629 ionization. J Geophys Res Space Phys 110. doi:10.1029/2004JA010928

2630
2631 Freeman MP, Southwood DJ, Lester M, Yeoman TK, Reeves GD (1992) Substorm-associated
2632 radar auroral surges. J Geophys Res 97:12173. doi:10.1029/92JA00697

2633
2634 Friis-Christensen E, McHenry M A, Clauer C R, Vennerstrøm S. (1988) Ionospheric traveling
2635 convection vortices observed near the polar cleft: A triggered response to sudden changes in the
2636 solar wind. Geophys Res Lett 15(3):253-256. doi:10.1029/GL015i003p00253

2637
2638 Frissell NA, Baker JBH, Ruohoniemi JM, Clausen LBN, Kale ZC, Rae IJ, Kepko L, Oksavik K,
2639 Greenwald RA, West ML (2011) First radar observations in the vicinity of the plasmopause of
2640 pulsed ionospheric flows generated by bursty bulk flows. Geophys Res Lett 38:L01103.
2641 doi:10.1029/2010GL045857

2642

1
2
3
4 2643 Frissell NA, Baker JBH, Ruohoniemi JM, Gerrard AJ, Miller ES, Marini JP, West ML, Bristow
5
6
7 2644 WA (2014) Climatology of medium-scale traveling ionospheric disturbances observed by the
8
9 2645 midlatitude Blackstone SuperDARN radar. *J Geophys Res Space Physics* 119:7679–7697.
10
11
12 2646 doi:10.1002/2014JA019870
13
14 2647
15
16 2648 Frissell NA, Baker JBH, Ruohoniemi JM, Greenwald RA, Gerrard AJ, Miller ES, West ML (2016)
17
18
19 2649 Sources and characteristics of medium-scale traveling ionospheric disturbances observed by high-
20
21 2650 frequency radars in the North American sector. *J Geophys Res Space Physics* 121:3722–3739.
22
23
24 2651 doi:10.1002/2015JA022168
25
26 2652
27
28
29 2653 Gallardo-Lacourt B, Nishimura Y, Lyons LR, Zou S, Angelopoulos V, Donovan E, McWilliams
30
31 2654 KA, Ruohoniemi JM, Nishitani N (2014a) Coordinated SuperDARN THEMIS ASI observations
32
33 2655 of mesoscale flow bursts associated with auroral streamers. *J Geophys Res Space Phys* 119:142–
34
35
36 2656 150. doi:10.1002/2013JA019245
37
38 2657
39
40
41 2658 Gallardo-Lacourt B, Nishimura Y, Lyons LR, Ruohoniemi JM, Donovan E, Angelopoulos
42
43 2659 V, McWilliams KA, Nishitani N (2014b) Ionospheric flow structures associated with auroral
44
45
46 2660 beading at substorm auroral onset. *J Geophys Res Space Physics* 119:9150–9159.
47
48 2661 doi:10.1002/2014JA020298
49
50
51 2662
52
53 2663 Galperin YI, Pomomarev YN, Zosimova AG (1973) Direct measurements of ion drift velocity in
54
55 2664 the upper ionosphere during a magnetic storm, 2. Results of measurements during the November
56
57
58 2665 3, 1967 magnetic storm. *Cosmic Research (in Russian)* 11:283–292
59
60
61
62
63
64
65

1
2
3
4 2666
5
6
7 2667 Gault JK, Yeoman TK, Davies JA, Milan SE, Honary F (2002) SuperDARN HF propagation and
8
9 2668 absorption response to the substorm expansion phase. *Ann Geophys* 20:1631-1645
10
11 2669
12
13
14 2670 Gillies, RG, Hussey GC, Sofko GJ, McWilliams KA (2012), A statistical analysis of SuperDARN
15
16 2671 scattering volume electron densities and velocity corrections using a radar frequency shifting
17
18
19 2672 technique. *J Geophys Res* 117:A08320. doi:10.1029/2012JA017866
20
21 2673
22
23
24 2674 Gjerloev JW, Greenwald RA, Waters CL, Takahashi K, Sibeck D, Oksavik K, Barnes R, Baker J,
25
26 2675 Ruohoniemi JM (2007) Observations of Pi2 pulsations by the Wallops HF radar in association
27
28
29 2676 with substorm expansion. *Geophys Res Lett* 34: L20103. doi:10.1029/2007GL030492.
30
31 2677
32
33
34 2678 Glassmeier K-H, Hönisch M, Untiedt J (1989) Ground-based and satellite observations of
35
36 2679 traveling magnetospheric convection twin vortices. *J Geophys Res* 94(A3):2520–2528.
37
38 2680 doi:10.1029/JA094iA03p02520
39
40
41 2681
42
43
44 2682 Greenwald RA, Baker KB, Dudeney JD, Pinnock M, Jones TB, Thomas EC, Villain, J-PCerisier
45
46 2683 J-C, Senior C, Hanuise C, Hunsucker RD, Sofko G, Koehler J, Nielsen E, Pellinen R, Walker ADM,
47
48
49 2684 Sato N, Yamagishi H (1995) DARN/SuperDARN: A global view of the dynamics of high-latitude
50
51 2685 convection. *Space Sci Rev* 71:761-796
52
53
54 2686
55
56 2687 Greenwald RA, Oksavik K, Erickson PJ, Lind FD, Ruohoniemi JM, Bake JBH, Gjerloev JW
57
58
59 2688 (2006) Identification of the temperature gradient instability as the source of decameter-scale
60
61
62
63
64
65

1
2
3
4 2689 ionospheric irregularities on plasmopause field lines. *Geophys Res Lett* 33:L18105.
5
6 2690 doi:10.1029/2006GL026581
7
8
9 2691
10
11 2692 Greenwald RA, Oksavik K, Barnes R, Ruohoniemi JM, Baker JBH, Talaat ER (2008) First radar
12
13
14 2693 measurements of ionospheric electric fields at sub-second temporal resolution. *Geophys Res Lett*
15
16 2694 35:L03111. doi:10.1029/2007GL032164
17
18
19 2695
20
21 2696 Greenwald RA, Frissell N, de Larquier S (2017) The importance of elevation angle measurements
22
23 2697 in HF radar investigations of the ionosphere. *Radio Sci* 52:305–320. doi:10.1002/2016RS006186
24
25
26 2698
27
28
29 2699 Greenwood RI, Parkinson ML, Dyson PL, Schulz EW (2011) Dominant ocean wave direction
30
31 2700 measurements using the TIGER SuperDARN systems. *J Atmos Sol Terr Phys* 73(16):2379–2385
32
33 2701
34
35
36 2702 Grocott A, Milan SE, Baker JBH, Freeman MP, Lester M, Yeoman TK (2011) Dynamic
37
38 2703 subauroral ionospheric electric fields observed by the Falkland Islands radar during the course of
39
40
41 2704 a geomagnetic storm. *J Geophys Res* 116:A11202. doi:10.1029/2011JA016763
42
43 2705
44
45
46 2706 Grocott A, Hosokawa K, Ishida T, Lester M, Milan SE, Freeman MP, Sato N, Yukimatu AS (2013)
47
48 2707 Characteristics of medium-scale traveling ionospheric disturbances observed near the Antarctic
49
50
51 2708 Peninsula by HF radar. *J Geophys Res Space Physics* 118:5830–5841. doi:10.1002/jgra.50515
52
53 2709
54
55
56
57
58
59
60
61
62
63
64
65

1
2
3
4 2710 Gurevich AV, Borisov ND, Zybin KP (1997) Ionospheric turbulence induced in the lower part of
5
6
7 2711 the *E* region by the turbulence of the neutral atmosphere. J Geophys Res 102:379–388.
8
9 2712 doi:10.1029/96JA00163
10
11
12 2713
13
14 2714 Hall GE, MacDougall JW, Moorcroft DR, St-Maurice J-P, Manson AH, Meek CR (1997) Super
15
16 2715 Dual Auroral Radar Network observations of meteor echoes. J Geophys Res 102:14603-14624.
17
18
19 2716 doi:10.1029/97JA00517
20
21 2717
22
23
24 2718 Hayashi H, Nishitani N, Ogawa T, Otsuka Y, Tsugawa T, Hosokawa K, Saito A (2010) Large -
25
26 2719 scale traveling ionospheric disturbance observed by SuperDARN Hokkaido HF radar and GPS
27
28
29 2720 networks on 15 December 2006. J Geophys Res 115:A06309. doi:10.1029/2009JA014297
30
31 2721
32
33
34 2722 He L-S, Dyson PL, Parkinson ML, Wan W (2004) Studies of medium scale travelling ionospheric
35
36 2723 disturbances using TIGER SuperDARN radar sea echo observations. Ann Geophys 22:4077–4088.
37
38
39 2724 <https://doi.org/10.5194/angeo-22-4077-2004>
40
41 2725
42
43
44 2726 Hibbins RE, Freeman MP, Milan SE, Ruohoniemi JM (2011) Winds and tides in the midlatitude
45
46 2727 Southern hemisphere upper atmosphere recorded with the Falkland Islands SuperDARN radar.
47
48 2728 Ann Geophys 29:1985-1996. <https://doi.org/10.5194/angeo-29-1985-2011>
49
50
51 2729
52
53 2730 Hocke K, Schlegel K (1996) A review of atmospheric gravity waves and traveling ionospheric
54
55
56 2731 disturbances: 1982–1995. Ann Geophys 14:917–940. <https://doi.org/10.1007/s00585-996-0917-6>
57
58 2732
59
60
61
62
63
64
65

1
2
3
4 2733 Hori T, Shinbori A, Nishitani N, Kikuchi T, Fujita S, Nagatsuma T, Troshichev O, Yumoto K,
5
6
7 2734 Moiseyev A, Seki K (2012) Evolution of negative SI-induced ionospheric flows observed by
8
9 2735 SuperDARN King Salmon HF radar. J Geophys Res 117:A12223. doi:10.1029/2012JA018093
10
11
12 2736
13
14 2737 Hori T, Shinbori A, Fujita S, Nishitani N (2015) IMF-By dependence of transient ionospheric flow
15
16 2738 perturbation associated with sudden impulses: SuperDARN observations. Earth, Planets Space
17
18
19 2739 67:190. doi:10.1186/s40623-015-0360-6
20
21 2740
22
23
24 2741 Horvath I, Essex EA (2003) The Weddell Sea Anomaly observed with the Topex satellite data. J
25
26 2742 Atmos Solar Terr Phys 65:693–706. doi:10.1016/S1364-6826(03)00083-X
27
28
29 2743
30
31 2744 Hosokawa K, Nishitani N (2010) Plasma irregularities in the duskside subauroral ionosphere as
32
33 2745 observed with midlatitude SuperDARN radar in Hokkaido, Japan. Radio Sci 45:RS4003.
34
35
36 2746 doi:10.1029/2009RS004244
37
38 2747
39
40
41 2748 Hosokawa K, Iyemori T, Yukimatu AS, Sato N (2001) Source of field-aligned irregularities in the
42
43 2749 subauroral F region as observed by the SuperDARN radars. J Geophys Res 106:24713.
44
45
46 2750 doi:10.1029/2001JA900080
47
48 2751
49
50
51 2752 Hosokawa K, Ogawa T, Arnold N, Lester M, Sato N, Yukimatu (2005) Extraction of polar
52
53 2753 mesosphere summer echoes from SuperDARN data. Geophys Res Lett 32:L12801.
54
55 2754 10.1029/2005GL022788
56
57
58 2755
59
60
61
62
63
64
65

1
2
3
4 2756 Hosokawa K, Tsugawa T, Shiokawa K, Otsuka Y, Nishitani N, Ogawa T, Hairston MR (2010)
5
6
7 2757 Dynamic temporal evolution of polar cap tongue of ionization during magnetic storm. *J Geophys*
8
9 2758 *Res Space Phys* 115:A12333. doi:10.1029/2010JA015848
10
11
12 2759
13
14 2760 Huang C, Sazykin S, Spiro R, Goldstein J, Crowley G, Ruohoniemi JM (2006) Storm-time
15
16 2761 penetration electric fields and their effects. *EOS* 87:131–132
17
18
19 2762
20
21 2763 Hughes WJ (1994) Magnetospheric ULF waves: A tutorial with a historic perspective. *Solar wind*
22
23
24 2764 sources of magnetospheric ultra-low frequency waves. *Geophys Monogr Ser*, 81:1-11 eds
25
26 2765 Engebretson MJ, Takahashi K, Scholer M, AGU Washington DC
27
28
29 2766
30
31 2767 Hughes JM, Bristow WA, Greenwald RA, Barnes RJ (2002) Determining characteristics of HF
32
33
34 2768 communications links using SuperDARN. *Ann Geophys* 20:1023–1030
35
36 2769
37
38 2770 Hunsucker R (1982) Atmospheric gravity waves generated in the high latitude ionosphere: A
39
40
41 2771 review. *Rev Geophys Space Phys* 20:293– 315
42
43 2772
44
45
46 2773 Ichihara A, Nishitani N, Ogawa T, Tsugawa T (2013) Northward-propagating nighttime medium-
47
48 2774 scale traveling ionospheric disturbances observed with SuperDARN Hokkaido HF radar and
49
50
51 2775 GEONET. *Advances in Polar Science* 24:42–49. doi:10.3724/SP.J.1085.2013.00042
52
53 2776
54
55
56
57
58
59
60
61
62
63
64
65

1
2
3
4 2777 Ishida T, Hosokawa K, Shibata T, Suzuki S, Nishitani N, Ogawa T (2008) SuperDARN
5
6 2778 observations of daytime MSTIDs in the auroral and midlatitudes: Possibility of long-distance
7
8
9 2779 propagation. Geophys Res Lett 35:L13102 doi:10.1029/2008GL034623
10
11
12 2780
13
14 2781 Jansen F, Pirjola R (2004) Space Weather Research Elucidates Risks to Technological
15
16 2782 Infrastructure. EOS 85(25): 245-246
17
18
19 2783
20
21
22 2784 Jones RM, Stephenson JJ (1975) A versatile three - dimensional ray tracing computer program for
23
24 2785 radio waves in the ionosphere. OT Rep 75 - 76.PB2488567 US Dept of Comm, Washington DC
25
26
27 2786
28
29
30 2787 Joshi, PP, Baker JBH, Ruohoniemi JM, Makela JJ, Fisher DJ, Harding BJ, Frissell NA, Thomas
31
32 2788 EG (2015) Observations of storm time midlatitude ion-neutral coupling using SuperDARN radars
33
34 2789 and NATION Fabry-Perot interferometers. J Geophys Res Space Physics 120:8989–9003.
35
36
37 2790 doi:10.1002/2015JA021475
38
39 2791
40
41
42 2792 Kane TA, Makarevich RA (2010) HF radar observations of the F region ionospheric plasma
43
44 2793 response to Storm Sudden Commencements. J Geophys Res 115:A07320.
45
46
47 2794 doi:10.1029/2009/2009JA014974
48
49 2795
50
51
52 2796 Kane TA, Makarevich RA, Devlin JC (2012) HF radar observations of ionospheric backscatter
53
54 2797 during geomagnetically quiet periods. Ann Geophys 30(1):221-233. doi:10.5194/angeo-30-221-
55
56 2798 2012
57
58
59 2799
60
61
62
63
64
65

1
2
3
4 2800 Karlsson T, Marklund GT, Blomberg LG, Mälkki A (1998) Subauroral electric fields observed by
5
6
7 2801 the Freja satellite: A statistical study. J Geophys Res 103:4327. doi:10.1029/97JA00333
8
9 2802
10
11 2803 Kataoka R, Nishitani N, Ebihara Y, Hosokawa K, Ogawa T, Kikuchi T, Miyoshi Y
12
13
14 2804 (2007) Dynamic variations of a convection flow reversal in the subauroral postmidnight sector as
15
16 2805 seen by the SuperDARN Hokkaido HF radar. Geophys Res Lett 34:L21105.
17
18
19 2806 doi:10.1029/2007GL031552
20
21 2807
22
23 2808 Kataoka R, Hosokawa K, Nishitani N, Miyoshi Y (2009) SuperDARN Hokkaido radar observation
24
25
26 2809 of westward flow enhancement in subauroral latitudes. Ann. Geophys 27:1695-1699. www.ann-
27
28
29 2810 geophys.net/27/1695/2009/
30
31 2811
32
33 2812 Kawano H, Yukimatu AS, Tanaka Y, Saita S, Nishitani N, Hori T (2016) SC-Triggered 1.6 mHz
34
35
36 2813 Waves Including an Interval with latitude-Dependent Phase shift Observed by the SuperDARN
37
38 2814 Hokkaido East Radar in Mid Latitudes: Possible Global Ionospheric Cavity-Mode Waves and their
39
40
41 2815 Field-Line Resonance with Poloidal Alfvén-Mode waves. Mem. Fac. Sci. Kyushu Univ Ser. D.
42
43 2816 Earth Planet Sci. XXXIV:1-15
44
45
46 2817
47
48 2818 Kelley MC, Fejer BG, Gonzales CA (1979) An explanation for anomalous equatorial ionospheric
49
50
51 2819 electric fields associated with a northward turning of the interplanetary magnetic field. Geophys
52
53 2820 Res Lett 6:301–304. doi:10.1029/GL006i004p00301
54
55 2821
56
57
58
59
60
61
62
63
64
65

1
2
3
4 2822 Kelley MC (2011) On the origin of mesoscale TIDs at midlatitudes. *Ann Geophys* 29(2):361–366.
5
6
7 2823 <https://doi.org/10.5194/angeo-29-361-2011>, 2011
8
9 2824
10
11 2825 Kikuchi T, Ebihara Y, Hashimoto KK, Kataoka R, Hori T, Watari S, Nishitani N (2010)
12
13 Penetration of the convection and overshielding electric fields to the equatorial ionosphere during
14 2826 a quasiperiodic DP 2 geomagnetic fluctuation event. *J Geophys Res* 115:A05209.
15
16 2827 doi:10.1029/2008JA013948
17
18 2828
19
20
21 2829
22
23 2830 Killeen TL, Hays PB, Carignan GR, Heelis RA, Hanson WB, Spencer NW, Brace LH (1984) Ion-
24
25 neutral coupling in the high-latitude *F* region: Evaluation of ion heating terms from Dynamics
26 2831 Explorer 2. *J Geophys Res* 89(A9):7495–7508. doi:10.1029/JA089iA09p07495
27
28 2832
29
30
31 2833
32
33 2834 Kim K-H, Lee D-H, Shiokawa K, Lee E, Park J-S, Kwon H-J, Angelopoulos
34
35 V, Park Y-D, Hwang J, Nishitani N, Hori T, Koga K, Obara T, Yumoto K,
36 2835
37 Baishev DG (2012) Magnetospheric responses to the passage of the interplanetary shock on 24
38 2836
39 November 2008. *J Geophys Res* 117:A10209. doi:10.1029/2012JA017871
40
41 2837
42
43 2838
44
45
46 2839 Kim S-I, Kim K-H, Kwon H-J, Jin H, Lee E, Jee G, Nishitani N, Hori T, Lester M, Wygant JR
47
48 (2017) SC-associated electric field variations in the magnetosphere and ionospheric convective
49 2840
50 flows. *J Geophys Res Sp Phys* 122:11044–11057. doi:10.1002/2017JA024611
51 2841
52
53
54 2842
55
56
57
58
59
60
61
62
63
64
65

1
2
3
4 2843 Kotake N, Otsuka Y, Tsugawa T, Ogawa T, and Saito A (2006) Climatological study of GPS total
5
6
7 2844 electron content variations caused by medium-scale traveling ionospheric disturbances. *J Geophys*
8
9 2845 *Res* 111:A04306. doi:10.1029/2005JA011418
10
11 2846
12
13
14 2847 Kotake N, Otsuka Y, Ogawa T, Tsugawa T, Saito A (2007) Statistical study of medium-scale
15
16 2848 traveling ionospheric disturbances observed with the GPS networks in Southern California. *Earth*
17
18
19 2849 *Planets Space* 59(2):95–102
20
21 2850
22
23 2851 Koustov AV, Drayton RA, Makarevich RA, McWilliams KA, St-Maurice J-P, Kikuchi T, Frey
24
25
26 2852 HU (2006) Observations of high-velocity SAPS-like flows with the King Salmon SuperDARN
27
28
29 2853 radar. *Ann Geophys* 24:1591–1608. doi:10.5194/angeo-24-1591-2006
30
31 2854
32
33 2855 Koustov AV, Nishitani N, Ebihara Y, Kikuchi T, Hairston MR, André D (2008) Subauroral
34
35
36 2856 polarization streams: Observations with the Hokkaido and King Salmon SuperDARN radars and
37
38 2857 modeling. *Ann Geophys* 26:3317–3327
39
40
41 2858
42
43 2859 Koustov AV, Nishitani N, Ponomarenko PV, Shiokawa K, Suzuki S, Shevtsov BM, MacDougall
44
45
46 2860 JW (2009) Joint observations of a traveling ionospheric disturbance with the Paratunka OMTI
47
48 2861 camera and the Hokkaido HF radar. *Ann Geophys* 27:2399–2406. <https://doi.org/10.5194/angeo->
49
50 2862 [27-2399-2009](https://doi.org/10.5194/angeo-27-2399-2009)
51
52
53 2863
54
55 2864 Koustov AV, Yakymenko KN, Nishitani N, Ponomarenko PV (2014) Hokkaido HF radar
56
57
58 2865 signatures of periodically reoccurring nighttime medium scale traveling ionospheric disturbances
59
60
61
62
63
64
65

1
2
3
4 2866 detected at short ranges. J Geophys Res Space Physics 119:1200–1218.
5
6
7 2867 doi:10.1002/2013JA019422
8
9 2868
10
11 2869 Kubota M, Conde M, Ishii M, Murayama Y, Jin H (2011) Characteristics of nighttime medium -
12
13
14 2870 scale traveling ionospheric disturbances observed over Alaska. J Geophys Res 116:A05307.
15
16
17 2871 doi:10.1029/2010JA016212
18
19 2872
20
21 2873 Kumar VV, Makarevich RA, Kane TA, Ye H, Devlin JC, Dyson PL (2011) On the spatiotemporal
22
23
24 2874 evolution of the ionospheric backscatter during magnetically disturbed periods as observed by the
25
26
27 2875 TIGER Bruny Island HF radar. J Atmos Sol Terr Phys 73(13):1940-1952
28
29 2876
30
31 2877 Kunduri, BSR, Baker JBH, Ruohoniemi JM, Clausen LBN, Grocott A, Thomas EG, Freeman MP,
32
33
34 2878 Talaat ER (2012) An examination of inter-hemispheric conjugacy in a subauroral polarization
35
36
37 2879 stream. J Geophys Res 117:A08225. doi:10.1029/2012JA017784
38
39 2880
40
41 2881 Kunduri, BSR, Baker JBH, Ruohoniemi JM, Thomas EG, Shepherd SG, Sterne KT
42
43
44 2882 (2017) Statistical characterization of the large-scale structure of the subauroral polarization
45
46
47 2883 stream. J Geophys Res Space Physics 122:6035–6048. doi:10.1002/2017JA024131
48
49 2884
50
51 2885 Lester M, Hughes WJ, Singer HJ (1983) Polarization patterns of Pi2 Magnetic Pulsations and the
52
53
54 2886 substorm Current Wedge. J Geophys Res 88:7958-7966
55
56 2887
57
58
59
60
61
62
63
64
65

1
2
3
4 2888 Lester M, Chapman PJ, Cowley SWH, Crooks SJ, Davies JA, Hamadyk P, McWilliams KA, Milan
5
6 2889 SE, Parsons MJ, Payne DB, Thomas EC, Thornhill JD, Wade NM, Yeoman TK, Barnes RJ (2004)
7
8
9 2890 Stereo CUTLASS – A new capability for the SuperDARN radars. *Ann Geophys* 22:459 - 473
10
11
12 2891
13
14 2892 Lomb NR (1976) Least-squares frequency analysis of unequally spaced data. *Astrophys Space Sci*
15
16 2893 39:447–462. doi:10.1007/BF00648343.
17
18
19 2894
20
21 2895 Lyons LR, Nishimura Y, Kim H-J, Donovan E, Angelopoulos V, Sofko G, Nicolls M, Heinselman
22
23 2896 C, Ruohoniemi JM, Nishitani N (2011) Possible connection of polar cap flows to pre- and post-
24
25
26 2897 substorm onset PBIs and streamers. *J Geophys Res* 116:A12225. doi:10.1029/2011JA016850
27
28
29 2898
30
31 2899 Lyons LR, Nishimura Y, Gallardo-Lacourt B, Nicolls MJ, Chen S, Hampton DL, Bristow
32
33 2900 WA, Ruohoniemi JM, Nishitani N, Donovan EF, Angelopoulos V (2015) Azimuthal flow bursts
34
35
36 2901 in the inner plasma sheet and possible connection with SAPS and plasma sheet earthward flow
37
38 2902 bursts. *J Geophys Res Space Phys* 120:5009–5021. doi: 10.1002/2015JA021023
39
40
41 2903
42
43 2904 Lyons LR, Gallardo-Lacourt B, Zou S, Weygand JM, Nishimura Y, Li W, Gkioulidou M,
44
45 2905 Angelopoulos V, Donovan EF, Ruohoniemi JM, Anderson BJ, Shepherd SG, Nishitani N (2016)
46
47
48 2906 The 17 March 2013 storm: Synergy of observations related to electric field modes and their
49
50
51 2907 ionospheric and magnetospheric Effects. *J Geophys Res Space Phys* 121:10,880-10,897.
52
53 2908 doi:10.1002/2016JA023237
54
55 2909
56
57
58
59
60
61
62
63
64
65

1
2
3
4 2910 Makarevich RA, Dyson PL (2007) Dual HF radar study of the subauroral polarization stream. Ann
5
6
7 2911 Geophys 25:2579–2591. www.ann-geophys.net/25/2579/2007/
8
9 2912
10
11 2913 Makarevich RA, Kellerman AC, Bogdanova Y.V., Koustov AV (2009) Time evolution of the
12
13
14 2914 subauroral electric fields: A case study during a sequence of two substorms. J Geophys Res
15
16 2915 114:A04312. doi:10.1029/2008JA013944
17
18
19 2916
20
21 2917 Makarevich RA, Kellerman AC, Devlin JC, Ye H, Lyons LR, Nishimura Y (2011) SAPS
22
23
24 2918 intensification during substorm recovery: A multi-instrument case study. J Geophys Res
25
26 2919 116:A11311. doi:10.1029/2011JA016916
27
28
29 2920
30
31 2921 Makarevich RA, Bristow WA (2014) Fine structure of subauroral electric field and electron
32
33
34 2922 content. J Geophys Res Space Phys 119:3789–3802. doi:10.1002/2014JA019821
35
36 2923
37
38 2924 Marchaudon A, and Blelly P-L (2015) A new interhemispheric 16-moment model of the
39
40
41 2925 plasmasphere-ionosphere system: IPIM. J. Geophys. Res. Space Physics 120: doi:
42
43 2926 10.1002/2015JA021193
44
45
46 2927
47
48 2928 Mauk BH, Fox NJ, Kanekal SG, Kessel RL, Sibeck DG, Ukhorskiy, A (2013) Science objectives
49
50
51 2929 and rationale for the Radiation Belt Storm Probes mission. Space Sci Rev 179:3-
52
53 2930 27. <https://doi.org/10.1007/s11214-012-9908-y>
54
55 2931
56
57
58
59
60
61
62
63
64
65

- 1
2
3
4 2932 McFadden J, Carlson C, Larson D, Ludlam M, Abiad R, Elliott B, Turin P, Marckwordt M,
5
6
7 2933 Angelopoulos V (2008) The THEMIS ESA plasma instrument and in-flight calibration. Space Sci
8
9 2934 Rev 14:277-302.
- 10
11
12 2935
- 13
14 2936 Milan SE, Yeoman TK, Lester M, Thomas EC, Jones TB (1997a) Initial backscatter occurrence
15
16 2937 statistics for the CUTLASS HF radars. Ann Geophys 15:703–718
17
18
19 2938
- 20
21 2939 Milan SE, Jones TB, Robinson TR, Thomas EC, and Yeoman TK (1997b) Interferometric
22
23
24 2940 evidence for the observation of ground backscatter originating behind the CUTLASS coherent
25
26 2941 HF radars. Ann. Geophys. 15:29-39
27
28
29 2942
- 30
31 2943 Milan SE, Lester M (1998) Simultaneous observations at different altitudes of ionospheric
32
33
34 2944 backscatter in the eastward electrojet. Ann Geophys 16:55-68
35
36 2945
- 37
38 2946 Milan SE, Lester M, Cowley SWH, Brittnacher M (2000) Convection and auroral response to a
39
40
41 2947 southward turning of the IMF: Polar UVI, CUTLASS, and IMAGE signatures of transient
42
43 2948 magnetic flux transfer at the magnetopause. J Geophys Res 105(A7):15741–15755.
44
45
46 2949 doi:10.1029/2000JA900022
47
- 48 2950
- 49
50
51 2951 Milan SE, Lester M (2001) A classification of spectral populations observed in HF radar
52
53 2952 backscatter from the E region electrojets. Ann Geophys 19:189–204
54
55
56 2953

1
2
3
4
5
6
7
8
9
10
11
12
13
14
15
16
17
18
19
20
21
22
23
24
25
26
27
28
29
30
31
32
33
34
35
36
37
38
39
40
41
42
43
44
45
46
47
48
49
50
51
52
53
54
55
56
57
58
59
60
61
62
63
64
65

2954 Milan SE, Lester M, Sato N, Takizawa H (2001) On the altitude dependence of the spectral
2955 characteristics of decametre-wavelength E region backscatter and the relationship with optical
2956 auroral forms. *Ann Geophys* 19:205 - 217

2957
2958 Milan SE, Lester, Cowley SWH, Oksavik K, Brittnacher M, Greenwald RA, Sofko G, Villain J-P
2959 (2003) Variations in polar cap area during two substorm cycles. *Ann Geophys* 21:1121 - 1140

2960
2961 Milan SE, M Lester, TK Yeoman, TR Robinson, MV Uspensky, and J-P Villain (2004) HF radar
2962 observations of high-aspect angle backscatter from the E region. *Ann. Geophys.* 22:829-847

2963
2964 Milan SE, Grocott A, de Larquier S, Lester M, Yeoman TK, Freeman MP, Chisham G (2013)
2965 Traveling ionospheric disturbances in the Weddell Sea Anomaly associated with geomagnetic
2966 activity. *J Geophys Res Space Physics* 118:6608–6617. doi:10.1002/jgra.50566

2967
2968 Mishin EV, Burke WJ, Huang CY, Rich FJ (2003) Electromagnetic wave structures within
2969 subauroral polarization streams. *J Geophys Res* 108(A8):1309. doi:10.1029/2002JA009793

2970
2971 Mishin, E, Burke W (2005) Stormtime coupling of the ring current, plasmasphere and topside
2972 ionosphere: Electromagnetic and plasma disturbances. *J Geophys Res* 110:A07209.
2973 doi:10.1029/2005JA011021

2974
2975 Mishin EV, Puhl-Quinn PA (2007) SAID: Plasmaspheric short circuit of substorm
2976 injections. *Geophys Res Lett* 34:L24101. doi:10.1029/2007GL031925

1
2
3
4 2977
5
6
7 2978 Miyoshi Y, Ono T, Takashima T, Asamura K, Hirahara M, Kasaba Y, Matsuoka A, Kojima H,
8
9 2979 Shiokawa K, Seki K, Fujimoto M, Nagatsuma T, Cheng CZ, Kazama Y, Kasahara S, Mitani T,
10
11 2980 Matsumoto H, Higashio N, Kumamoto A, et al (2012) The Energization and Radiation in Geospace
12
13 (ERG) Project. In: Summers D, Mann IR, Baker DN, Shultz M (eds) Dynamics of the Earth's
14 2981 Radiation Belts and Inner Magnetosphere, Geophysical Monograph Series, 199. AGU,
15
16 2982 Washington, D. C., pp 103–116
17
18
19 2983
20
21
22 2984
23
24 2985 Nagano H, Nishitani N, Hori T (2015) Occurrence characteristics and lowest speed limit of Sub-
25
26 Auroral Polarization Stream (SAPS) observed by the SuperDARN Hokkaido East radar. Earth
27 2986 Planets Space 67:126. doi:10.1186/s40623-015-0299-7
28
29 2987
30
31
32 2988
33
34 2989 Nishida A (1968) Coherence of geomagnetic DP 2 fluctuations with interplanetary magnetic
35
36 2990 variations. J Geophys Res 73:5549–5559. doi:10.1029/JA073i017p05549
37
38
39 2991
40
41
42 2992 Nishimura Y, Lyons LR, Zou S, Xing X, Angelopoulos V, Mende SB, Bonnell JW, Larson D,
43
44 2993 Auster U, Hori T, Nishitani N, Hosokawa K, Sofko G, Nicolls M, Heinselman C (2010) Preonset
45
46 2994 time sequence of auroral substorms: Coordinated observations by all-sky imagers, satellites, and
47
48 2995 radars. J Geophys Res Sp Phys 115: A00108. doi:10.1029/2010JA015832
49
50
51
52 2996
53
54
55 2997 Nishitani N, Ogawa T (2005) Model calculations of possible ionospheric backscatter echo area for
56
57 2998 a mid-latitude HF radar. Adv Polar Upper Atmos Res 19:55-62
58
59
60
61
62
63
64
65

1
2
3
4 2999
5
6
7 3000 Nishitani N, Ogawa T, Sato N, Yamagishi H, Pinnock M, Villain J-P, Sofko G, Troshichev O
8
9 3001 (2002) A study of the dusk convection cell's response to an IMF southward turning. J Geophys
10
11 Res 107(A3). doi:10.1029/2001JA900095
12 3002
13
14 3003
15
16 3004 Nishitani N, Ogawa T, Otsuka Y, Hosokawa K, Hori T (2011) Propagation of large amplitude
17
18 ionospheric disturbances with velocity dispersion observed by the SuperDARN Hokkaido radar
19 3005
20 after the 2011 off the Pacific coast of Tohoku Earthquake. Earth Planets and Space 63(7):891-896.
21 3006
22 doi: 10.5047/eps.2011.07.003
23
24 3007
25
26 3008
27
28 3009 Norouzi-Sedeh L, Waters CL, Menk FW (2015) Survey of ULF wave signatures seen in the
29
30 Tasman International Geospace Environment Radars data. J Geophys Res 120:949-963
31 3010
32 doi:10.1002/2014JA020652
33 3011
34
35
36 3012
37
38 3013 Occhipinti G, Dorey P, Farges T, Lognonné P (2010) Nostradamus: the radar that wanted to be a
39
40 seismometer. Geophys Res Lett 37:L18104. doi:10.1029/2010GL044009
41 3014
42
43 3015
44
45 3016 Ogawa T, Nishitani N, Sato N, Yamagishi H, Yukimatu AS (2002a) Upper mesosphere summer
46
47 echoes detected with the antarctic Syowa HF radar. Geophys Res Lett 29:1157.
48 3017
49 doi:10.1029/2001GL014094
50 3018
51
52
53 3019
54
55
56
57
58
59
60
61
62
63
64
65

- 1
2
3
4 3020 Ogawa, T, Balan N, Otsuka Y, Shiokawa K, Ihara C, Shimomai T, Saito A (2002b) Observations
5
6
7 3021 and modeling of 630 nm airglow and total electron content associated with traveling ionospheric
8
9 3022 disturbances over Shigaraki, Japan. *Earth Planets Space* 54:45–56
10
11
12 3023
13
14 3024 Ogawa T, Arnold NF, Kirkwood S, Nishitani N, Lester M (2003) Finland HF and Esrange MST
15
16 3025 radar observations of polar mesosphere summer echoes. *Ann Geophys* 21:1047 - 1055
17
18
19 3026
20
21 3027 Ogawa T, Nishitani N, Otsuka Y, Shiokawa K, Tsugawa T, Hosokawa K (2009) Medium-scale
22
23 3028 traveling ionospheric disturbances observed with the SuperDARN Hokkaido radar, all-sky imager,
24
25
26 3029 and GPS network and their relation to concurrent sporadic E irregularities. *J Geophys Res*
27
28
29 3030 114:A03316. doi:10.1029/2008JA013893
30
31 3031
32
33 3032 Ogawa T, Nishitani N, Tsugawa T, Shiokawa K (2012) Giant ionospheric
34
35 3033 disturbances observed with the SuperDARN Hokkaido HF radar and GPS network after
36
37
38 3034 the 2011 Tohoku earthquake. *Earth Planets Space* 64(12): 1295-1307
39
40
41 3035
42
43 3036 Ogawa, T, Nishitani N, Kawamura S, Murayama Y(2013) Mesosphere summer echoes observed
44
45 3037 with the SuperDARN Hokkaido HF radar at Rikubetsu, Japan (43.5N). *Earth Planets Space*
46
47
48 3038 65:1593-1597. doi:10.5047/eps.2013.07.009
49
50
51 3039
52
53 3040 Oinats AV, Kurkin VI, Nishitani N (2015) Statistical study of medium-scale traveling ionospheric
54
55 3041 disturbances using SuperDARN Hokkaido ground backscatter data for 2011. *Earth Planets Space*
56
57
58 3042 67:22. doi: 10.1186/s40623-015-0192-4
59
60
61
62
63
64
65

- 1
2
3
4 3043
5
6
7 3044 Oinats AV, Nishitani N, Ponomarenko P, Bergardt O, Ratovsky K (2016a) Statistical
8
9 3045 characteristics of medium-scale traveling ionospheric disturbances revealed from the Hokkaido
10
11 3046 East and Ekaterinburg HF radar data. Earth Planets Space 68:8. doi: 10.1186/s40623-016-0390-8
12
13
14 3047
15
16 3048 Oinats AV, Nishitani N, Ponomarenko P, Ratovsky KG (2016b) Diurnal and seasonal behavior of
17
18
19 3049 the Hokkaido East SuperDARN ground backscatter: simulation and observation. Earth Planets and
20
21 3050 Space 68:18. doi:10.1186/s40623-015-0378-9
22
23
24 3051
25
26 3052 Oksavik, K, Greenwald RA, Ruohoniemi JM, Hairston MR, Paxton LJ, Baker JBH, Gjerloev JW,
27
28
29 3053 and Barnes RJ (2006) First observations of the temporal/spatial variation of the sub-auroral
30
31 3054 polarization stream from the SuperDARN Wallops HF radar. Geophys Res Lett 33:L12104.
32
33 3055 doi:10.1029/2006GL026256.
34
35
36 3056
37
38 3057 Otsuka Y, Kotake N, Shiokawa K, Ogawa T, Tsugawa T, Saito A (2011) Statistical Study of
39
40
41 3058 Medium-Scale Traveling Ionospheric Disturbances Observed with a GPS Receiver Network in
42
43 3059 Japan. Aeronomy of the Earth's Atmosphere and Ionosphere IAGA Special Sopron Book Series
44
45
46 3060 Volume 2 Part 3: 291-299. doi: 10.1007/978-94-007-0326-1_21
47
48 3061
49
50
51 3062 Parkinson ML, Pinnock M, Ye H, Hairston MR, Devlin JC, Dyson PL, Morris RJ, Ponomarenko
52
53 3063 P (2003a) On the lifetime and extent of an auroral westward flow channel (AWFC) observed
54
55 3064 during a magnetospheric substorm. Ann Geophys 21:893–913
56
57
58 3065
59
60
61
62
63
64
65

1
2
3
4
5
6
7
8
9
10
11
12
13
14
15
16
17
18
19
20
21
22
23
24
25
26
27
28
29
30
31
32
33
34
35
36
37
38
39
40
41
42
43
44
45
46
47
48
49
50
51
52
53
54
55
56
57
58
59
60
61
62
63
64
65

3066 Parkinson ML, Devlin JC, Ye H, Waters CL, Dyson PL, Breed AM, Morris RJ (2003b) On the
3067 occurrence and motion of decametre-scale irregularities in the sub-auroral, auroral, and polar cap
3068 ionosphere. *Ann Geophys* 21:1847-1868

3069
3070 Parkinson ML, Pinnock M, Wild JA, Lester M, Yeoman TK, Milan SE, Ye H, Devlin JC, Frey
3071 HU, Kikuchi T (2005) Interhemispheric asymmetries in the occurrence of magnetically conjugate
3072 sub-auroral polarisation streams. *Ann Geophys* 23:1371-1390

3073
3074 Parkinson ML, Dyson PL, Pinnock M (2006) On the occurrence of auroral westward flow channels
3075 and substorm phase. *Advances in Space Research* 38(8):1755-1762

3076
3077 Parris RT, Bristow WA (2009) Observations and characterization of HAARP induced F-region
3078 decameter scale plasma density irregularities using the new imaging capabilities of the Kodiak
3079 Island SuperDARN radar. American Geophysical Union, Fall Meeting 2009

3080
3081 Perkins F (1973) Spread *F* and ionospheric currents. *J Geophys Res* 78:218–226.
3082 doi:10.1029/JA078i001p00218

3083
3084 Pettigrew ED, Shepherd SG, Ruohoniemi JM (2010) Climatological patterns of high-latitude
3085 convection in the Northern and Southern hemispheres: Dipole tilt dependencies and
3086 interhemispheric comparisons. *J Geophys Res* 115:A07305. doi:10.1029/2009JA014956

3087

1
2
3
4 3088 Puhl-Quinn P, Matsui H, Mishin E, Mouikis C, Kistler L, Khotyaintsev Y, De'cre'au P, Lucek E
5
6
7 3089 (2007) Cluster and DMSP Observations of SAID electric fields. J Geophys Res 112:A05219.
8
9 3090 doi:10.1029/ 2006JA012065
10
11
12 3091
13
14 3092 Pinnock M, Rodger AS, Dudeney JR, Baker KB, Greenwald RA, Greenspan M (1993)
15
16 3093 Observations of an enhanced convection channel in the cusp ionosphere. J Geophys Res 98: 3767-
17
18
19 3094 3776
20
21 3095
22
23 3096 Ponomarenko PV, Menk FW, Waters CL (2003) Visualization of ULF waves in SuperDARN data.
24
25
26 3097 Geophys Res Lett 30:1926-1929. doi:10.1029/2003GL017757
27
28
29 3098
30
31 3099 Ponomarenko PW, Menk FW, Waters CL, Sciffer MD (2005) Pc3-4 ULF waves observed by the
32
33 3100 SuperDARN TIGER radar. Ann Geophys 23:1271-1280. <https://doi.org/10.5194/angeo-23-1271->
34
35
36 3101 2005
37
38 3102
39
40
41 3103 Ponomarenko PV, Waters CL, St-Maurice J-P (2010) Upstream Pc3-4 waves: Experimental
42
43 3104 evidence of propagation to the nightside plasmopause/plasmatrough. Geophys Res Lett
44
45
46 3105 37:L22102. doi:10.1029/2010GL045416
47
48 3106
49
50
51 3107 Ponomarenko PV, Waters CL (2013) Transition of Pi2 ULF wave polarization structure from the
52
53 3108 ionosphere to the ground. Geophys Res Lett 40:1474-1478. doi:10.1002/grl50271
54
55
56 3109
57
58 3110 Ponomarenko P, Nishitani N, Oinats AV, Tsuya T, St.-Maurice J-P (2015) Application of ground
59
60
61
62
63
64
65

1
2
3
4 3111 scatter returns for calibration of HF interferometry data. Earth Planets Space 67:138. doi:
5
6
7 3112 10.1186/s40623-015-0310-3
8
9 3113
10
11 3114 Ponomarenko P, Iserhienrhien B, St.-Maurice JP (2016) Morphology and possible origins of near-
12
13 range oblique HF backscatter at high and midlatitudes. Radio Sci 51:718–730.
14 3115
15
16 3116 doi:10.1002/2016RS006088
17
18
19 3117
20
21 3118 Provan G, Yeoman TK, Milan SE (1998) CUTLASS Finland radar observations of the ionospheric
22
23 signatures of flux transfer events and the resulting plasma flow. Ann Geophys 16:1411
24 3119
25
26 3120
27
28
29 3121 Rae IJ, Donovan EF, Mann IR, Fenrich FR, Watt CEJ, Milling DK, Lester M, Lavraud B, Wild
30
31 3122 JA, Singer HJ, Reme H, Balogh A (2005) Evolution and characteristics of global Pc5 ULF waves
32
33 during a high solar wind speed interval. J Geophys Res 110:A12211. doi:10.1029/2005JA01107
34 3123
35
36 3124
37
38 3125 Ribeiro AJ, Ruohoniemi JM, Baker JBH, Clausen LBN, de Larquier S, Greenwald RA (2011) A
39
40 new approach for identifying ionospheric backscatter in midlatitude SuperDARN HF radar
41 3126
42 observations. Radio Sci 46:RS4011. doi:10.1029/2011RS004676
43 3127
44
45
46 3128
47
48 3129 Ribeiro AJ, Ruohoniemi JM, Baker JBH, Clausen LBN, Greenwald RA, Lester M (2012) A survey
49
50 of plasma irregularities as seen by the midlatitude Blackstone SuperDARN radar. J Geophys Res
51 3130
52 117: A02311. doi:10.1029/2011JA017207
53 3131
54

55 3132
56
57
58
59
60
61
62
63
64
65

1
2
3
4 3133 Rich FJ, Denig WF (1992) The major magnetic storm of March 13-14, 1989 and associated
5
6
7 3134 ionosphere effects. *Can. J. Phys.* 70:510
8
9
10 3135
11
12 3136 Ruohoniemi JM, Greenwald RA, Villain J-P, Baker KB, Newell PT, Meng C-I (1988) Coherent
13
14
15 3137 HF radar backscatter from small-scale irregularities in the dusk sector of the subauroral ionosphere.
16
17 3138 *J Geophys Res* 93(A11):12871–12882. doi:10.1029/JA093iA11p12871
18
19
20 3139
21
22 3140 Ruohoniemi JM, Greenwald RA (1996) Statistical patterns of high-latitude convection obtained
23
24
25 3141 from Goose Bay HF radar observations. *J Geophys Res* 101:21743-21763
26
27 3142
28
29 3143 Ruohoniemi JM, Greenwald RA (1998) The response of high-latitude convection to a sudden
30
31
32 3144 southward IMF turning. *Geophys Res Lett* 25:2913-2916
33
34 3145
35
36 3146 Ruohoniemi JM, Barnes RJ, Greenwald RA, Shepherd SG (2001) The response of the high-latitude
37
38
39 3147 ionosphere to the coronal mass ejection event of April 6, 2000: A practical demonstration of space
40
41
42 3148 weather nowcasting with the Super Dual Auroral Radar Network HF radars. *J Geophys Res Space*
43
44 3149 *Phys* 106:30085–30097. doi:10.1029/2000JA000217
45
46 3150
47
48
49 3151 Ruohoniemi, JM, Greenwald RA (2005) Dependencies of high-latitude plasma convection:
50
51 3152 Consideration of interplanetary magnetic field, seasonal, and universal time factors in statistical
52
53
54 3153 patterns. *J Geophys Res* 110:A09204. doi:10.1029/2004JA010815
55
56 3154
57
58
59
60
61
62
63
64
65

1
2
3
4 3155 Sakaguchi K, Nagatsuma T, Ogawa T, Obara T, Troshichev OA (2012) Ionospheric Pc5 plasma
5
6 3156 oscillations observed by the King Salmon HF radar and their comparison with geomagnetic
7
8
9 3157 pulsations on the ground and in geostationary orbit. J Geophys Res 117:A03218.
10
11
12 3158 doi:10.1029/2011JA016923
13
14 3159
15
16 3160 Samson JC, Greenwald RA, Ruohoniemi JM, Frey A, Baker KB (1990) Goose bay radar
17
18
19 3161 observations of earth-reflected, atmospheric gravity-waves in the high-latitude ionosphere. J
20
21 3162 Geophys Res 95(A6):7693–7709
22
23
24 3163
25
26 3164
27
28
29 3165 Scargle JD (1982) Studies in astronomical time series analysis. II -Statistical aspects of spectral
30
31 3166 analysis of unevenly spaced data. Astrophys J 263:835. doi:10.1086/160554
32
33
34 3167
35
36 3168 Senior C, Cerisier J-C, Thorolfsson A, Lester M (2002) Propagation in the ionosphere of
37
38 3169 convection changes following a sharp interplanetary magnetic field *By* transition. J Geophys Res
39
40
41 3170 107(A10):1316. doi:10.1029/2001JA005078
42
43 3171
44
45
46 3172 Shepherd SG (2014) Altitude-adjusted corrected geomagnetic coordinates: Definition and
47
48 3173 functional approximations. J Geophys Res Space Physics 119:7501–7521.
49
50
51 3174 doi:10.1002/2014JA020264
52
53 3175
54
55 3176 Shepherd SG (2017) Elevation angle determination for SuperDARN HF radar layouts. Radio
56
57
58 3177 Science 52:938–950. <https://doi.org/10.1002/2017RS006348>
59
60
61
62
63
64
65

1
2
3
4 3178
5
6
7 3179 Shepherd SG, Greenwald RA, Ruohoniemi JM (1999) A possible explanation for rapid large-scale
8
9 3180 ionospheric responses to southward turnings of IMF. *Geophys Res Lett* 26(20):3197-3200
10
11
12 3181
13
14 3182 Shi X, Baker JBH, Ruohoniemi JM, Hartinger MD, Frissell NA, Liu J (2017) Simultaneous space
15
16 3183 and ground-based observations of a plasmaspheric virtual resonance. *J Geophys Res* 122:4190-
17
18 4209. doi:10.1002/2016JA023583
19 3184
20
21 3185
22
23
24 3186 Shinagawa H, Iyemori T, Saito S, Maruyama T (2007) A numerical simulation of ionospheric and
25
26 3187 atmospheric variations associated with the Sumatra earthquake on December 26, 2004. *Earth*
27
28
29 3188 *Planets Space* 59:1015–1026 2007
30
31 3189
32
33
34 3190 Shiokawa K, Otsuka Y, Ogawa T, Balan N, Igarashi K, Ridley AJ, Knipp DJ, Saito A, Yumoto K
35
36 3191 (2002) A large-scale traveling ionospheric disturbance during the magnetic storm of 15 September
37
38 3192 1999. *J Geophys Res* 107(A6):1088. doi:10.1029/2001JA000245
39
40
41 3193
42
43 3194 Shiokawa K, Ihara C, Otsuka Y, Ogawa T (2003) Statistical study of nighttime medium-scale
44
45 3195 traveling ionospheric disturbances using midlatitude airglow images. *J Geophys Res*
46
47 108(A1):1052. doi:10.1029/2002JA009491
48 3196
49
50
51 3197
52
53 3198 Shiokawa K, Otsuka Y, Nishitani N, Ogawa T, Tsugawa T, Maruyama T, Smirnov SE, Bychkov
54
55 3199 VV, and Shevtsov BM (2008) Northeastward motion of nighttime MSTIDs at middle latitudes
56
57 3200 observed by an airglow imager. *J. Geophys. Res.* 113: A12312. doi:10.1029/2008JA013417
58
59
60
61
62
63
64
65

- 1
2
3
4 3201
5
6
7 3202 Southwood DJ, Wolf RA (1978) An assessment of the role of precipitation in magnetospheric
8
9 3203 convection. *J Geophys Res* 83:5227. doi:10.1029/JA083iA11p05227
10
11
12 3204
13
14 3205 Southwood DJ and Hughes WJ (1983) Theory of hydromagnetic waves in the magnetosphere.
15
16 3206 *Space Sci Rev* 35: 301. doi.org/10.1007/BF00169231
17
18
19 3207
20
21 3208 Spiro RW, Heelis RA, Hanson WB (1979) Rapid subauroral ion drifts observed by Atmosphere
22
23 3209 Explorer C. *Geophys Res Lett* 6:657–660. doi:10.1029/GL006i008p00657
24
25
26 3210
27
28
29 3211 Stocker AJ, Arnold NF, Jones TB (2000) The synthesis of travelling ionospheric disturbance (TID)
30
31 3212 signatures in HF radar observations using ray tracing. *Ann Geophys* 18:56-64.
32
33 3213 <https://doi.org/10.1007/s00585-000-0056-4>
34
35
36 3214
37
38 3215 Sutcliffe PR, Poole AWW (1989) Ionospheric Doppler and electron velocities in the presence of
39
40 3216 ULF waves. *J Geophys Res* 94:13505-13514. doi:10.1029/JA094iA10p13505
41
42
43 3217
44
45
46 3218 Suzuki S, Hosokawa K, Shibata T, Shiokawa K, Otsuka Y, Nishitani N, Ogawa T, Koustov AV,
47
48 3219 Shevtsov B (2009) Coordinated observations of nighttime medium-scale traveling ionospheric
49
50 3220 disturbances in 630-nm airglow and HF radar echoes at midlatitudes. *J Geophys Res* 114:A07312.
51
52
53 3221 doi:10.1029/2008JA013963
54
55
56 3222
57
58
59
60
61
62
63
64
65

- 1
2
3
4 3223 SuperDARN Data Analysis Working Group. Participating members: Thomas EG, Ponomarenko
5
6
7 3224 PV, Billett DD, Bland EC, Burrell AG, Kotyk K, Reimer AS, Schmidt M, Shepherd SG, Sterne
8
9 3225 KT, Walach M-T (2018) SuperDARN Radar Software Toolkit (RST) 4.2.
10
11
12 3226 doi:10.5281/zenodo.1403226.
13
14 3227
15
16 3228 Teramoto M, Nishitani N, Pilipenko V, Ogawa T, Shiokawa K, Nagatsuma T, Yoshikawa A,
17
18
19 3229 Baishev D, Murata KT (2014) Pi2 pulsation simultaneously observed in the *E* and *F* region
20
21 3230 ionosphere with the SuperDARN Hokkaido radar. J Geophys Res 119:3444-3462.
22
23
24 3231 doi:10.1002/2012JA018585
25
26 3232
27
28
29 3233 Teramoto M, Nishitani N, Nishimura Y, Nagatsuma T (2016) Latitudinal dependence on the
30
31 3234 frequency of Pi2 pulsations near the plasmopause using THEMIS satellites and Asian-Oceanian
32
33 3235 SuperDARN radars. Earth Planets Space 68:22-36. doi 10.1186/s40623-016-0397-1
34
35
36 3236
37
38 3237 Thébault E et al. (2015) International Geomagnetic Reference Field: the 12th generation. Earth,
39
40
41 3238 Planets and Space 67:79. doi.org/10.1186/s40623-015-0228-9
42
43 3239
44
45
46 3240 Thomas RM, Whitham PS, and Elford WG (1986) Frequency dependence of radar meteor echo
47
48 3241 rates. Proceedings of Astronomical Society of Australia, 6, 303-306
49
50
51 3242
52
53 3243 Thomas EG, Baker JBH, Ruohoniemi JM, Clausen LBN, Coster AJ, Foster JC, Erickson PJ (2013)
54
55 3244 Direct observations of the role of convection electric field in the formation of a polar tongue of
56
57
58
59
60
61
62
63
64
65

1
2
3
4 3245 ionization from storm enhanced density. J Geophys Res Space Phys 118:1180–1189.
5
6 3246 doi:10.1002/jgra.50116
7
8
9 3247
10
11 3248 Thomas EG, Shepherd SG (2018) Statistical patterns of ionospheric convection derived from mid-
12
13 latitude, high-latitude, and polar SuperDARN HF radar observations. J. Geophys. Res. 123:3196-
14 3249 3216. <https://doi.org/10.1002/2018JA025280>
15
16 3250
17
18
19 3251
20
21 3252 Thorolfsson A, Cerisier J-C, Pinnock M (2001) Flow transients in the postnoon ionosphere: The
22
23 role of solar wind dynamic pressure. J Geophys Res 106(A2):1887–1901.
24 3253 doi:10.1029/2000JA900078
25
26 3254
27
28
29 3255
30
31 3256 Tsuda T, Yamamoto M, Hashiguchi H, Shiokawa K, Ogawa Y, Nozawa S, Miyaoka H, Yoshikawa
32
33 A (2016) A proposal on the study of solar-terrestrial coupling processes with atmospheric radars
34 3257 and ground-based observation network Radio Sci 51:1587–1599. doi:10.1002/2016RS006035
35
36 3258
37
38 3259
39
40
41 3260 Tsugawa T, Saito A, Otsuka Y, Yamamoto M (2003) Damping of large-scale traveling ionospheric
42
43 3261 disturbances detected with GPS networks during the geomagnetic storm. J Geophys Res 108(A3):
44
45 1127. doi:10.1029/2002JA009433
46 3262
47
48 3263
49
50
51 3264 Tsugawa T, Saito A, Otsuka Y (2004) A statistical study of large-scale traveling ionospheric
52
53 3265 disturbances using the GPS network in Japan. J Geophys Res 109:A06302.
54
55 3266 doi:10.1029/2003JA010302
56
57
58 3267
59
60
61
62
63
64
65

- 1
2
3
4 3268 Unwin RS, Cummack CH (1980) Drift spikes: The ionospheric signature of large poleward
5
6
7 3269 directed electric fields at subauroral latitudes, IMS in Antarctica. Mem Natl Inst Polar Res 16:72–
8
9 3270 83
10
11
12 3271
13
14 3272 Watanabe D, Nishitani N (2013) Study of ionospheric disturbances during solar flare events using
15
16 3273 the SuperDARN Hokkaido radar. Adv Polar Sci 24:12-18. doi:10.3724/SP.J.1085.2013.00012
17
18
19 3274
20
21 3275 Wild J (2012) Public Engagement with SuperDARN. SuperDARN Workshop 2012, Shanghai,
22
23
24 3276 China
25
26
27 3277
28
29 3278 Wild JA, Cowley SWH, Davies JA, Khan H, Lester M, Milan SE, Provan G, Yeoman TK, Balogh
30
31
32 3279 A, Dunlop MW, Fornaçon K-H, Georgescu E (2001) First simultaneous observations of flux
33
34 3280 transfer events at the high-latitude magnetopause by the Cluster spacecraft and pulsed radar
35
36
37 3281 signatures in the conjugate ionosphere by the CUTLASS and EISCAT radars. Ann Geophys
38
39 3282 18:1491 – 1508
40
41
42 3283
43
44 3284 Wild JA, Milan SE, Cowley SWH, Dunlop MW, Owen CJ, Bosqued JM, M. G. G. T. Taylor GT,
45
46 3285 Davies JA, Lester M, Sato N, Yukimatu AS, Fazakerley AN, Balogh A, Rème H (2003)
47
48
49 3286 Coordinated interhemispheric SuperDARN radar observations of the ionospheric response to flux
50
51 3287 transfer events observed by the Cluster spacecraft at the high-latitude magnetopause. Ann Geophys
52
53
54 3288 21: 1807 – 1826. <https://doi.org/10.5194/angeo-21-1807-200>
55
56 3289
57
58
59
60
61
62
63
64
65

1
2
3
4 3290 Wolf RA, Spiro RW, Sazykin S, Toffoletto FR (2007) How the Earth's inner magnetosphere
5
6
7 3291 works: An evolving picture. *J. Atmos. Solar-Terr. Phys.* 69: 288–302
8
9 3292
10
11 3293 Yakymenko, KN, Koustov AV, Nishitani N (2015) Statistical study of midlatitude E region echoes
12
13
14 3294 observed by the Hokkaido SuperDARN HF radar. *J Geophys Res* 120:9959-9976.
15
16 3295 doi:10.1002/2015JA021685
17
18
19 3296
20
21 3297 Yeh H-C, Foster JC, Rich FJ, Swider W (1991) Storm time electric field penetration observed at
22
23
24 3298 mid-latitude. *J Geophys Res* 96:5707. doi:10.1029/90JA02751
25
26 3299
27
28
29 3300 Yokoyama T, Hysell DL (2010) A new midlatitude ionosphere electrodynamic coupling model
30
31 3301 (MIECO): Latitudinal dependence and propagation of medium-scale traveling ionospheric
32
33
34 3302 disturbances. *Geophys Res Lett* 37:L08105. doi:10.1029/2010GL042598
35
36 3303
37
38 3304 Yeoman TK, Wright DM, Robinson TR, Davies JA, Rietveld M (1997) High spatial and temporal
39
40
41 3305 resolution observations of an impulse driven field line resonance in radar backscatter artificially
42
43 3306 generated with the Tromso heater. *Ann Geophys* 15:634-644. doi:10.1007/s00585-997-0634-9
44
45
46 3307
47
48 3308 Zou S, Lyons LR, Nicolls MJ, Heinselman CJ, Mende SB (2009) Nightside ionospheric
49
50
51 3309 electrodynamic associated with substorms: PFISR and THEMIS ASI observations. *J Geophys*
52
53 3310 *Res* 114:A12301. doi:10.1029/2009JA014259
54
55 3311
56
57
58 3312 Zou Y, Nishitani N (2014) Study of midlatitude ionospheric convection during quiet
59
60
61
62
63
64
65

1
2
3
4
5
6
7
8
9
10
11
12
13
14
15
16
17
18
19
20
21
22
23
24
25
26
27
28
29
30
31
32
33
34
35
36
37
38
39
40
41
42
43
44
45
46
47
48
49
50
51
52
53
54
55
56
57
58
59
60
61
62
63
64
65

3313 and disturbed periods using the SuperDARN Hokkaido radar. Adv Space Res
3314 54:473-480 <http://dx.doi.org/10.1016/j.asr.2014.01.011>

3315

[Click here to view linked References](#)

1
2 3316 **Figure captions**
3
4 3317 **Fig. 1.** Fields of view of the SuperDARN radars in the a) northern and b) southern
5
6 3318 hemispheres.
7
8
9 3319
10
11 3320 **Fig. 2.** Photo of the Fort Hays East and West radar antennas and radar equipment shelter.
12
13 3321
14
15
16 3322 **Fig. 3.** Ray-tracing results for 11 MHz transmissions on beam 12 of the Blackstone radar
17
18 3323 propagating through the predicted IRI-2011 ionosphere on 18 November 2010 at 14:00
19
20 3324 UT (see text for details). Reproduced from Fig. 3 of de Larquier et al. (2013)
21
22 3325
23
24
25 3326 **Fig. 4.** A plot of Doppler velocity against radar beam and range from CVE and CVW
26
27 3327 radars. This figure shows Doppler velocity observations (positive toward the radar) for
28
29 3328 one scan of data from CVW and CVE and indicates 4 separate regions of ionospheric
30
31 3329 scatter indicated by the number I - meteor scatter, II – low velocity ionospheric scatter
32
33 3330 from the sub auroral region, III – scatter from a SAPS, and IV- low velocity ionospheric
34
35 3331 scatter from the auroral regions. Reproduced from Fig. 2 of Clausen et al. (2012).
36
37 3332
38
39
40 3333 **Fig. 5.** Schematic plots showing the (a) northern and (b) southern hemisphere
41
42 3334 SuperDARN radar locations with respect to the auroral oval. The auroral oval (yellow)
43
44 3335 for moderately disturbed conditions, as quantified by Holzworth and Meng (1975), is
45
46 3336 plotted as a function of AACGM coordinates with the SuperDARN radar locations
47
48 3337 identified in green type and green closed circles (polar cap latitudes), blue type and blue
49
50 3338 closed circles (auroral latitudes) and black type and red closed circles (mid-latitude
51
52 3339 radars).
53
54
55
56
57
58
59
60
61
62
63
64
65

1
2
3
4
5
6
7
8
9
10
11
12
13
14
15
16
17
18
19
20
21
22
23
24
25
26
27
28
29
30
31
32
33
34
35
36
37
38
39
40
41
42
43
44
45
46
47
48
49
50
51
52
53
54
55
56
57
58
59
60
61
62
63
64
65

3340
3341
3342
3343
3344
3345
3346
3347
3348
3349
3350
3351
3352
3353
3354
3355
3356
3357
3358
3359
3360
3361
3362

Fig. 6. Timeline of the SuperDARN radars in the a) northern and b) southern hemispheres. The geomagnetic latitudes are in AACGM-v2 coordinates, changing as a function of time.

Fig. 7. Schematic illustration of natural phenomena which can be studied by SuperDARN radars.

Fig. 8. (a-d) GPS TEC maps depicting evolution of the polar tongue of ionization (TOI) with SuperDARN convection patterns overlaid. (e-h) SuperDARN LOS velocity measurements from radars located at mid-latitudes on the dayside and extending into the polar cap. Reproduced from Fig. 7 of Thomas et al. (2013)

Fig. 9. Average patterns of Northern Hemisphere ionospheric convection calculated from SuperDARN data collected during periods of increased geomagnetic activity ($Kp \geq 3$) between June 2005 and April 2006. Contours of the global solution of electrostatic potential are shown as black lines spaced every 4 kV. Adapted from Fig. 12 of Baker et al. (2007)

Fig. 10. CVW velocity in beam 4 on 17 March 2013, 0930-1430 UT. The green cells refer to the SAPS region. The two vertical white lines mark the period of narrow and intense SAID feature. The period of strong SAPS Wavy Structure (SAPSWS) activity is near 1215 UT. Reproduced from Fig. 2(a) of Makarevich and Bristow (2014)

1
2 3363 **Fig. 11.** LOS Doppler velocity for a 1-minute scan of WAL showing a strong sub-auroral
3
4 3364 westward flow channel. Overlaid is a swath of the 135.6 nm aurora from TIMED GUVI,
5
6
7 3365 cross-track drift velocity from the DMSP F15 spacecraft and the track of the NOAA-18
8
9 3366 spacecraft, which are used to determine the equatorward edge of electron precipitation
10
11 3367 (shown as a thick dotted line). Adapted from Fig. 1 of Oksavik et al. (2006)
12
13
14
15 3368

16
17 3369 **Fig. 12.** (top/left) spatial distribution of GPS TEC with precipitating electron flux along
18
19 3370 a pass of NOAA/POES satellite. (bottom/left) 2-D map of LOS velocities observed by
20
21 3371 mid-latitude SuperDARN radars over North America at 0840 UT on 9 April 2011. (right)
22
23 3372 Vector representation of the average large-scale SAPS flow direction and the inferred
24
25 3373 SAPS speed identified by the three radar pairs. Time runs along the y axis, increasing
26
27 3374 toward the bottom. Adapted from Figs. 5 and 7 of Clausen et al. (2012)
28
29
30
31

32 3375
33
34 3376 **Fig. 13.** Conjugate radar observations of a SAPS flow channel for two different periods
35
36 3377 showing excellent agreement in the latitude of the channel between BKS and FIR.
37
38 3378 Reproduced from Fig. 6 of Grocott et al. (2011)
39
40
41

42 3379
43
44 3380 **Fig. 14.** Range-Time-Parameter plots of the Doppler velocities observed by beam 7 of
45
46 3381 the Hokkaido East radar (top panel) and calculated using the CRCM numerical simulation
47
48 3382 with the plasma sheet boundary conditions determined by the LANL particle data (middle
49
50 3383 panel) and with fixed boundary condition (bottom panel). Reproduced from Fig. 5 of
51
52 3384 Ebihara et al. (2009)
53
54
55
56

57 3385
58
59
60
61
62
63
64
65

1
2 3386 **Fig. 15.** (a) CVW velocity versus universal time (UT) and magnetic latitude (MLAT) on
3
4 3387 17 March 2013 between 1150 and 1340 UT and slant ranges 1035–1665 km. The
5
6 3388 propagation of SAPS Wavy Structure (SAPSWS) 1–4 is shown by yellow lines. The
7
8 3389 range coincident with Ionospheric Pierce Point (IPP) at 450 km between PRN 21 and
9
10 3390 Beaver Cove (BCOV) is shown by the pink line. (b) CVW velocity at IPP. The four
11
12 3391 periods with velocities < -500 m/s are highlighted. (c) GPS TEC measurements at IPP.
13
14 3392 (d) Wavelet spectrum of CVW velocity at IPP. (e) Wavelet spectrum of GPS TEC. The
15
16 3393 colored dots show the three highest peaks for each spectrum. Reproduced from Fig. 3 of
17
18 3394 Makarevich and Bristow (2014)

19
20 3395
21
22 3396 **Fig. 16.** The occurrence rate (%) of ionospheric echoes from beam 4 of TIG detected
23
24 3397 during all seasons, and sorted according to geomagnetic activity $Kp > 1$ to 2; $Kp > 3$ to 4
25
26 3398 and $Kp > 5$ to 6. Model auroral oval boundaries are superimposed for $AL = -64$ nT ($Kp =$
27
28 3399 $2-$), $AL = -240$ nT ($Kp = 4-$), and $AL = -458$ nT ($Kp = 6-$). Adapted from Fig. 5 of
29
30 3400 Parkinson et al. (2003b)

31
32 3401
33
34 3402 **Fig. 17.** The association of quiet-time subauroral irregularities with gradients in
35
36 3403 ionospheric electron density and temperature. The top panel shows time series of the
37
38 3404 electron density and electron temperature gradients measured by the Millstone Hill
39
40 3405 incoherent scatter radar. The pink triangle marks the time that the gradient in electron
41
42 3406 temperature reversed from poleward to equatorward, establishing favorable conditions
43
44 3407 for the TGI. The bottom panel shows a time series of backscatter power from one beam
45
46 3408 of the Wallops radar and the increase in backscatter power that followed the reversal.

1
2 3409 Reproduced from Fig. 1 of Greenwald et al. (2006)

3
4
5
6 3410

7
8
9 3411 **Fig. 18.** Observations of the altitude of the irregularities associated with SAIS from beam
10
11 3412 12 of the Blackstone radar near local midnight on 18 November 2010. The two solid
12
13 3413 curves mark the region where the magnetic aspect angle is within 1° of perpendicularity.

14
15
16 3414 Reproduced from Fig. 7 of de Larquier et al. (2013)

17
18
19
20 3415

21
22 3416 **Fig. 19.** Daytime TIG echo occurrence versus Pedersen conductance from the IRI model.

23
24
25 3417 Each point is color-coded according to the corresponding value of the F region peak
26
27 3418 density $NmF2$, with the scale shown on the right. Reproduced from Fig. 5 of Kane et al.
28
29 3419 (2012)

30
31
32 3420

33
34 3421 **Fig. 20.** Keograms from the Hokkaido radar of (a) radar echo power on beam 15 and
35
36 3422 airglow intensity deviation and (b) Doppler velocity and (c) airglow intensity deviation
37
38 3423 on beam 15 and 10 on 11 June 2007. Trace velocities indicated by red lines with numbers
39
40 3424 1-4 and number 5 are 120 and 90 m/s, respectively, and those indicated by black lines
41
42 3425 with numbers 1-4 and number 5 are 240 and 180 m/s, respectively. Reproduced from Fig.
43
44 3426 12 of Ogawa et al. (2009)

45
46
47
48
49 3427

50
51 3428 **Fig. 21.** Schematic interpretation of the optical and radar events observed on 8 December
52
53 3429 2007 by the Hokkaido radar. The dark grey and light gray shaded regions represent the
54
55 3430 depletions and enhancements, respectively in the 630-nm airglow intensity. Reproduced
56
57 3431 from Fig. 4 of Suzuki et al. (2009)

58
59
60
61 178

62
63
64
65

1
2
3
4
5
6
7
8
9
10
11
12
13
14
15
16
17
18
19
20
21
22
23
24
25
26
27
28
29
30
31
32
33
34
35
36
37
38
39
40
41
42
43
44
45
46
47
48
49
50
51
52
53
54
55
56
57
58
59
60
61
62
63
64
65

3432

3433 **Fig. 22.** Classification of LOS Doppler velocities from beam-7 of the Blackstone radar
3434 on 15 January 2010 according to: (a) the traditional point-by-point threshold method (top),
3435 and (b) the new clustering method (bottom). Ionospheric scatter is colored according to
3436 the scale at right while ground scatter is shaded gray. Reproduced from Fig. 3 of Ribeiro
3437 et al. (2011)

3438

3439 **Fig. 23.** Observations of the mid-latitude evening anomaly on 13 August 2010 seen in:
3440 (a) Blackstone radar beam-7 backscattered power, and (b) Millstone Hill ISR electron
3441 density versus altitude. Dashed lines identify solar noon and sunset. Reproduced from Fig.
3442 5 of de Larquier et al. (2011)

3443

3444 **Fig. 24.** Diurnal variation of f_oF2 for 12-13 September 2010 calculated from Bruny Island
3445 radar data (black), Unwin radar data (red), and Macquarie Island ionosonde (blue).
3446 Reproduced from Fig. 4 of Bland et al. (2014)

3447

3448 **Fig. 25.** Range-time maps of elevation angle for beam 7 of the HOK data at 06-12 UT on
3449 23 February 2014 for: (a) uncalibrated (top), and (b) calibrated data (bottom). Adapted
3450 from Fig. 6 of Ponomarenko et al. (2015)

3451

3452 **Fig. 26.** Ray-tracing analysis (solid curves) and expected locations for ionospheric
3453 irregularity backscatter occurrence (asterisks) for HOK during nighttime quiet
3454 geomagnetic conditions and transmission frequencies of (top to bottom) 9, 11, and 13

1
2 3455 MHz, respectively. Adapted from Fig. 3 of Nishitani and Ogawa (2015)
3
4
5 3456
6
7 3457 **Fig. 27.** (a) Model ray paths of HF radar propagation through an ionosphere modulated
8
9 3458 by a TID. Focusing and defocusing at the ground is caused by the uneven contours of
10
11 3459 electron density (adapted from Samson et al. (1990)). (b) Example of FIR radar ground
12
13 3460 scatter data received along a single beam, versus ground range and universal time,
14
15 3461 showing several signatures of TID moving toward the radar. Reproduced from Fig. 2 of
16
17 3462 Grocott et al. (2013)
18
19
20
21 3463
22
23
24 3464 **Fig. 28.** LSTID signatures observed simultaneously by HOK and GEONET GPS receiver
25
26 3465 network on 15 December 2006. (a) Doppler velocity of GS echoes measured by HOK,
27
28 3466 and (b) GEONET-GPS total electron content (TEC) perturbations (sampled along the
29
30 3467 direction of HOK beam 0 at lower latitudes) plotted as a function of UT and geographic
31
32 3468 latitude. In panel (b), the TEC perturbation values were obtained by subtracting 60-min
33
34 3469 running average. Three major disturbances are visible in each map, denoted as events 1–
35
36 3470 3. Reproduced from Fig. 5 of Hayashi et al. (2010)
37
38
39
40
41 3471
42
43 3472 **Fig. 29.** Modeled rates of anti-wind MSTID direction occurrence versus local time based
44
45 3473 on the HWM07 neutral wind model (Drob et al. 2008) applied to the center of the HOK
46
47 3474 FOV. Contours are MSTID occurrence rates according to the HOK observations of
48
49 3475 ground scatter from the *E* region. (b) the same as (a) but for ground scatter from the *F*
50
51 3476 region. Blue, red and magenta contours are for the rates of 3, 5 and 10%, respectively.
52
53
54 3477 Adapted from Fig. 3 of Oinats et al. (2016a)
55
56
57
58 3478
59
60
61
62
63
64
65

1
2 3479 **Fig. 30.** Time series of North American SuperDARN MSTID, polar vortex, and
3
4 3480 geomagnetic activity indices for the 2012–2013 observational season. (a) Continental
5
6 3481 MSTID index (gray and blue traces) and daily number of good sampling windows (dotted
7
8 3482 line). Background color indicates daily MSTID score and classification, with MSTID-
9
10 3483 active days in reds and MSTID-quiet days in blues. (b) Polar Vortex Index. (c) Negative
11
12 3484 *AE* index. (d) *SYM-H* index. In all panels, gray traces show raw data while blue traces
13
14 3485 show a 4-day running mean smoothing. Adapted from Fig. 8 of Frissell et al. (2016)
15
16
17
18
19
20

21 3486
22 3487 **Fig. 31.** Doppler velocity of HOK echoes on beam 4 (echo power >10 dB) versus
23
24 3488 Japanese Standard Time (JST) after an earthquake on 11 March 2011. Sloped lines mark
25
26 3489 several individual echo bands propagating northward away from the earthquake epicenter.
27
28 3490 Measurements at 900–1100 km range (dashed rectangles) are 2-hop signals while their 1-
29
30 3491 hop counterparts are identified by solid rectangles at 350–500 km range. Reproduced
31
32 3492 from Fig. 5 of Ogawa et al. (2012)
33
34
35

36 3493
37
38 3494 **Fig. 32.** SuperDARN ionospheric convection maps during the (a, b) main and (c) recovery
39
40 3495 phases of a geomagnetic storm on 2 October 2013, with fitted vectors in locations where
41
42 3496 measurements were obtained (color coded according to the scale at right) and superposed
43
44 3497 neutral wind velocity (black vector) measured at the Illinois (UAO) and Michigan (ANN)
45
46 3498 FPI sites. Locations of the mid-latitude SuperDARN radars operational at this time are
47
48 3499 identified. Adapted from Figs. 4 and 7 of Joshi et al. (2015)
49
50
51
52

53 3500
54
55 3501 **Fig. 33.** The BKS LOS velocity as a function of latitude and time. The BKS data along
56
57 3502 beam 7 are averaged over 3 range gates and plotted as a function of UT for 5 sets of gates
58
59
60

1
2 3503 covering the latitude range of 53.9° N □to 57.1° N. Panel b shows the difference between
3
4 3504 the first part of each of the first two cycles and the second part. Reproduced from Fig. 3
5
6
7 3505 of Frissell et al. (2011)

8
9 3506
10
11 3507 **Fig. 34.** The FHE beam 10 LOS velocity as a function of time and results of a spectral
12
13 analysis. Panel a shows the FHE beam 10 LOS velocity as a function of time for a number
14 3508 of different range gates. Panel b shows the relative phase from the spectral analysis as a
15
16 3509 function of latitude while Panel c shows the amplitude from the spectral analysis. Note
17
18 3510 the red dashed line in panel b which gives the estimated position of the plasmopause.
19
20 3511 Reproduced from Fig. 12 of Shi et al. (2017).
21
22 3512

23
24 3513
25
26 3514 **Fig. 35.** A comparison of magnetometer data from Ottawa with WAL LOS velocity.
27
28 3515 Panel a shows the dynamic spectrum of the X component data from the Ottawa
29
30 3516 magnetometer for the interval 0604 to 0611 UT on 1 August 2007. The contours represent
31
32 3517 different levels of power with the lighter colors the higher power. Panel b shows the high
33
34 3518 time resolution estimates of the LOS velocity from WAL for the same period. Panel c
35
36 3519 shows the shorter interval marked by vertical dashed lines in panel c. Reproduced from
37
38 3520 Fig. 3 of Greenwald et al. (2008)

39
40 3521
41
42 3522 **Fig. 36.** LOS velocity data from beam 4 of TIG as a function of range and UT. One hour
43
44 3523 of LOS velocity data is presented from 2000 to 2100 UT on 28 September 2000. The
45
46 3524 grey scale, which saturates at + 50 m/s and -50 m/s demonstrates the ability of this
47
48 3525 technique to visualize MHD waves in the data Note also the band of scatter between
49
50 3526 range gates 20 and 40 (which is probably ground scatter) shows no evidence of the MHD

1
2
3
4
5
6
7
8
9
10
11
12
13
14
15
16
17
18
19
20
21
22
23
24
25
26
27
28
29
30
31
32
33
34
35
36
37
38
39
40
41
42
43
44
45
46
47
48
49
50
51
52
53
54
55
56
57
58
59
60
61
62
63
64
65

3527 wave on this occasion. Adapted from Fig. 4 of Ponomarenko et al. (2005)

3528

3529 **Fig. 37.** A histogram of significant frequencies in the TIG data set. A three- point
3530 smoothing is applied to the data and is shown by the curve with the slightly darker black
3531 line superimposed on the histogram. The vertical lines identify peaks of the smoothed
3532 curve showing certain frequencies at 1.3, 1.6, 2.1, 2.9, and 3.3 mHz which appear to have
3533 higher spectral power than the neighboring frequencies. The frequency resolution is 0.1
3534 mHz. Reproduced from Fig. 7 of Norouzi-Sedeh et al. (2015)

3535

Table 1. List of SuperDARN radars. Magnetic latitudes / longitudes are in AACGM-v2 coordinates to one decimal point accuracy for 1 January 2018.

Northern hemisphere

Radar Name	Country	Geo. Lat.	Geo. Lon.	Boresite	Mag. Lat.	Mag. Lon.	Year	Code
Adak Island East	USA	51.9	-176.6	46.0	47.3	-111.1	2012	ADE
Adak Island West	USA	51.9	-176.6	-28.0	47.3	-111.1	2012	ADW
Blackstone	USA	37.1	-78.0	-40.0	46.4	-0.7	2008	BKS
Christmas Valley East	USA	43.3	-120.4	54.0	48.7	-56.2	2010	CVE
Christmas Valley West	USA	43.3	-120.4	-20.0	48.7	-56.2	2010	CVW
Clyde River	Canada	70.5	-68.5	-55.6	77.4	18.4	2012	CLY
Fort Hays East	USA	38.9	-99.4	45.0	47.9	-30.1	2009	FHE
Fort Hays West	USA	38.9	-99.4	-25.0	47.9	-30.1	2009	FHW
Goose Bay	USA	53.3	-60.5	5.0	59.4	23.8	1983	GBR
Hankasalmi	UK	62.3	26.6	-12.0	58.9	103.8	1995	HAN
Hokkaido East	Japan	43.5	143.6	30.0	36.9	-143.2	2006	HOK
Hokkaido West	Japan	43.5	143.6	-30.0	36.9	-143.2	2014	HKW
Inuvik	Canada	68.4	-133.8	29.5	71.1	-81.1	2008	INV
Kapuskasings	USA	49.4	-82.3	-12.0	58.7	-6.2	1993	KAP
King Salmon	Japan	58.7	-156.7	-20.0	57.1	-96.6	2001	KSR
Kodiak	USA	57.6	-152.2	30.0	56.8	-92.3	2000	KOD
Longyearbyen	Norway	78.2	16.1	23.7	75.5	108.5	2016	LYR
Prince George	Canada	54.0	-122.6	-5.0	59.0	-61.6	2000	PGR
Pykkvibaer	UK	63.8	-20.5	30.0	63.5	66.0	1995	PYK

Rankin Inlet	Canada	62.8	-92.1	5.7	71.5	-21.7	2007	RKN
Saskatoon	Canada	52.2	-106.5	23.1	60.0	-41.2	1993	SAS
Stokkseyri	UK	63.9	-21.0	-59.0	63.7	65.7	1994	STO
Wallops Island	USA	37.9	-75.5	35.9	46.9	2.7	2005	WAL

8 Southern hemisphere

9

Radar Name	Country	Geo. Lat.	Geo. Lon.	Boresite	Mag. Lat.	Mag. Lon.	Year	Code
Buckland Park	Australia	-34.6	138.5	146.5	-45.3	-145.2	2014	BPK
Dome C East	Italy	-75.1	123.4	115.0	-89.0	56.9	2012	DCE
Falkland Islands	UK	-51.8	-59.0	178.3	-39.3	10.2	2010	FIR
Halley	UK	-75.5	-26.6	165.0	-62.2	30.3	1988	HAL
Kerguelen	France	-49.4	70.3	168.0	-58.5	124.5	2000	KER
McMurdo	USA	-77.9	166.7	263.4	-79.9	-32.8	2010	MCM
SANAE	South Africa	-71.7	-2.9	173.2	-61.9	45.1	1997	SAN
South Pole	USA	-90.0	118.3	75.7	-74.3	19.2	2013	SPS
Syowa East	Japan	-69.0	39.6	106.5	-66.5	73.6	1997	SYE
Syowa South	Japan	-69.0	39.6	165.0	-66.5	73.6	1995	SYS
TIGER Bruny Island	Australia	-43.4	147.2	180.0	-54.0	-132.3	1999	TIG
TIGER Unwin	Australia	-46.5	168.4	227.9	-53.8	-105.2	2004	UNW
Zhongshan	China	-69.4	76.4	72.5	-74.9	99.0	2010	ZHO

10

11

12

13

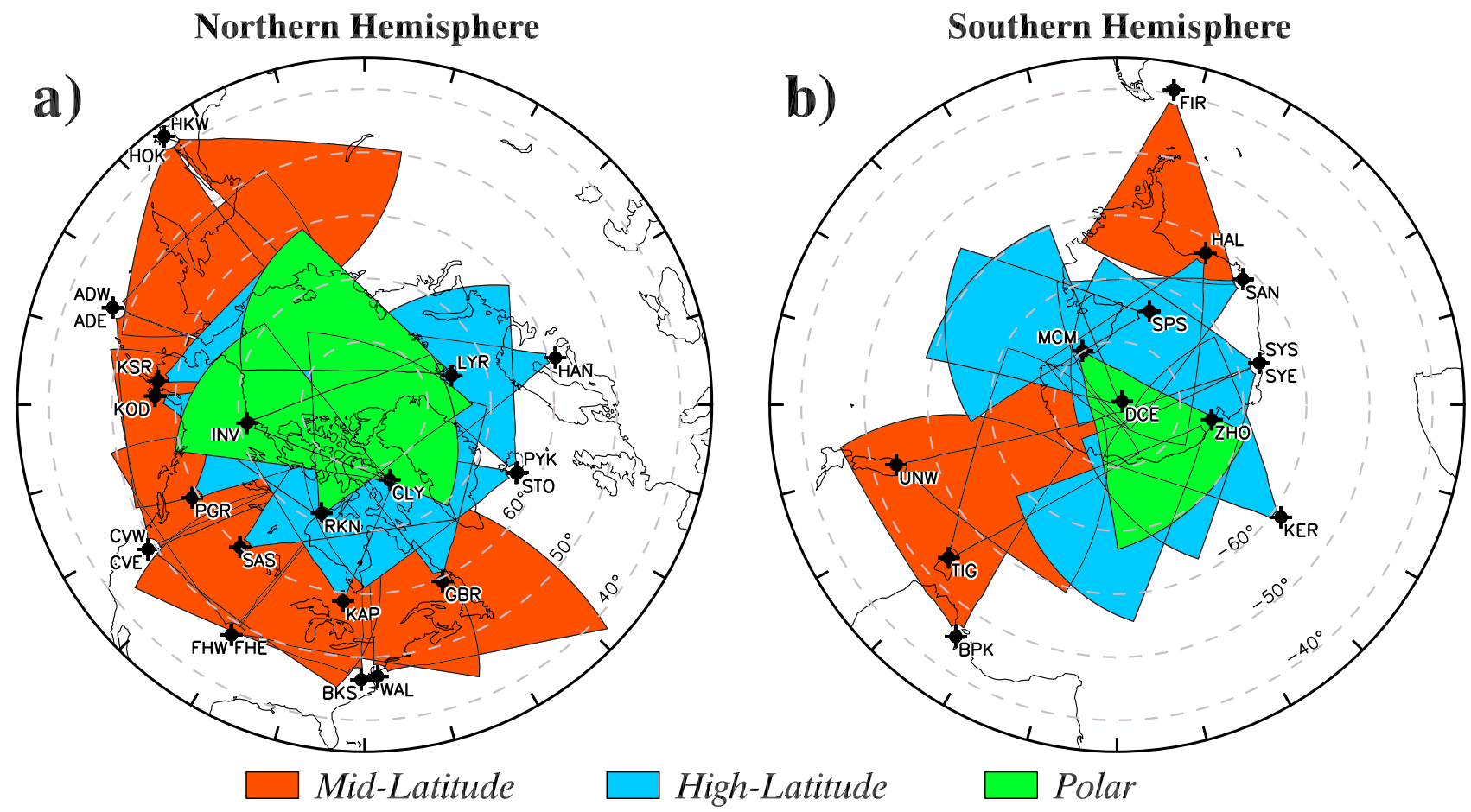
14

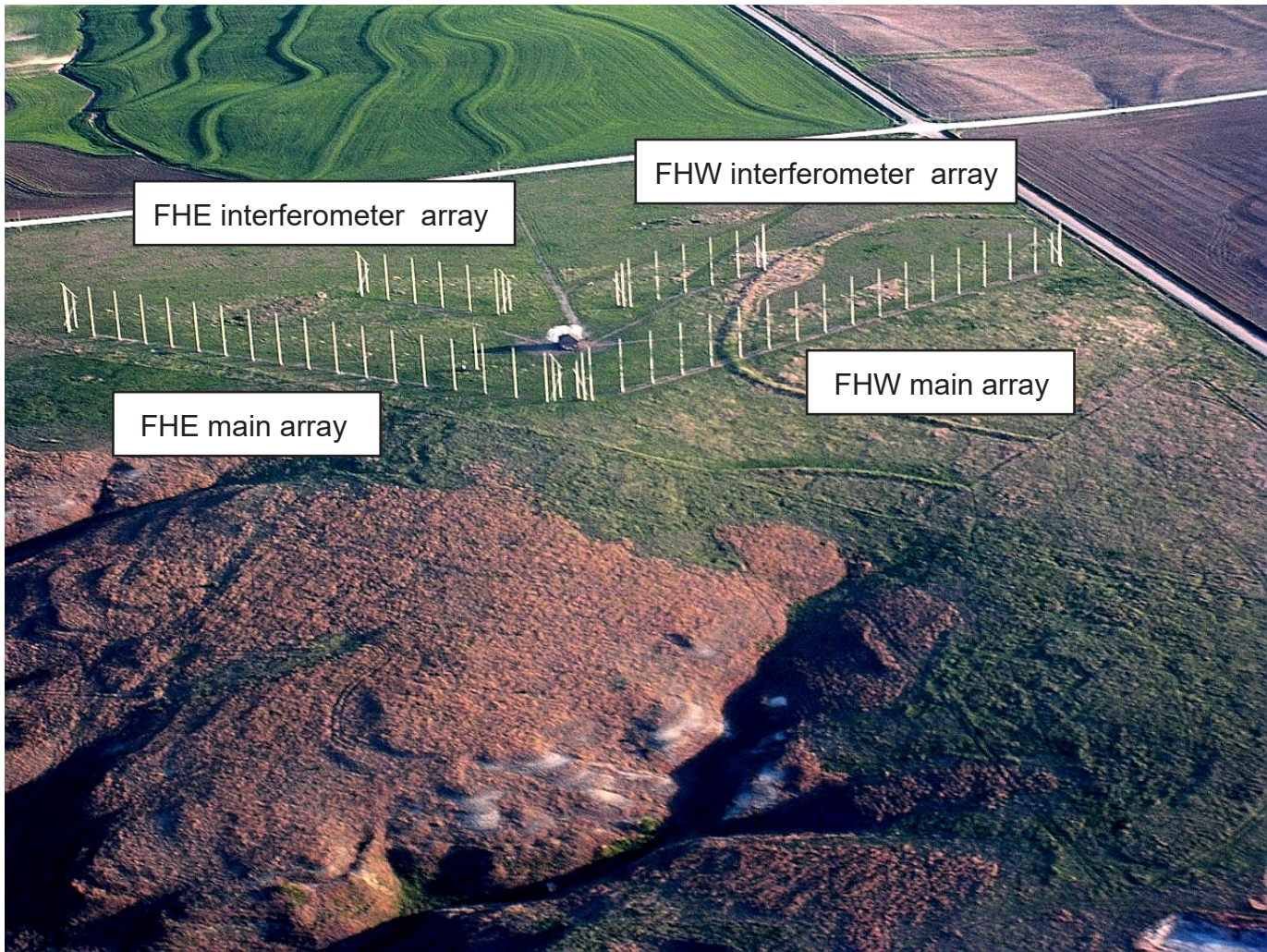
15

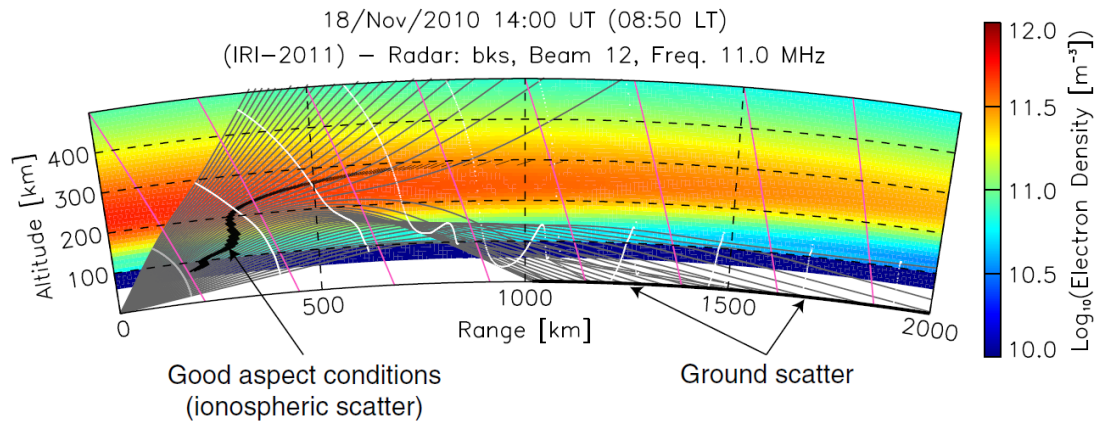
16

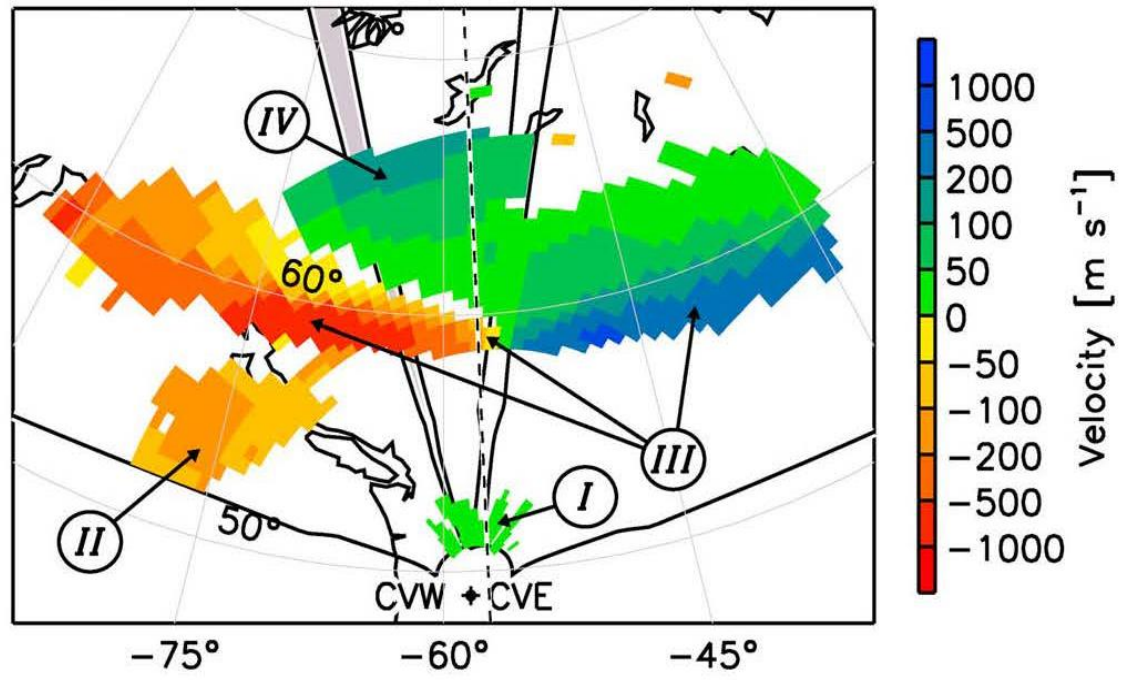
Table 2. Categories of Mid-latitude Irregularities with respect to the Equatorward Precipitation Boundary (EPB).

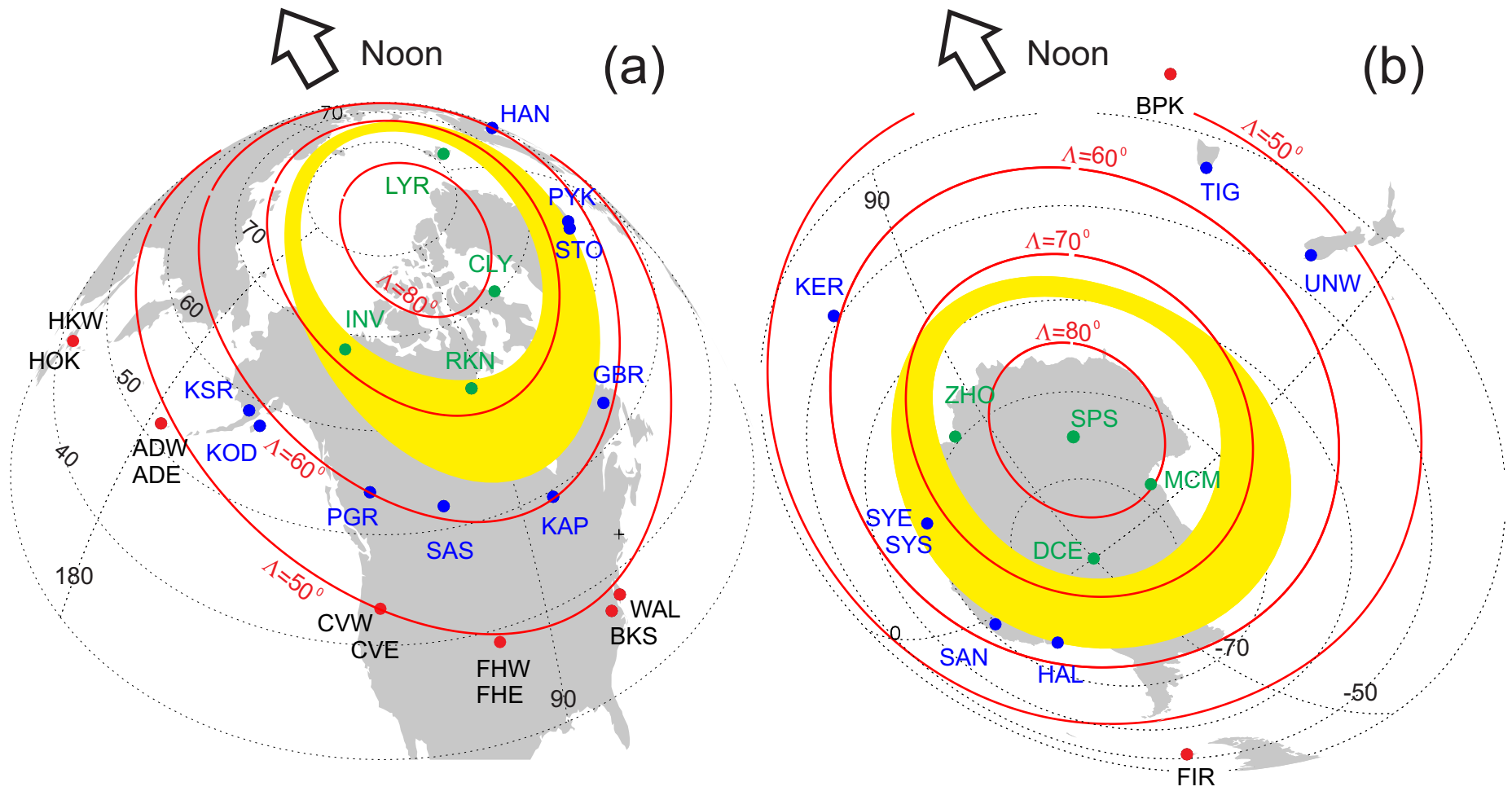
	Location in relation to the EPB	Occurrence /Properties
Auroral irregularities	Poleward of the EPB	Observed at nearer ranges during storms, high-speed (~100s m/s) flow
SAPS irregularities	On the equatorward side of the EPB and usually extending only a few degrees in latitude	Occurrence increases with disturbance level; westward, high-speed flow (~ 100 m/s) in the premidnight sector
Subauroral irregularities	Extending equatorward of the EPB indefinitely	Nightside, low-speed (~10s m/s) flow, predominantly westward
Temperate mid-latitude irregularities	Equatorward of the EPB by more than 10°	Strong association with MSTIDs

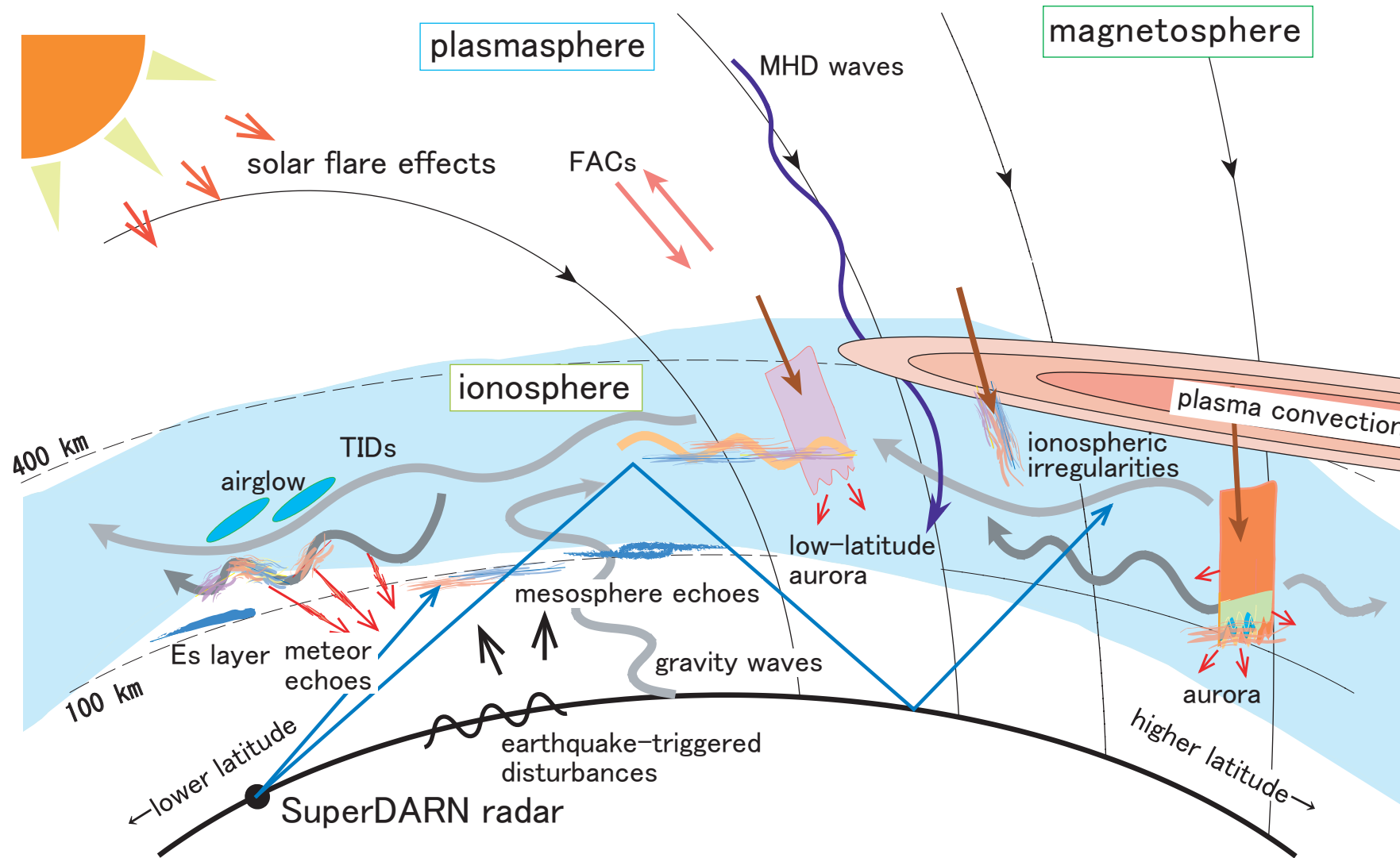


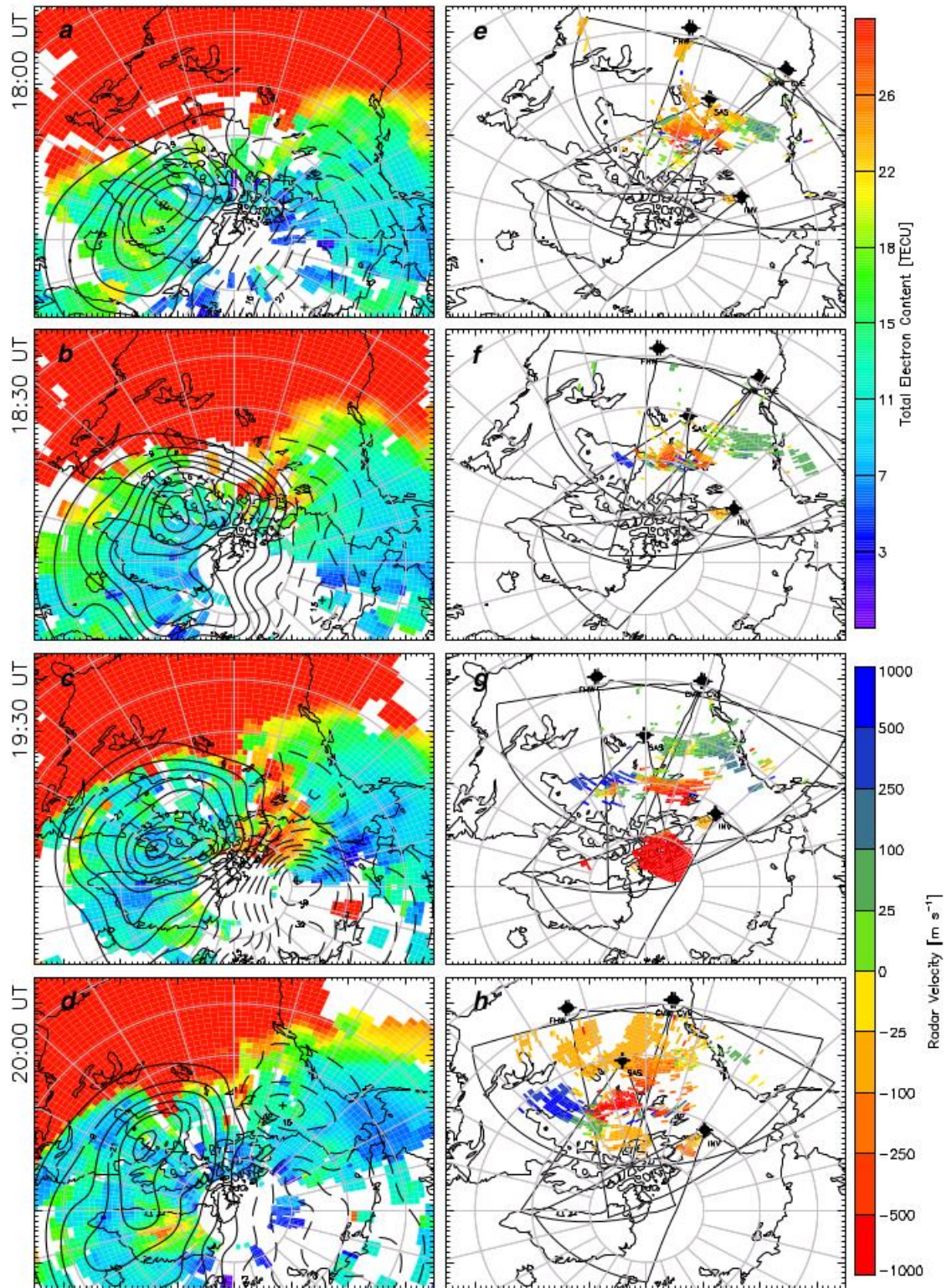


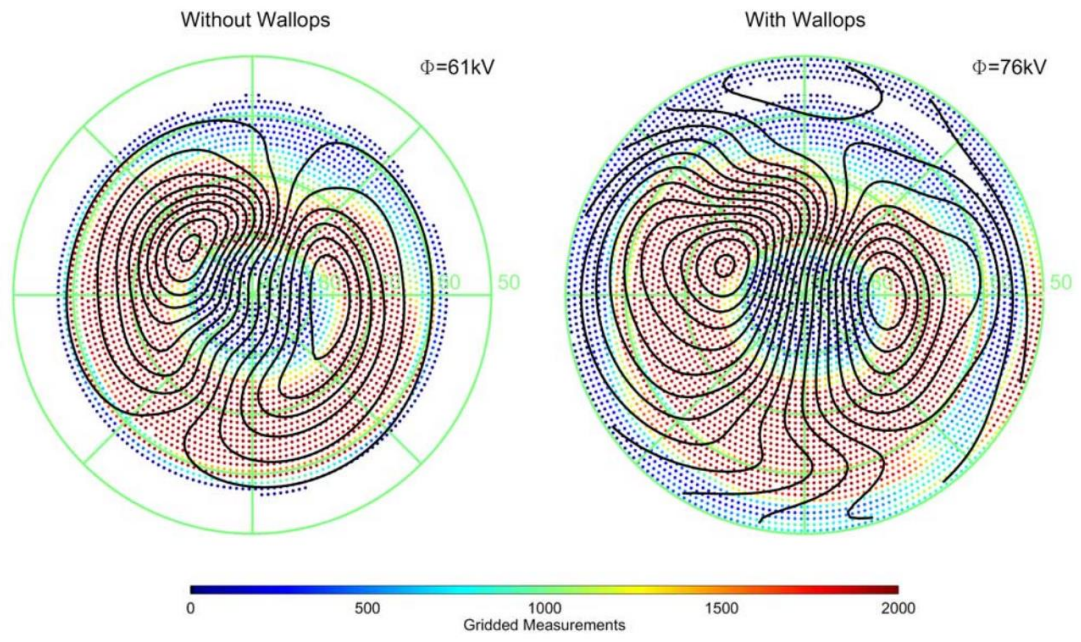


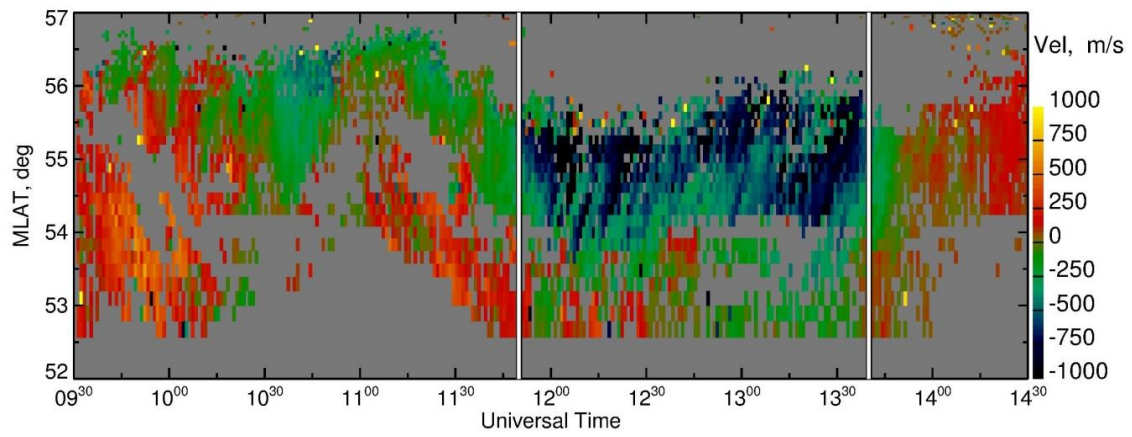


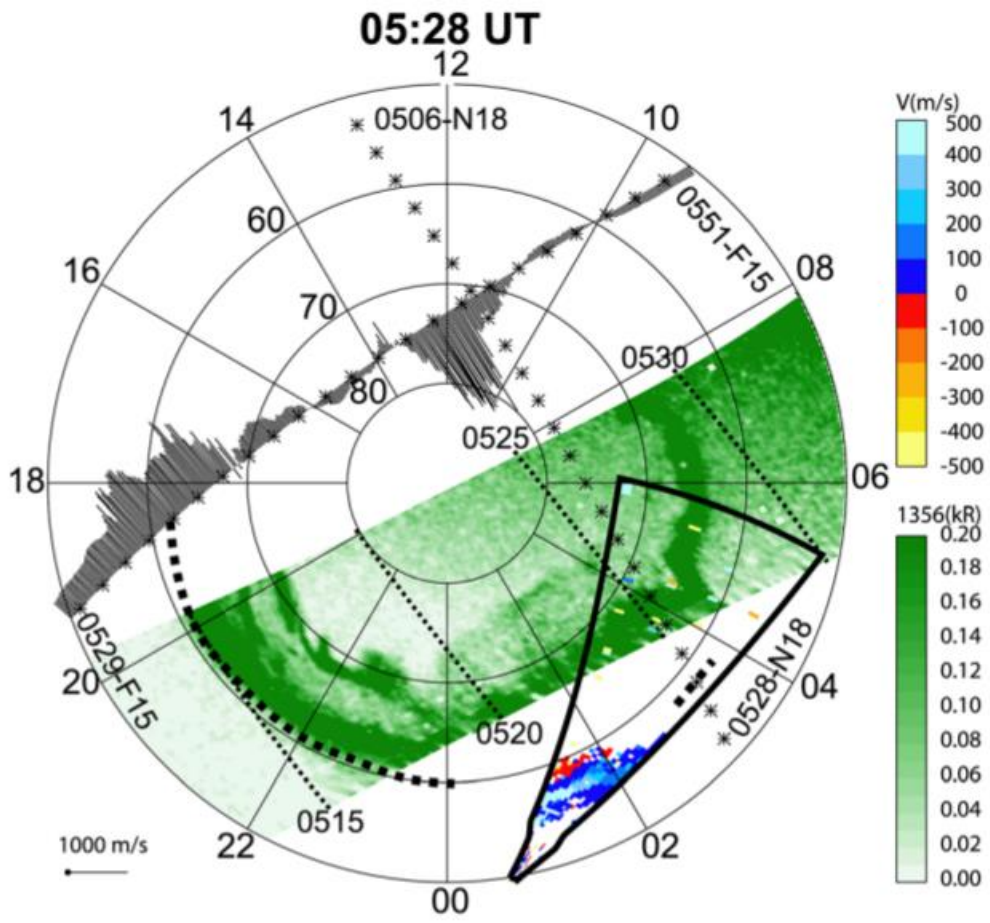


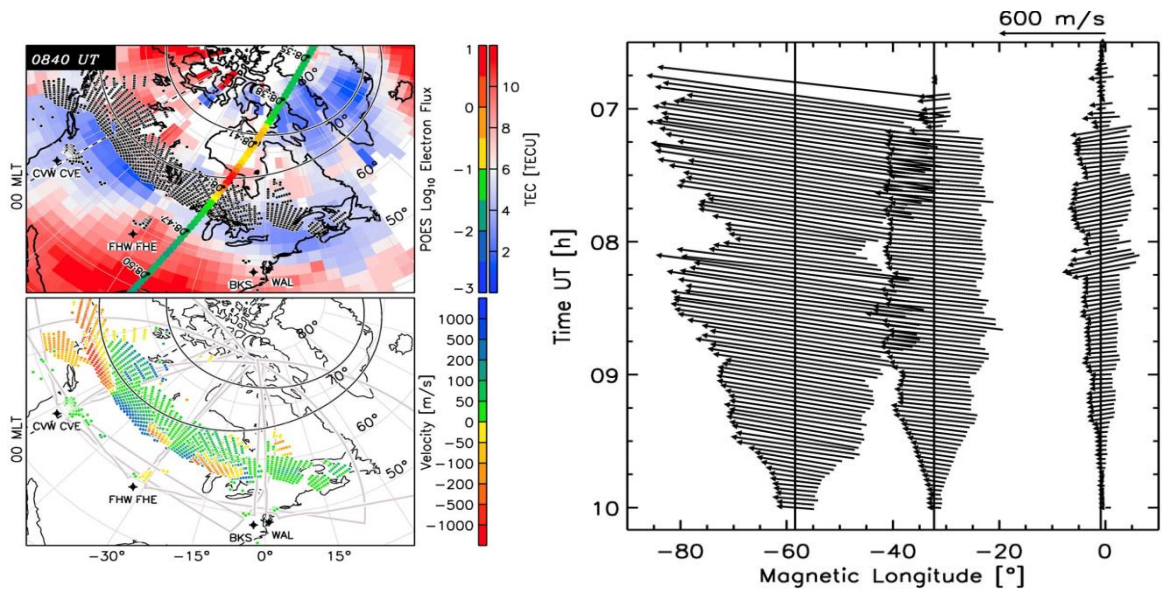


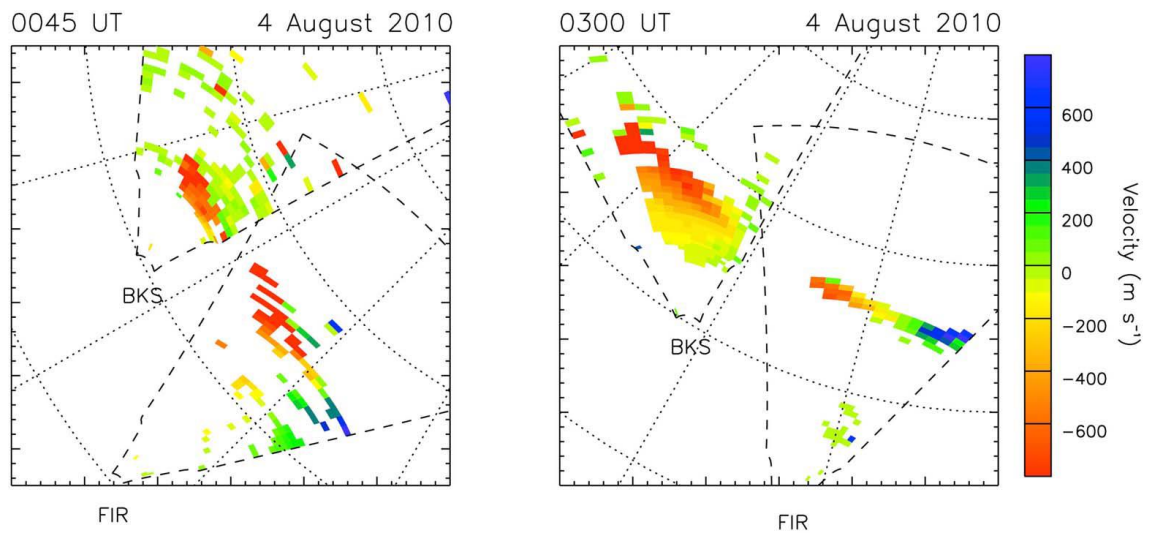


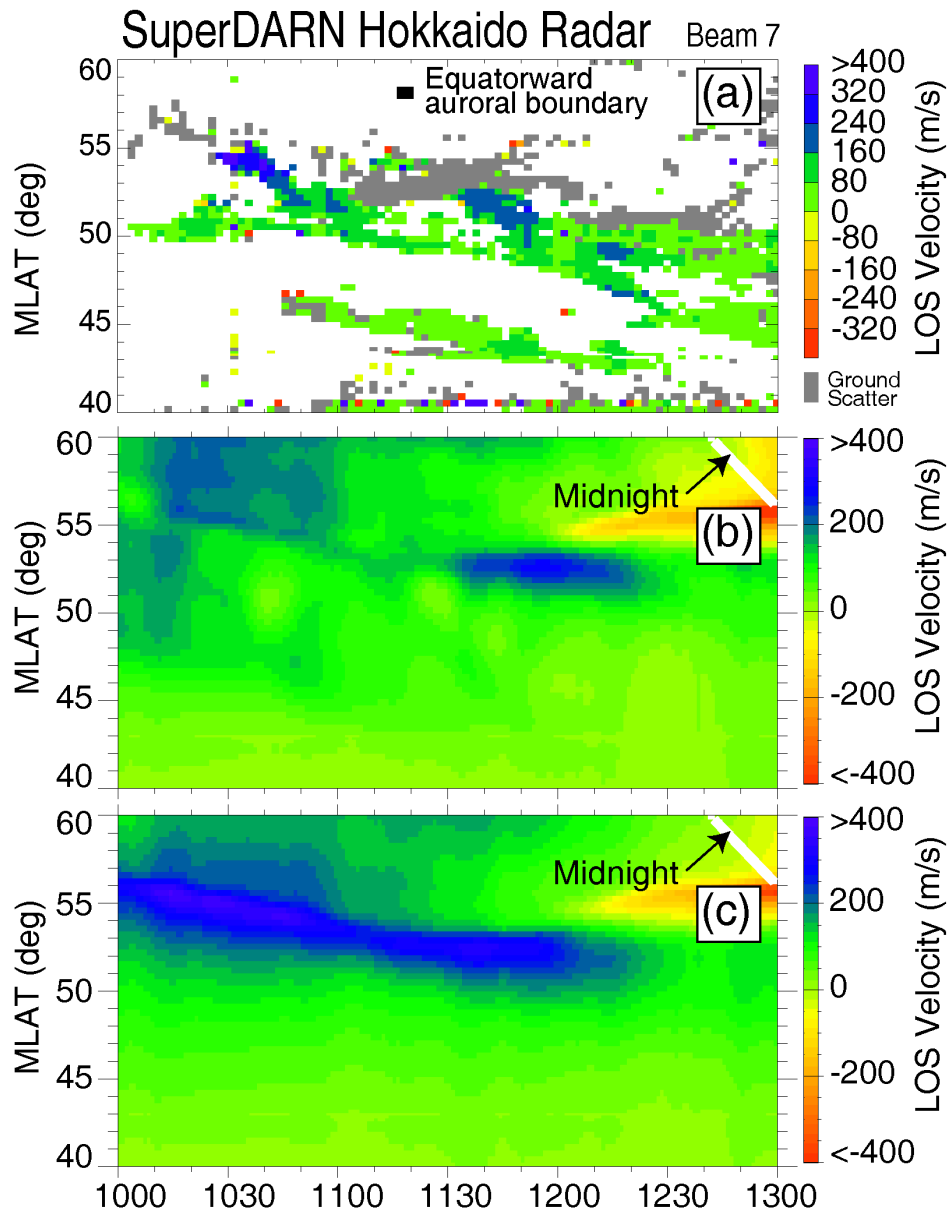


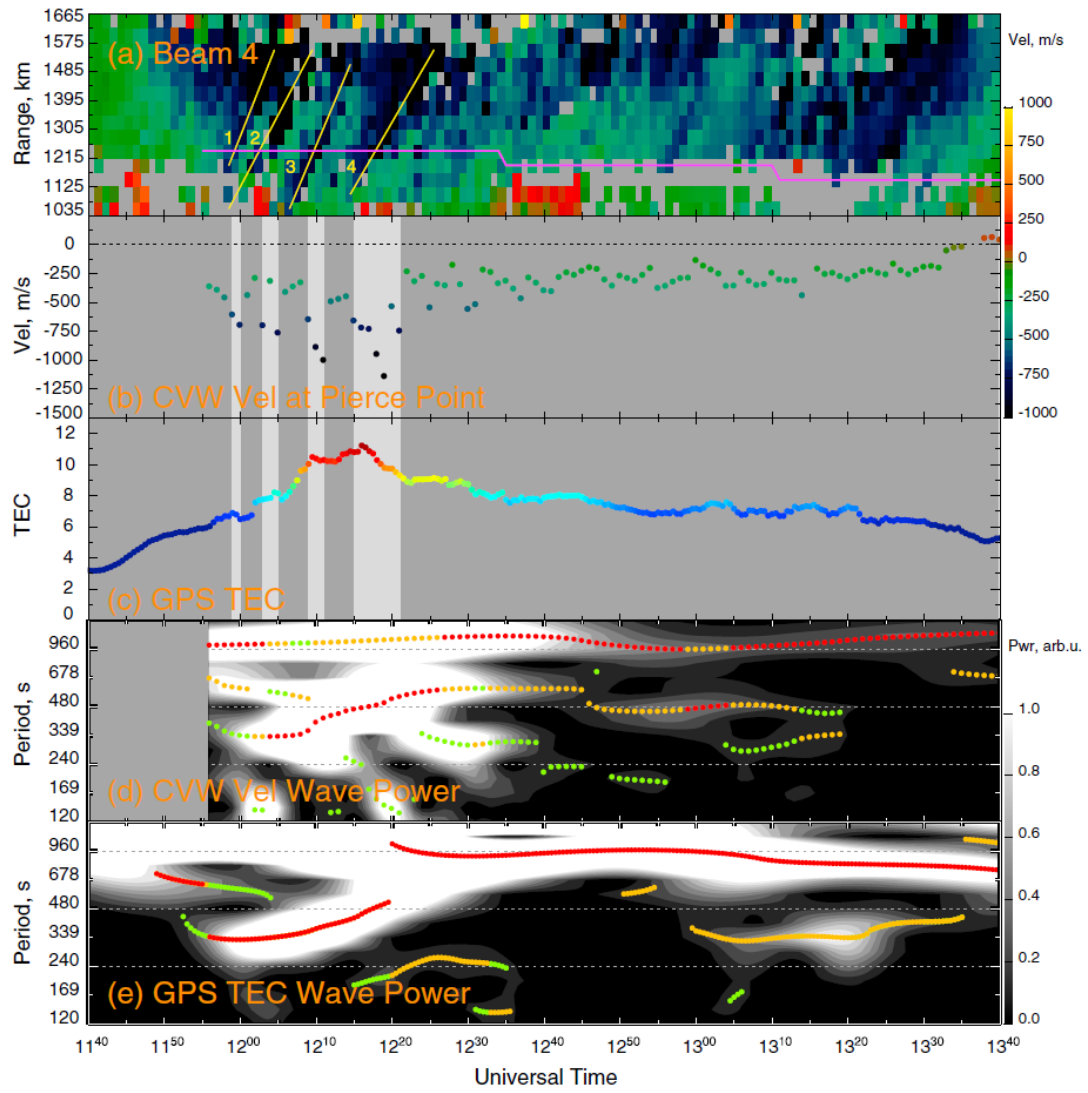


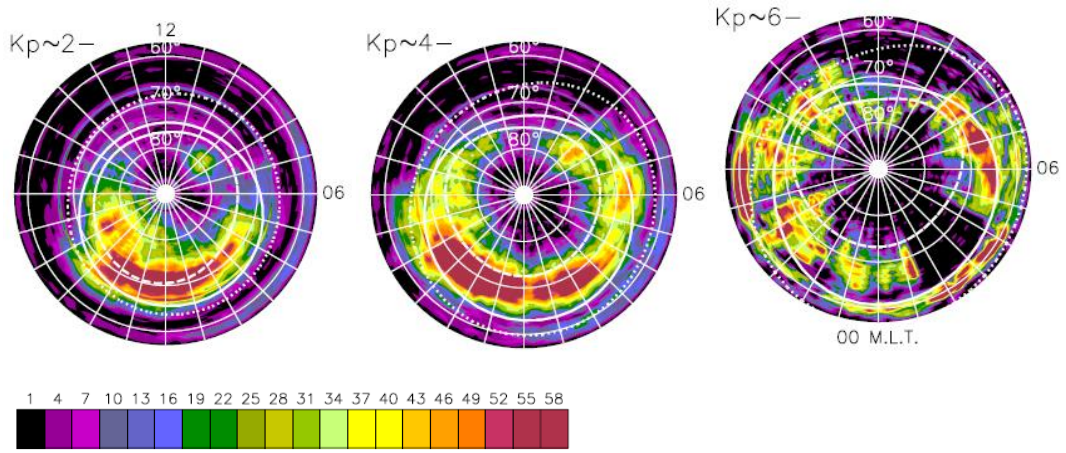


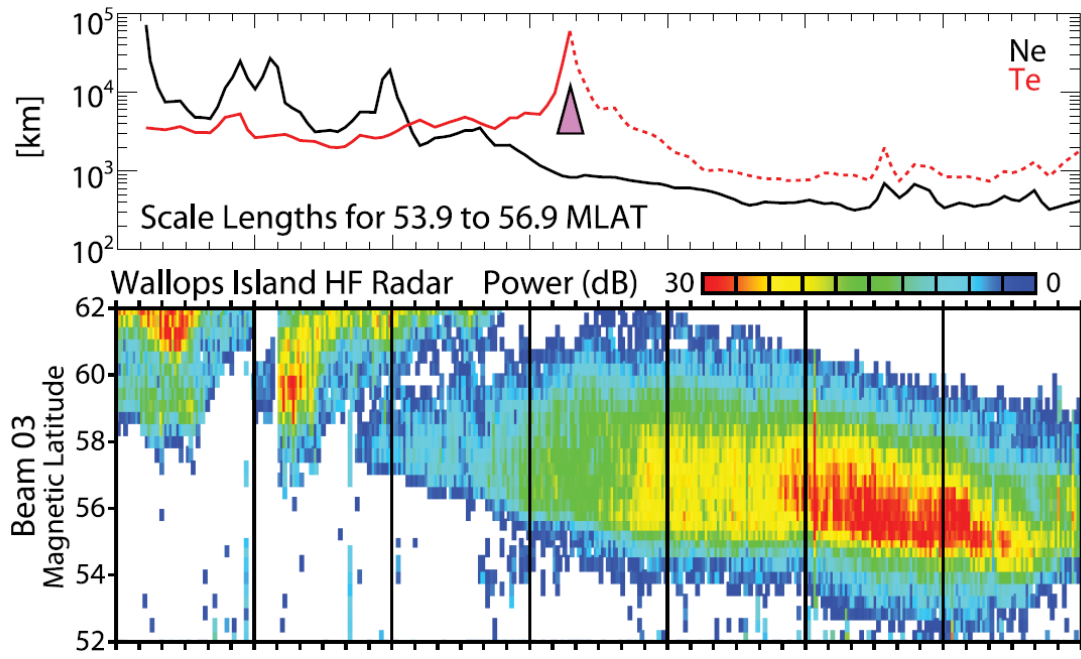


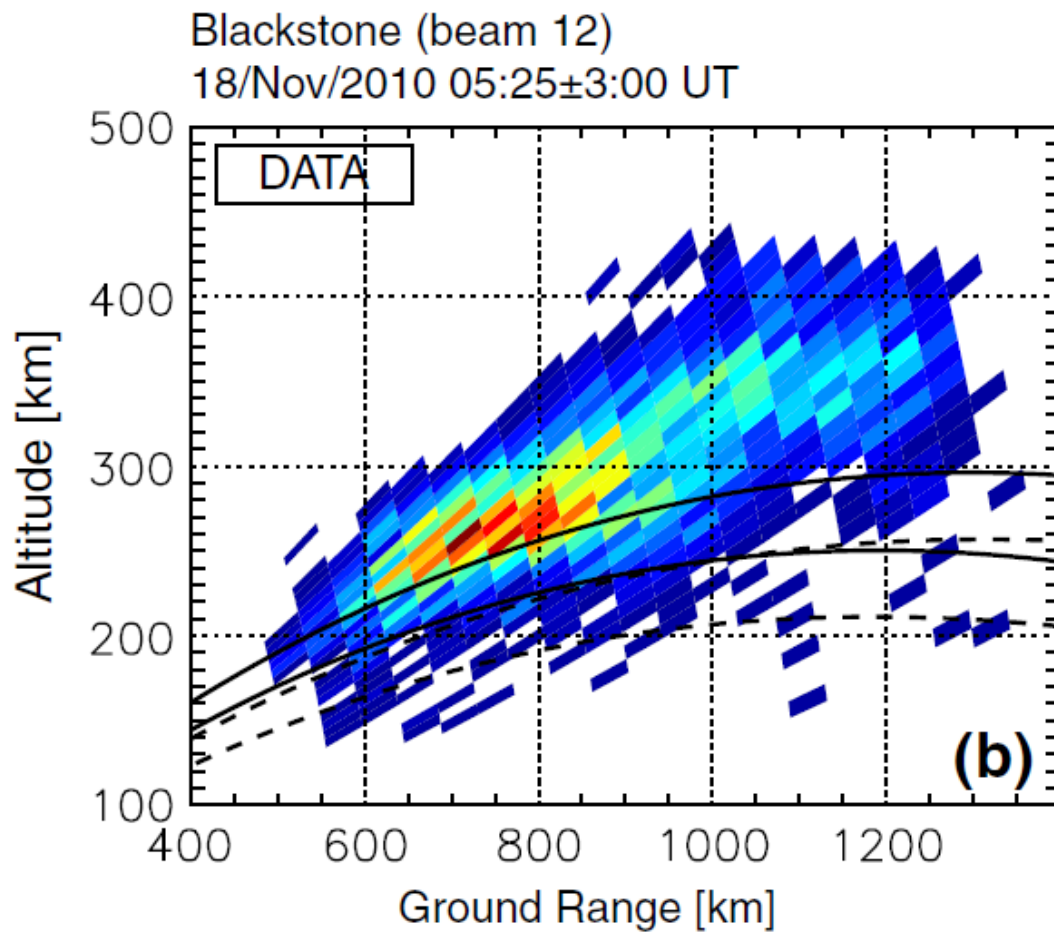


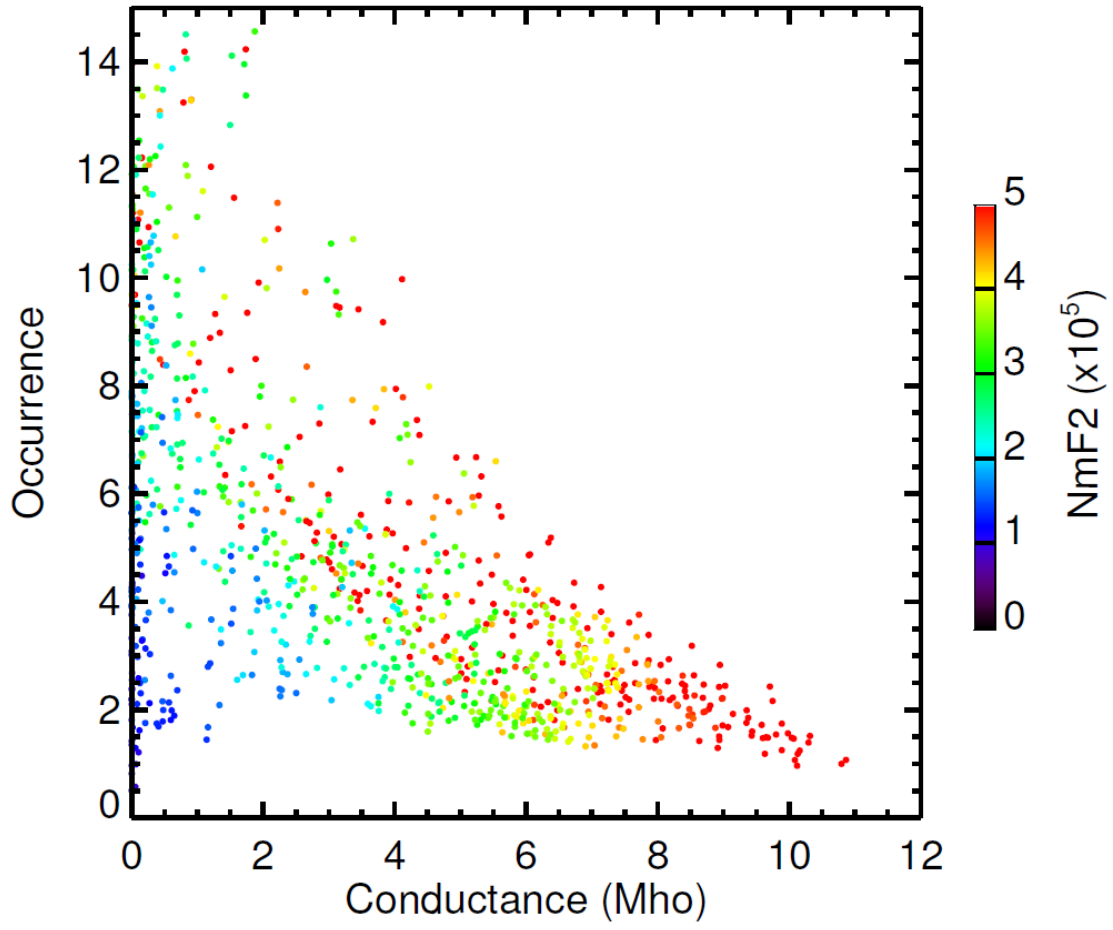


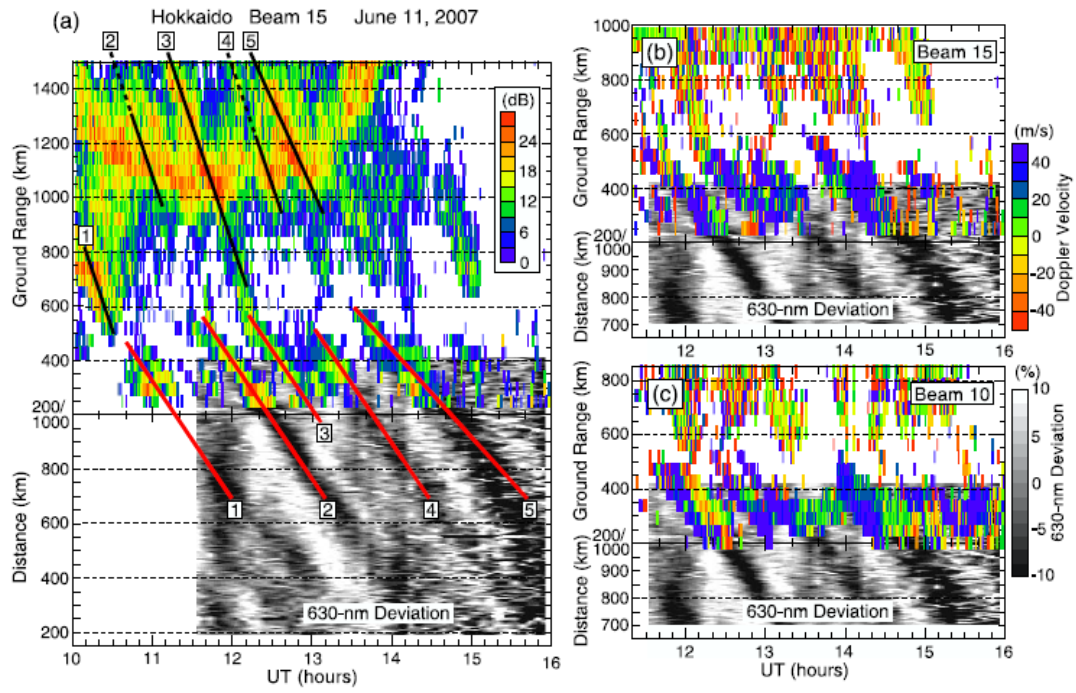


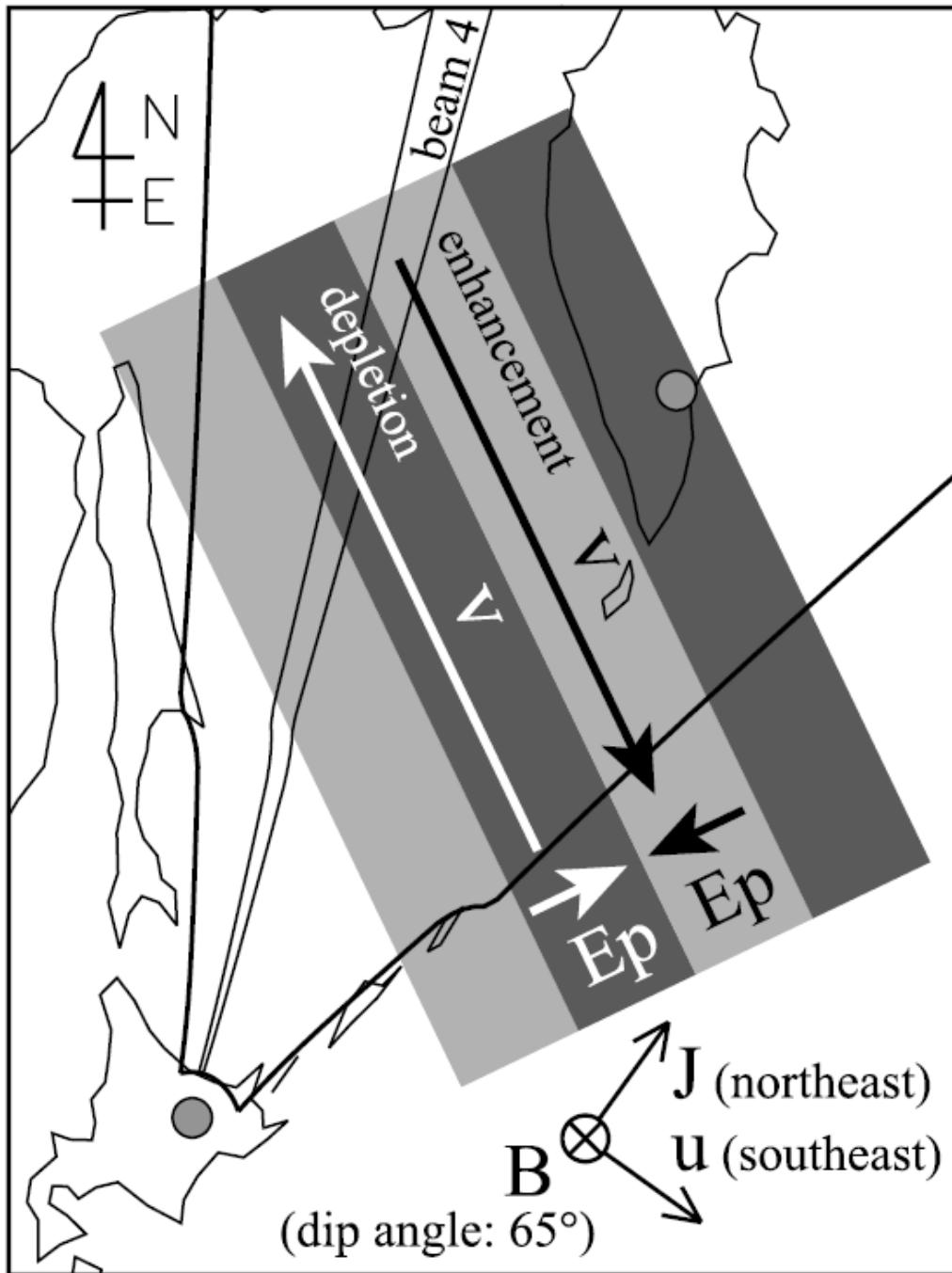


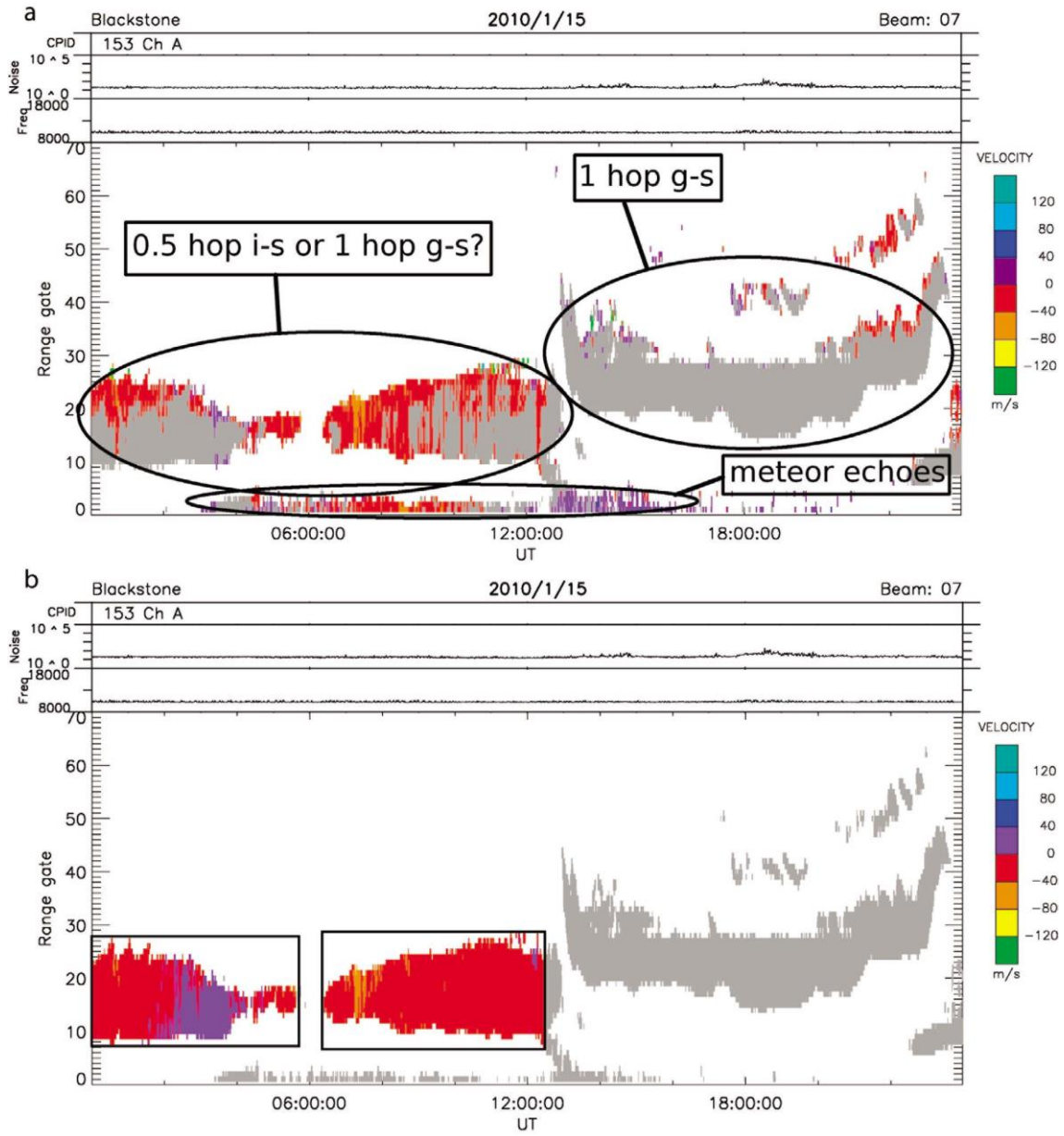


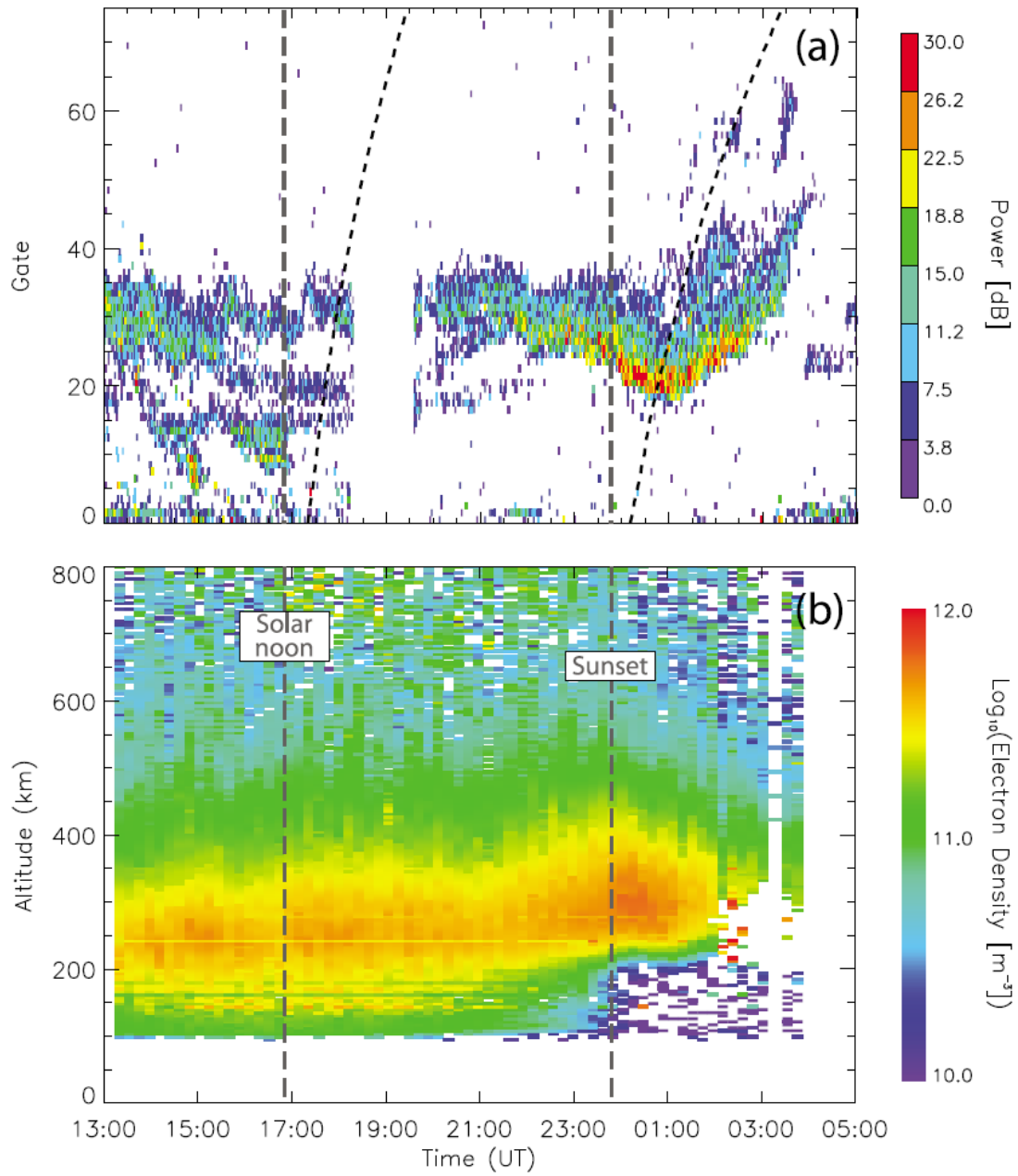


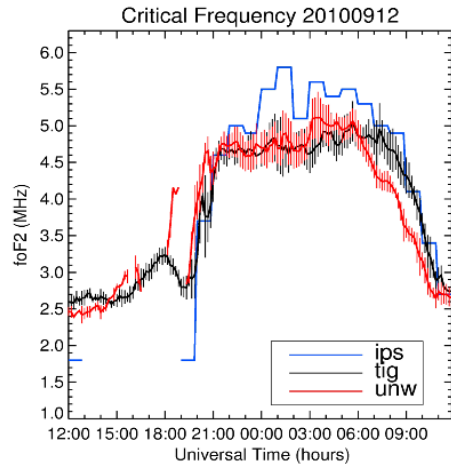


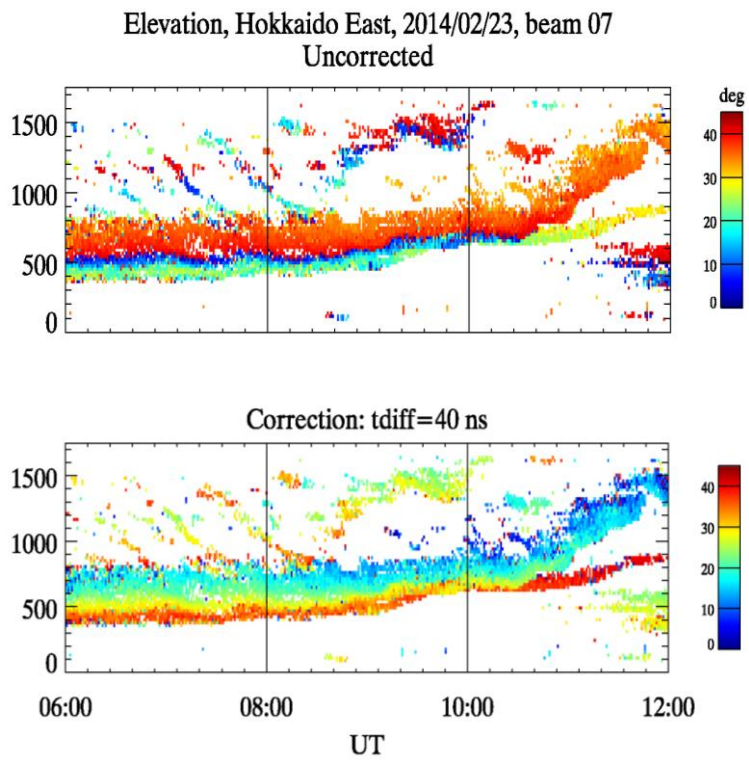




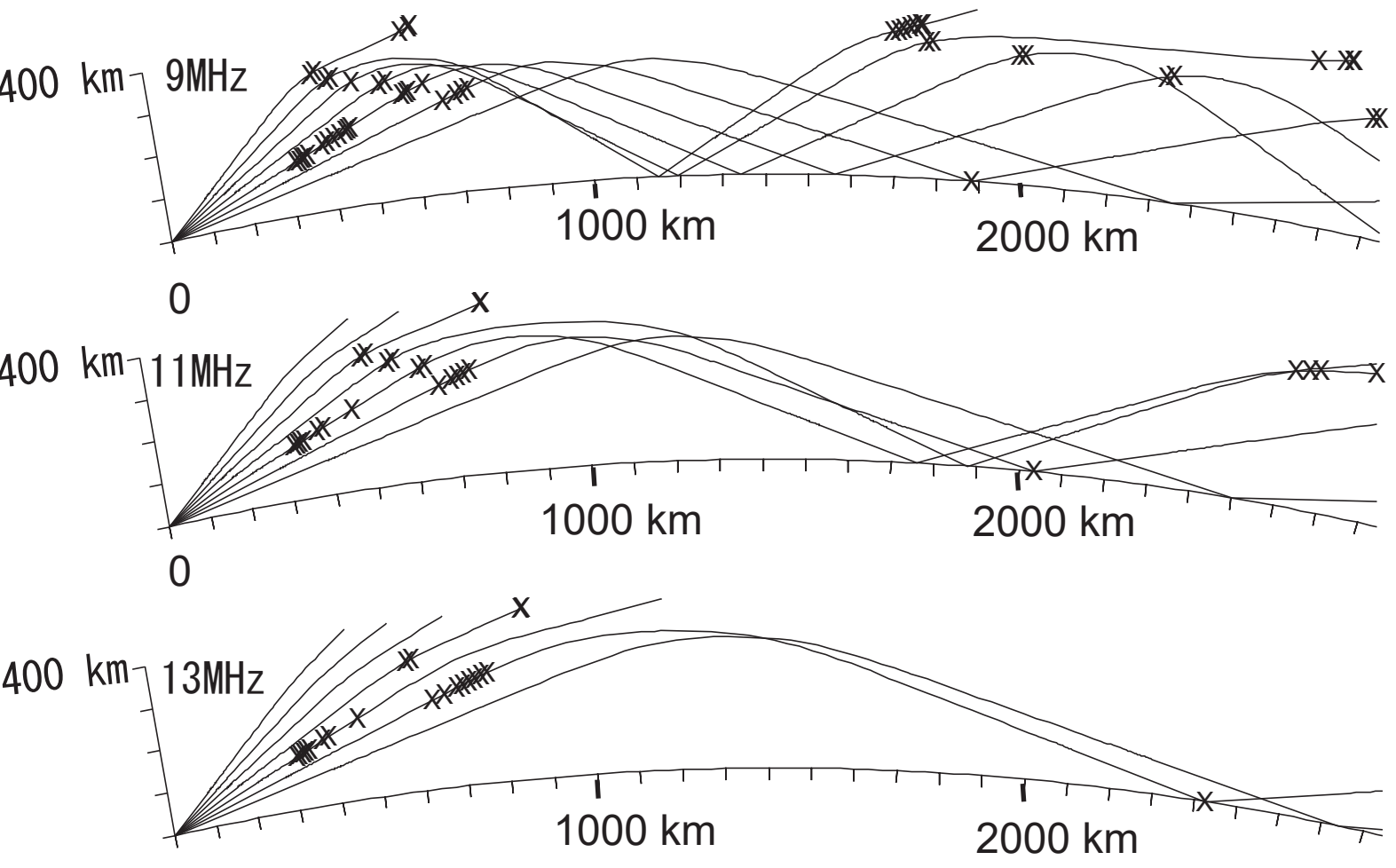


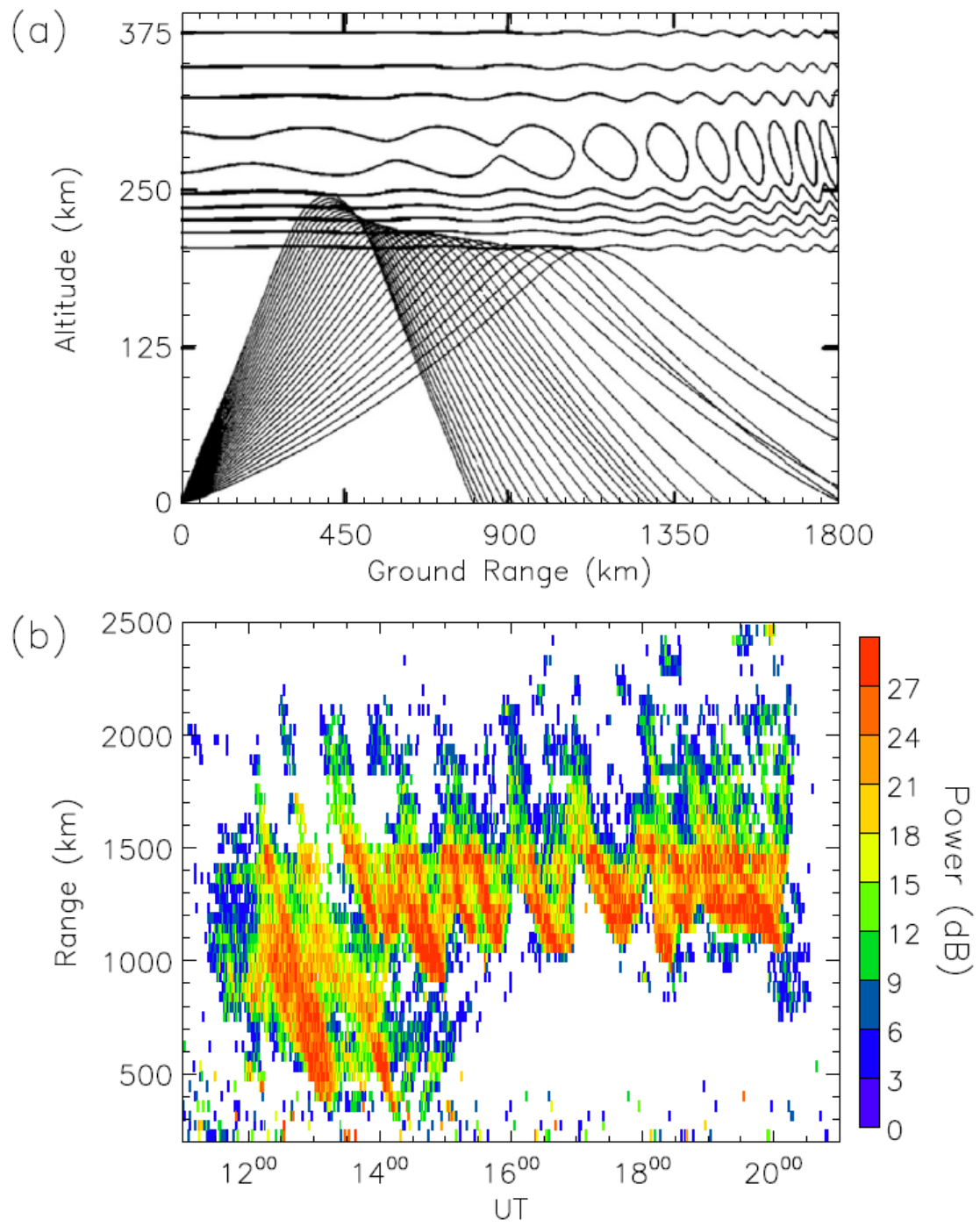


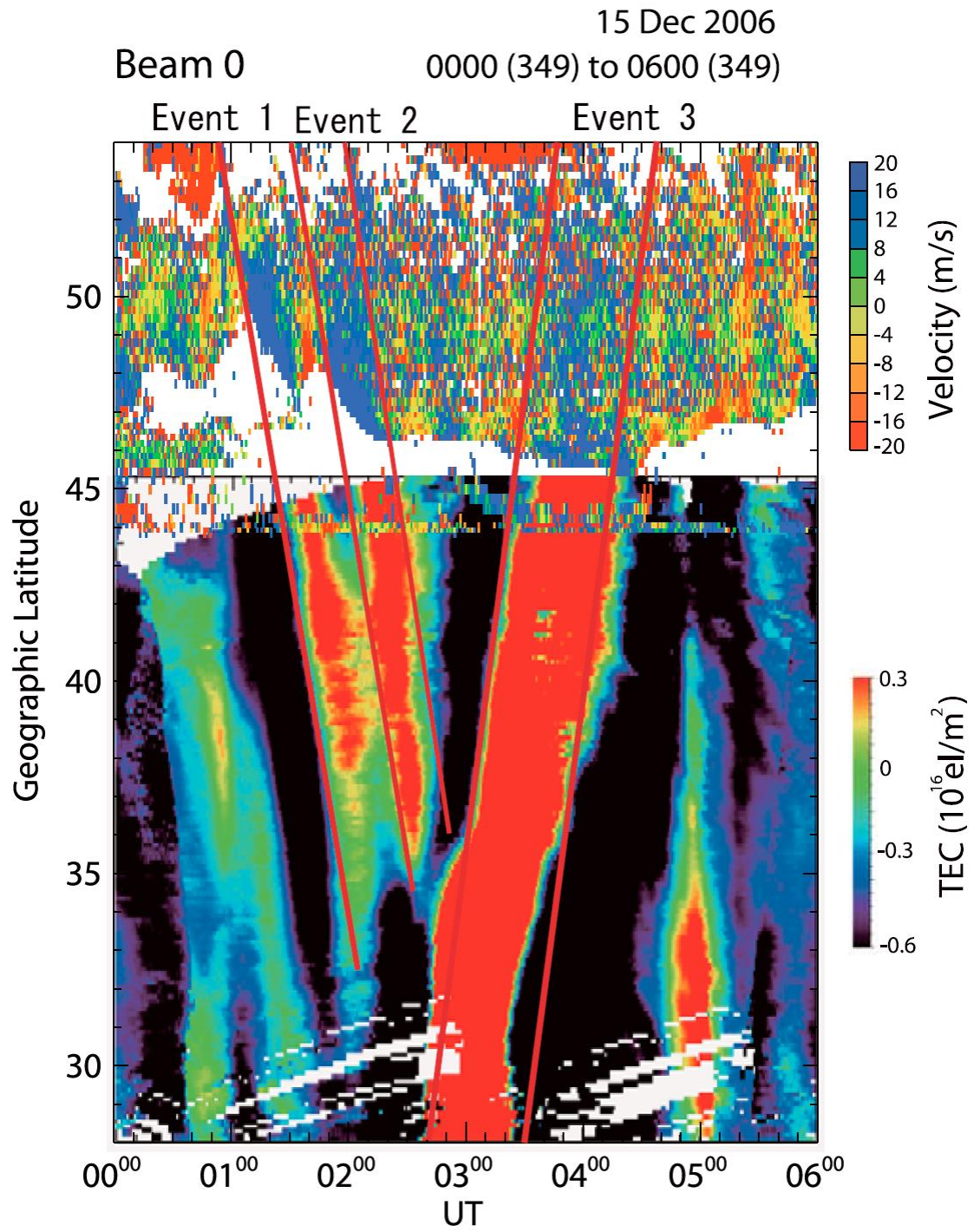


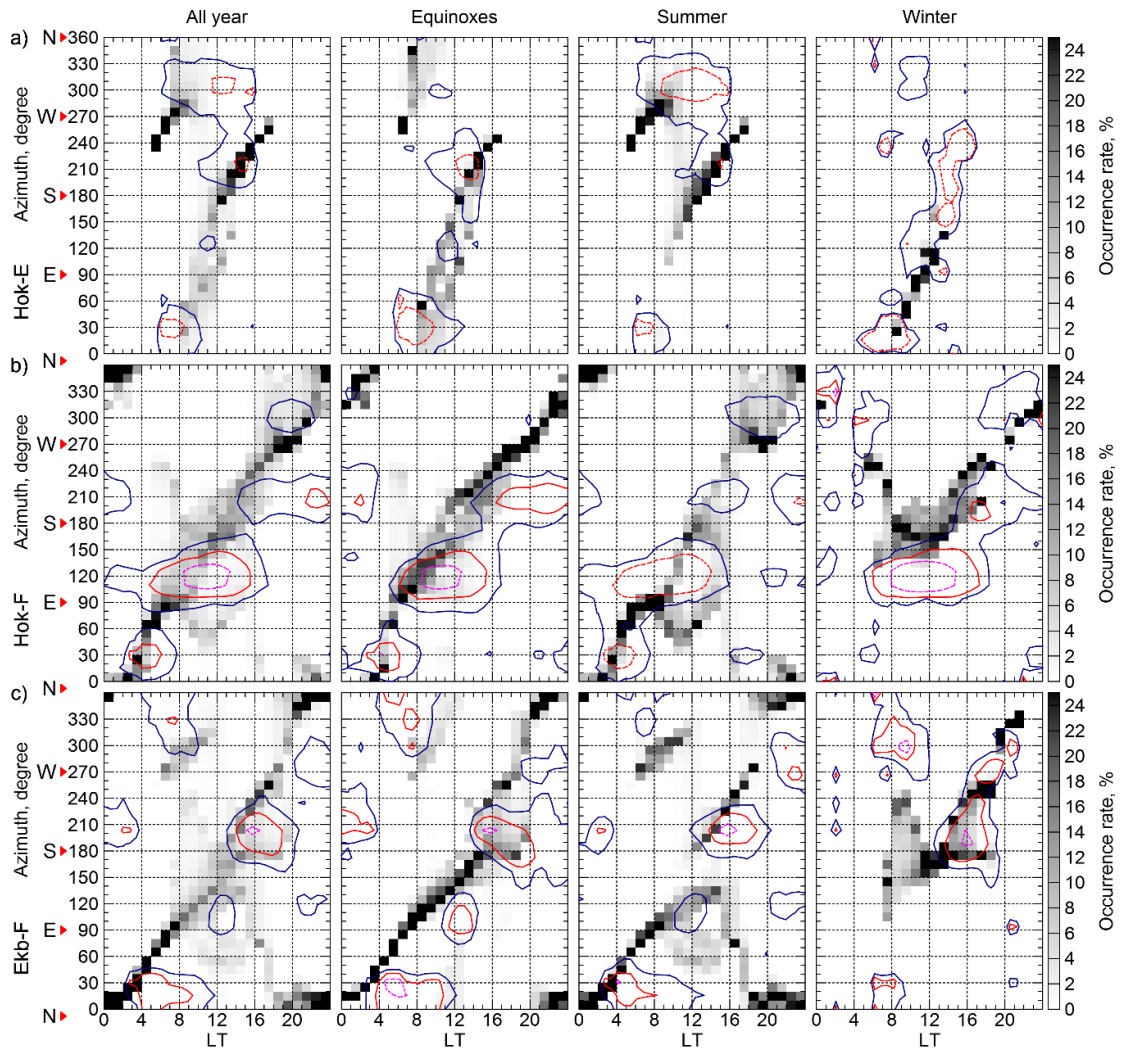


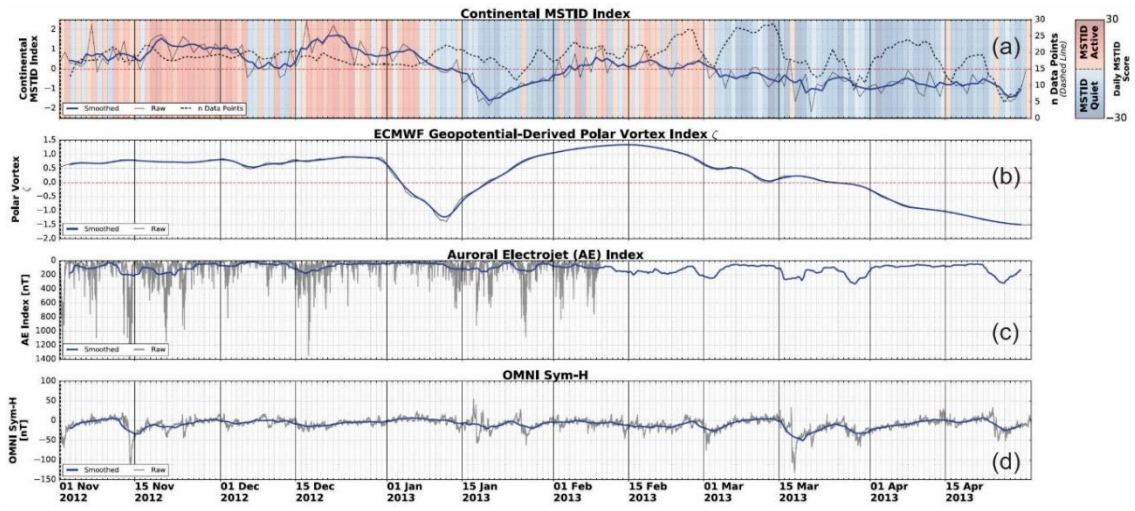
quiet nighttime (2003.3.26 0000 JST) $A_p=4$

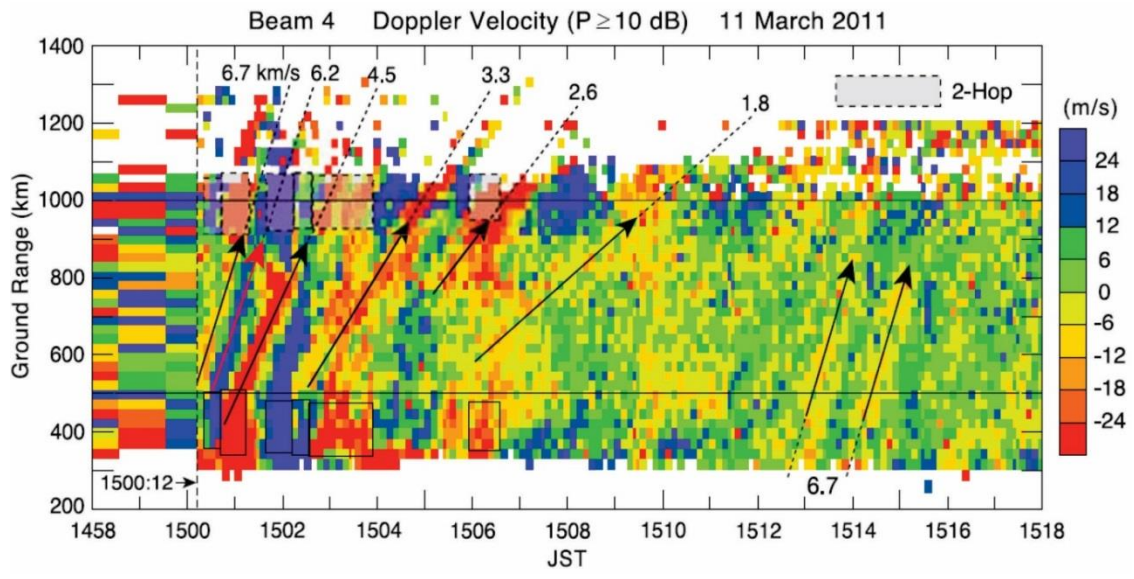


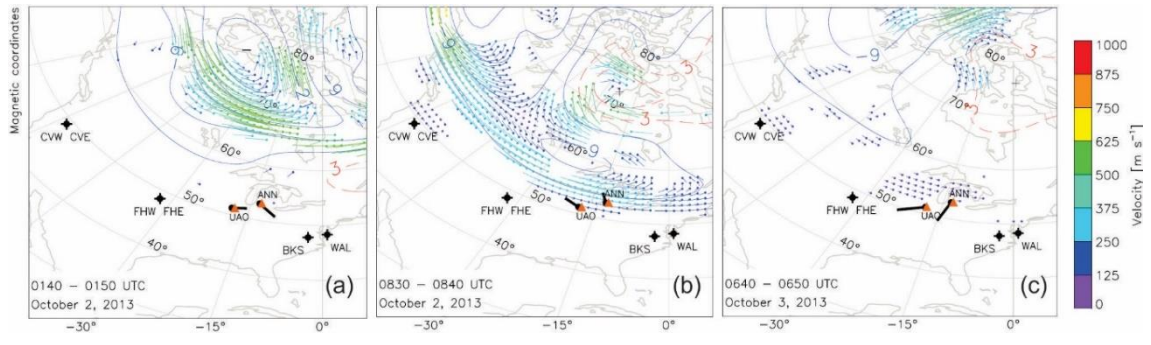


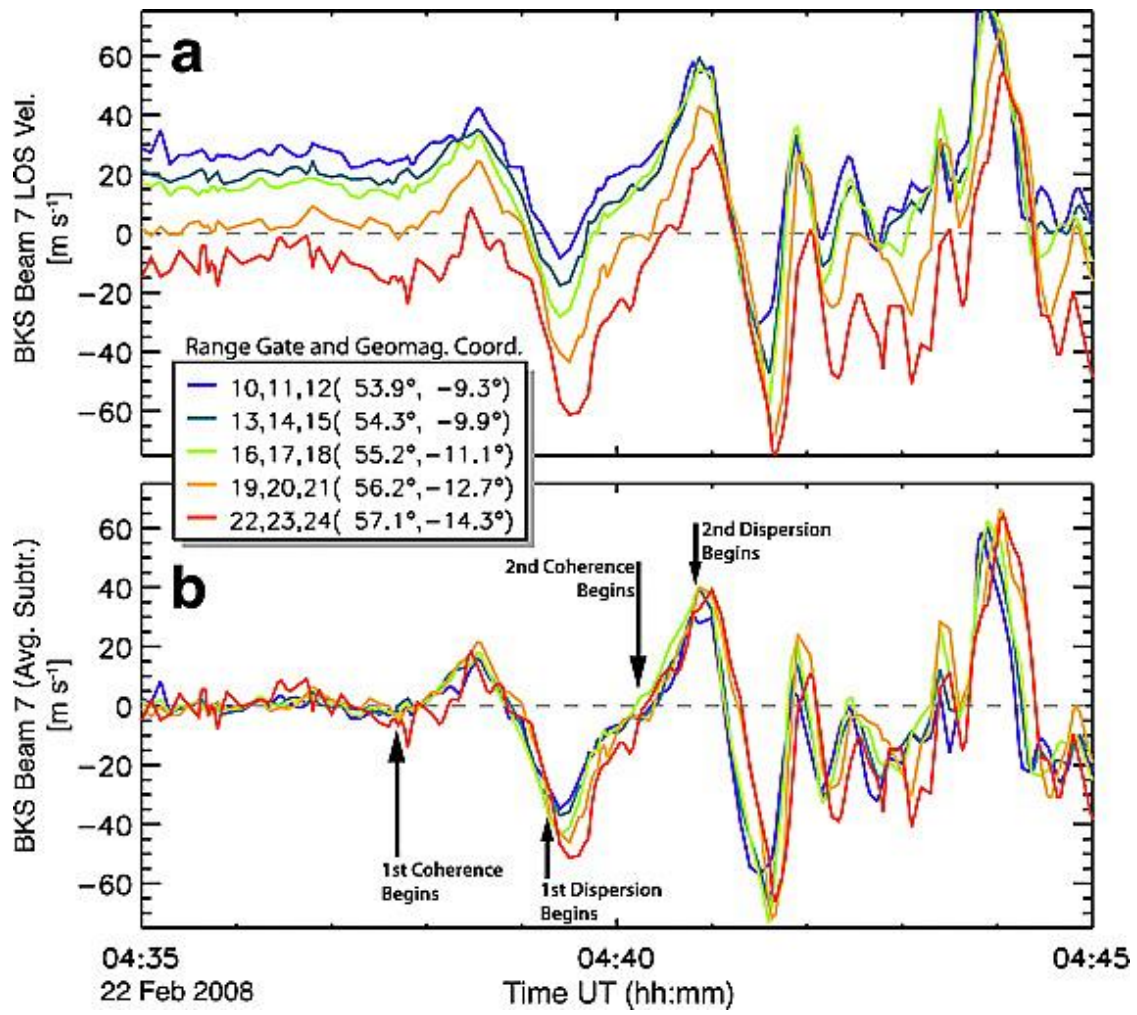


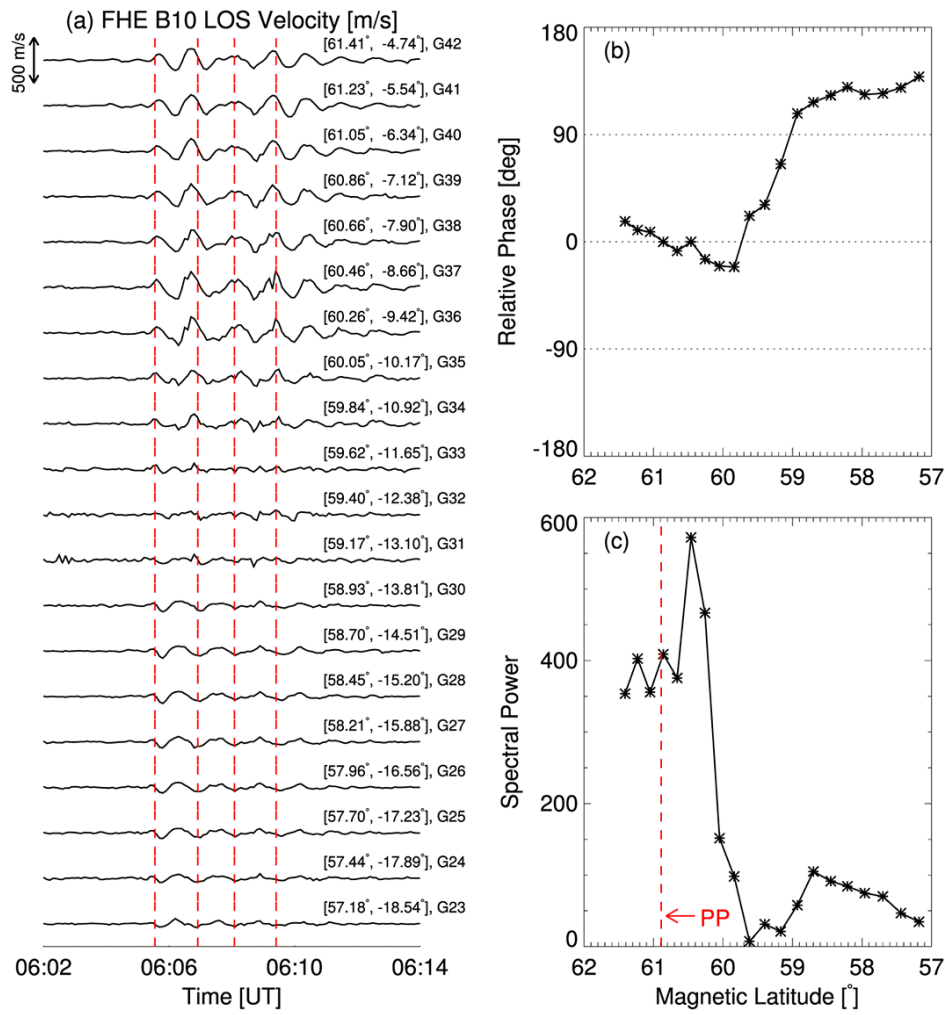


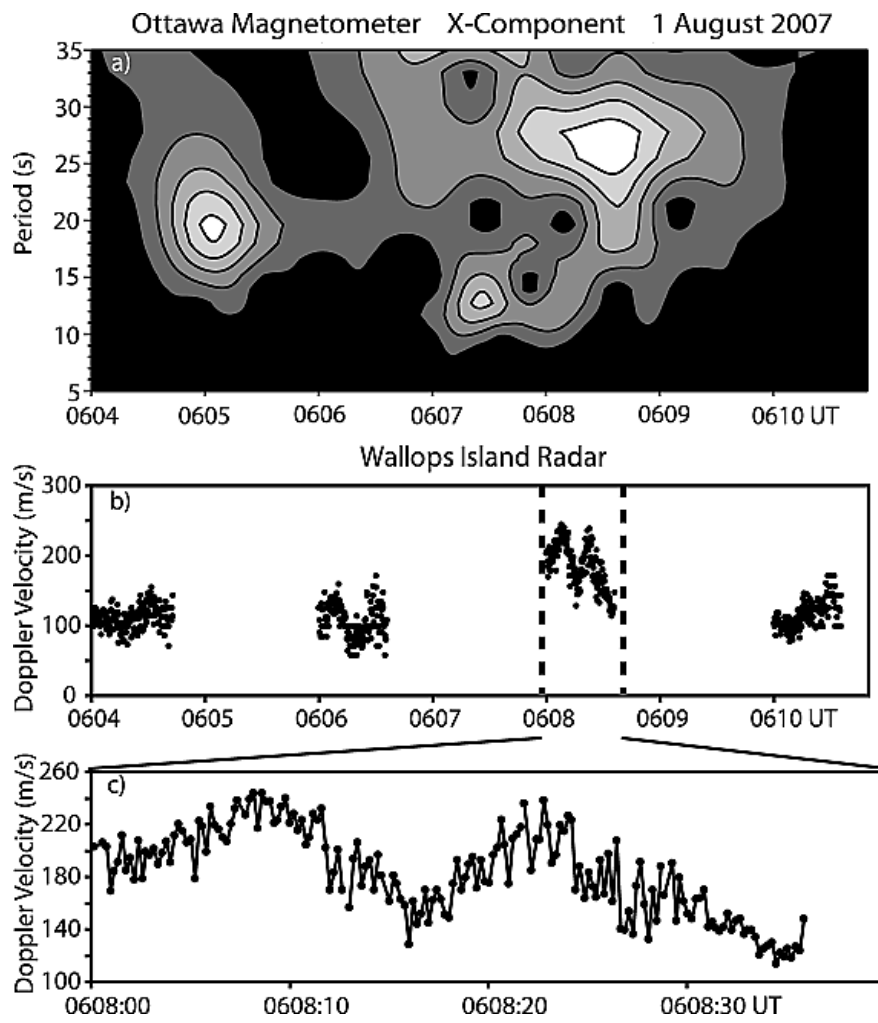


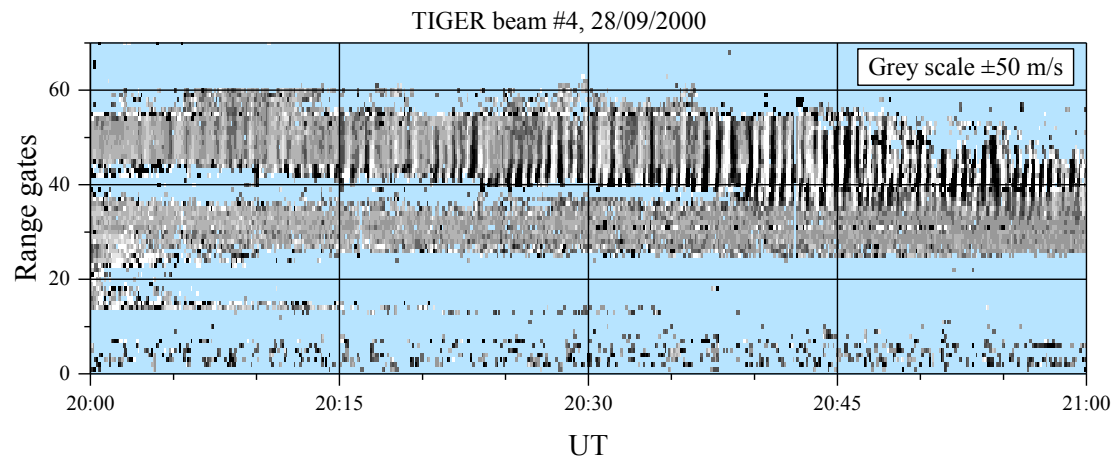


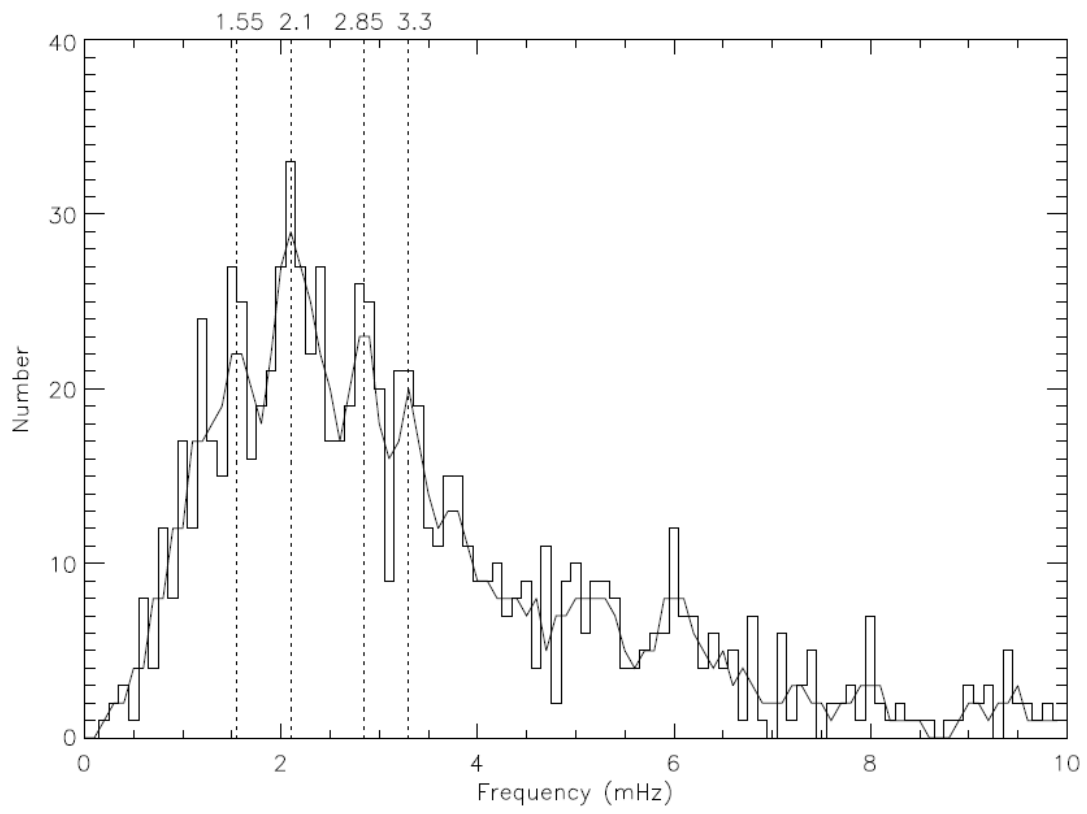














Click here to access/download

Supplementary Material

review_paper_additional_file_history_20181207_updated
.docx



[Click here to access/download](#)

Supplementary Material

[review_paper_whole_text_merged_20190129.docx](#)



